UNIVERSITY OF SALERNO

Department of Physics "E.R. Caianiello"

Doctor of Philosophy in Mathematics, Physics and Applications -
- Curriculum Physics - XXXV cycle - New Series

Doctoral thesis in

Praseodymium and manganese doped Ca_2RuO_4: crystals growth and physical properties

Marco Cannavacciuolo

PhD Coordinator:
Prof.ssa Patrizia Longobardi

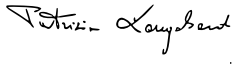

Tutors:
Prof. Alfonso Romano

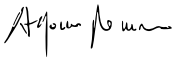

Dr. Rosalba Fittipaldi

Academic Year 2022/2023

To my Parents

Contents

Abstract

Layered ruthenates have received a great attention in condensed matter physics due to the richness of their physical properties and the related phase diagram, the latter being still far from a complete understanding. Ruthenate compounds show a strong interplay between electronic, structural, magnetic and orbital degrees of freedom. Two representative materials for this class of systems, Sr_2RuO_4 and Ca_2RuO_4, despite being isovalent, show, in fact, totally different physical properties. While Sr_2RuO_4 is a paramagnet with various magnetic fluctuations at high temperature showing an unconventional superconductivity below the temperature $\sim$ 1.5 K, Ca_2RuO_4 is a Mott insulator at room temperature and becomes an antiferromagnetic (AFM) insulator at $T_N \leq 113$ K.

What makes the above two ruthenates even more interesting is that, due to their multi-orbital nature, they are prototypical systems for studying the balance and interplay of multiple competing effects controlled by distinct physical parameters such as bandwidth, inter- and intra-orbital correlation, crystal field splitting, and spin-orbit coupling. As evidence for this, unusual structural, electronic, and magnetic phases have been found in $Sr_{2-x}Ca_xRuO_4$ systems, including crossovers of local and itinerant magnetism.

Interestingly, in recent years it has become evident that in Ca_2RuO_4 the delicate balance between competing microscopic interactions can be overturned by a slight external influence. Several experimental and theoretical studies have shown that the insulator-to-metal transition (IMT) in Ca_2RuO_4 is sensitive to external perturbations and can be tuned by temperature, electrical current, pressure, strain and chemical substitution. In this context, it is worth mentioning that the IMT in correlated electron materials is not only an important phenomenon in itself but its resistivity switching behavior can be useful for device applications, especially when the IMT occurs near room temperature as in Ca_2RuO_4. Examples along this line are sensors and logic elements for neuromorphic computation.

The present work was motivated by the expectation to clarify some open issues related to the IMT induced by different stimuli as well as the different magnetic ordering that emerges in Ca_2RuO_4 with doping. Two different routes have been explored to tune the IMT in the single layered calcium ruthenates system, one based on chemical substitution and the other one where the transition is induced by current. Regarding the

chemical substitution approach, either rare earth or transition metal site doping has been used. For this study, we grew pure Ca_2RuO_4 crystals as well as $Ca_{2-x}Pr_xRuO_4$ and $Ca_2Ru_{1-x}Mn_xO_4$ doped crystals.

Using angle-resolved photoemission nano-spectroscopy, we explored the evolution of the electronic structure in Ca_2RuO_4 as the crystal is driven across the IMT by the electrical current. Using a very small light spot, of the order of a few μm, we have shown that the current-driven IMT in Ca_2RuO_4 leads to the expected increase of the in-gap spectral weight, but at the same time the Mott state appears to be largely retained. An emergent semi-metallic state with simultaneous Mott character can be explained by the current-induced structural inhomogeneity of the sample, because band alignment between structurally different domains effectively reduces the overall gap. Our work thus unveils a novel type of non-equilibrium (semi-)metallic state that forms at the interface of Mott domains. Unlike what one would expect on the basis of well-known mechanisms, this situation arises from the structural inhomogeneity of a system, and it is entirely different from the mere coexistence of insulating and metallic domains that one would expect for a first order phase transition.

On a different track, this thesis also includes IMT tuning studies carried out by praseodymium doping and through the development of Pr-doped eutectic-like crystals with Ru inclusions. These systems offered an additional route to tune the IMT in Ca_2RuO_4. Compositional and structural studies of crystals synthesized by varying the excess of Ru in the starting melted material showed the formation of pure Pr-doped crystals using an excess of Ru of about 23%, while the synthesis of lamellar Ru inclusions was observed for a higher content of Ru excess. X-ray and electron diffraction studies revealed a decrease in the c-axis parameter of the $Ca_{2-x}Pr_xRuO_4$ phase in crystals with increasing Ru inclusions. In addition, structural studies have also allowed to infer the presence of a preferential orientation of the Ru lamellae inside the $Ca_{2-x}Pr_xRuO_4$ crystal. Regarding the electronic properties, transport measurements showed a decrease in the IMT temperature by increasing the amount of the Ru lamellae, while V-I characteristics at different temperatures showed similar behavior to that observed in Ca_2RuO_4, suggesting the emergence of a metastable current-induced metallic phase also in Pr-doped crystals with Ru inclusions. Our results show that the synthesis of crystals with regular arrangement of oriented Ru lamellae inside a Ca_2RuO_4 crystal may be a new way to tune the IMT and to explore and disentangle the mechanisms underlying the correlation between structural changes and IMT in this intriguing Mott insulator system.

Additionally, since slightly substituting Ru with a 3d transition metal ion effectively shifts IMT inducing exotic magnetic behavior below T_N, we explored by resonant X-Ray spectroscopy (REXS) the evolution of the structural, magnetic, and orbital degrees of freedom of Mn-doped Ca_2RuO_4. In particular, we revealed the mechanisms driving the antiferromagnetic transition as a function of the doping content. Thus, through the substitutional doping of Mn in Ca_2RuO_4 we have found a way to control

and measure the subtle change in magnetic ordering induced without changing the symmetry of the crystal structure. REXS measurements allowed us to unambiguously determine the magnetic ordering and separate the change in orbital population from the structural changes observed through traditional X-ray diffraction measurements. The resulting mechanism helps to understand the universality of the change from the A-centered to the B-centered magnetic phase in the material under a wide range of different Mn doping. Since the transition can be induced by atomic substitution, our results open new paths for the design of magnetic phases by dopant engineering or, prospectively, by exploiting surface deposition in ultra-thin films to induce surface magnetic reconstructions.

The results presented in this doctoral thesis were obtained within a collaboration between the Department of Physics "E. R. Caianiello" of the University of Salerno, the Musa Laboratory of the National Research Council - SuPerconducting and other INnovative materials and devices-Institute (CNR-SPIN), the Department of Physics and Astronomy of the Aarhus University, Denmark, and the Diamond Light source, United Kingdom.

OUTLINE OF THE THESIS

- **Chapter 1** (*Introduction to Mott Insulators*) introduces general concepts about the physics of the Mott insulators and, in particular, of the compound Ca_2RuO_4, also providing a brief experimental and theoretical overview of the main topics underlying this work.

- **Chapter 2** (*Experimental methods*) is devoted to the description of the experimental methods used.

- **Chapter 3** (*Results*) reports on the parameters adopted for the growth of the different crystals and the results of the various experiments performed on Ca_2RuO_4, $Ca_{2-x}Pr_xRuO_4$ and $Ca_2Ru_{1-x}Mn_xO_4$ samples.

The research presented in this thesis, being an experimental work that deals with extremely complicated systems, fabrication techniques, and measurements, has been strongly affected by the COVID-19 pandemic since it has slowed down the experimental activities.

Chapter 1

Introduction

1.1 The relevance of the electronic correlations

The description of electrons in a solid is usually done within the framework of the traditional band theory. In this approach, electrons are considered as non-interacting particles that move in the presence of the periodic potential generated by the crystal lattice. The electron-electron interaction, when it is introduced into the theory, is routinely treated by techniques that still allow one to refer to representation in terms of "objects" often called quasi-particles, which are mutually independent or at most are weakly interacting. The use of this concept to describe the complicated interrelated dynamics of a many-particle system, as determined by the strong and long-ranged Coulomb interactions between the electrons, has turned out to be an extraordinarily useful device in contemporary physics. It is generally accepted that the greatest achievement of band theory is that it allowed to successfully classify a large number of crystalline solids as metals or insulators.

In many cases, however, this type of approach turns out to be wholly unsatisfactory because the physical properties of certain systems may depend crucially on the presence of strong electronic correlations. It is well known, for example, that in order to adequately explain the existence of magnetic ordering in solids one is forced to abandon the independent-electron approximation and to introduce *ad hoc* models that explicitly contain the effect of electron-electron interaction.

An even more spectacular failure is that, contrary to what is experimentally found, in particular in low-dimensional systems, it predicts that certain insulators should be metal. The reasons behind this drawback of the band theory, first clearly pointed out by Mott [1, 2], can be understood referring to a so-called “thought experiment” (Gedankenexperiment). Let us consider a one-dimensional chain of equally spaced hydrogen atoms, each of them having its single electron in the lowest $1s$ energy level. As it is well known, the tight-binding approach leads to a band structure that in the case

of electron hopping between nearest-neighbor atoms only, has the following analytical expression:

$$\varepsilon(k) = \alpha + 2\beta \cos(ka) \ . \tag{1.1}$$

Here k is the electron wavevector, α is the electron energy when the atom is isolated,

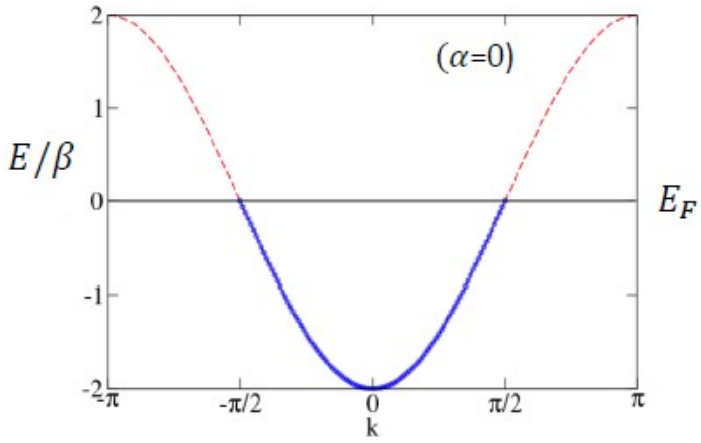

Figure 1.1: Tight-binding $1d$ energy spectrum given by Eq. (1.1). The blue part of the curve corresponds to the single-particle states occupied up to half filling.

given by

$$\alpha = \int dx \, \phi_i^*(x) \, H \, \phi_i(x) \tag{1.2}$$

and β is the so-called overlap integral:

$$\beta = \int dx \, \phi_i^*(x) \, H \, \phi_{i+1}(x) \ . \tag{1.3}$$

In the above expressions H is the Hamiltonian operator and $\phi_i(x)$ is the wavefunction of the electron belonging to the i-th atom. The behavior of the energy spectrum (1.1) is reported in Fig. 1.1.

What happens if we imagine to gradually increase the spacing between atoms, that is, if we consider increasing values of the lattice constant a? The bandwidth reduces as a consequence of the reduction of the overlap integral β, but even though the effective mass gradually gets lower, nonetheless the system remains metallic. Band theory thus predicts a metallic behavior even at very large interatomic spacing, this being of course totally unrealistic since in this case the system tends to become an array of independent neutral atoms. It is thus evident that at some critical spacing the systems should undergo a transition from metal to insulator, the so-called Mott transition.

In order to explain the mechanism underlying the Mott transition a key ingredient that must be introduced into the theoretical description is represented by the Coulomb interaction between electrons. This requires the formulation of a new scheme that

goes beyond the standard independent electron approximation on which band theory is based. Referring again to a chain of hydrogen atoms, described as a half-filled one-dimensional array of regularly spaced sites each hosting one electron, we have that for not too high values of the interatomic spacing, an electron with given spin can jump to an adjacent site, already occupied by another electron, provided the latter has opposite spin. However, the double site occupation that in this way is created, has in general a non-negligible cost in energy since the Coulomb repulsion between opposite-spin electrons occupying the same orbital is the higher the narrower is the extension of that same orbital. As a result, double occupations are energetically unfavourable, and thus tend to hinder electron mobility.

On the other hand, if two neighboring atoms are close enough to have a significant overlap between the corresponding electronic wavefunctions, for an electron it can nonetheless be energetically favourable to jump from an atom to the adjacent one, rather than remain localized on the atom it initially belongs (see Fig. 1.2). This tendency of the electrons to move along the chain is measured by the so-called "hopping amplitude", which is in turn proportional to the overlap integral β defined in Eq. (1.3). Conversely, as the lattice spacing is increased, it becomes more difficult for an electron to move to a neighboring atom, what implies a reduction of the electron kinetic energy and thus of the bandwidth.

At a critical value of the lattice spacing, the gain in kinetic energy becomes too low to compensate the cost in energy associated with double occupations, and thus mobility gets completely blocked: this corresponds to the onset of the metal-insulator transition, which thus emerges from the competition between kinetic and potential effects.

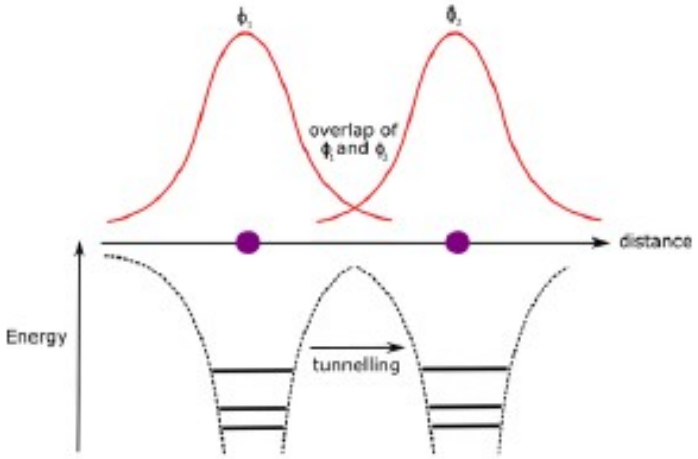

Figure 1.2: Overlap between the wavefunctions at the adjacent sites originating hopping processes between them.

Let us now provide a simple quantitative argument justifying the above scenario, presented in a form similar to the one given in Ref. [3]. The total energy of an assembly of N isolated hydrogen atoms is equal to $N\alpha$, where α is quantity defined in

Eq. (1.2). When the atoms are sufficiently close to allow hopping processes, the total energy, of purely kinetic origin, gets lowered and can be expressed in the form

$$E_K = N(\alpha - C\beta) \tag{1.4}$$

where C is an adimensional constant of order of unity and β is the overlap integral (1.3).
On the other hand, electron mobility tends to make some sites doubly occupied. The probability that a site is occupied by an electron with spin σ is 1/2, and the same of course holds for an electron with opposite spin. The probability that a site is doubly occupied is thus 1/4, so that the cost in energy due to presence of double occupations is

$$E_U = \frac{1}{4}NU \ , \tag{1.5}$$

U denoting the intraorbital Coulomb repulsion.
The total energy when mobility is allowed is thus

$$E = E_K + E_U = N\left(\alpha - C\beta + \frac{1}{4}U\right) \ . \tag{1.6}$$

When this energy becomes larger than the one of N isolated atoms, i.e. when

$$N\left(\alpha - C\beta + \frac{1}{4}U\right) > N\alpha \tag{1.7}$$

it becomes energetically more favourable for the electrons to lose completely their mobility, in such a way to avoid all possible double occupations. From Eq. 1.6 we see that the transition occurs at a critical value U_c of U given by

$$U_c = 4C\beta \tag{1.8}$$

such that for $U > U_c$ the system behaves as an insulator.
The simplest model taking into account the combined effect of the kinetic energy and the local Coulomb repulsion is the widely studied Hubbard model. To illustrate its basic features, let us start again from the case of an isolated hydrogen atom in its ground state, that is, there is only one electron occupying the $1s$ level with an energy $E_0 = -13.6\,\text{eV}$. Suppose now to add a second electron ($\text{H} \rightarrow \text{H}^-$): an independent electron picture would in this case predict an energy $2E_0 = -27.2\,\text{eV}$. However, this picture does not take into account the non-negligible Coulomb repulsion between the two electrons, which is $U = 12.8\,\text{eV}$. The total energy is instead $E = (-27.2 + 12.8)\,\text{eV}$ $= -14.4\,\text{eV}$, or, stated in other terms, adding an electron makes the energy decrease by only 0.8 eV and not by 13.6 eV.
To obtain a picture correctly reproducing this situation one can introduce a second level, higher than the lowest one, with energy equal to $E_1 = E_0 + U = -0.8\,\text{eV}$, and

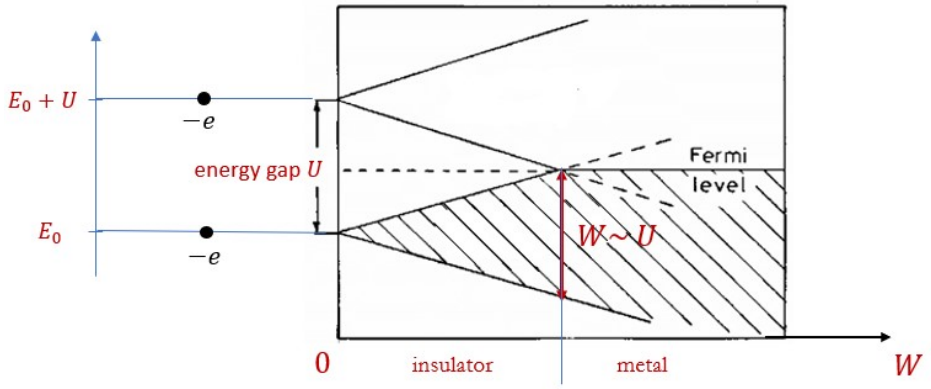

Figure 1.3: Qualitative scheme illustrating the formation of the lower and the upper Hubbard bands from the purely atomic limit (corresponding to $W = 0$). The bandwidth W increases as the interatomic distance decreases.

assume that the two energy levels can only be singly occupied. Within this picture, the added electron goes into the energy level E_1 and the total energy of H^- is correctly given by $2E_0 + U = -14.4\,\text{eV}$. We thus have two single-electron levels separated by an energy gap $U = 12.8\,\text{eV}$.

A suitable generalization of this picture is at the basis of the physics of the Hubbard model. This is easily seen if we investigate how it gets modified when we bring many atoms together to form a solid. Referring again to a linear chain of equally spaced hydrogen atoms in the ground state, i.e. with all electrons being in $1s$ orbitals, we know from band theory that each atomic energy level broadens into a band, each having a width W proportional to the interatomic wavefunction overlap. In the above picture, the two single-particle levels with energies E_0 and $E_1 = E_0 + U$ give rise to two bands, the so-called lower and upper Hubbard bands, which remain separate by an energy gap of order of U as soon as the the interatomic distance is sufficiently large, and thus the bandwidth is sufficiently small (see Fig. 1.3). The lower band thus corresponds to the energies of the singly occupied orbitals, while the upper band is representative of the energies of the electrons added to orbitals already occupied by another electron (with opposite spin). The energy gap is thus the energy to excite an electron with spin σ by removing it from a singly-occupied atom and adding to another atom already occupied by an electron with spin $-\sigma$. If the two bands overlap, this happening below a critical bandwidth of the order of U, the system will behave as a metal, otherwise will be an insulator.

As atoms get closer, lower and upper bands broaden and start overlapping as the bandwidth W becomes of the order of the on-site Coulomb repulsion U. For W larger than U the standard band theory description is recovered. In the opposite limit ($U \gg W$) specific models taking explicitly into account the electronic correlations induced by the Coulomb repulsion must be considered. The Hubbard model is certainly the simplest

(in form) and, at the same time, the most popular one.
Summarizing, the metallic or insulator behavior is determined by two competing energy scales, the kinetic energy of the electrons, giving rise to a finite bandwidth W and controlled by the overlap of orbitals belonging to neighboring atoms, and the Coulomb repulsion between electrons belonging to the same orbital, usually affected by screening effects and reduced from its value in the isolated atom. Coulomb repulsion between electrons belonging to different orbitals and/or to neighboring atoms may also be relevant, but to a first approximation its effect can be neglected compared to the one due to the local intra-orbital one.
Which are the elements where electronic correlations are important and thus cannot be neglected in theoretical models describing their behavior? Certainly they are the transition metals, having partially filled $3d$, $4d$ and $5d$ shells, the rare-earth elements (partially filled $4f$ shells), and the actinides (partially filled $5f$ shells). In these elements electronic correlations are strong since in a solid d and f orbitals remain fairly localized around the ions' nuclei, i.e. radial wavefunctions do not extend very much, this holding particularly for $3d$ orbitals, and even more for $4f$ ones (see Fig. 1.4). This implies one the one side that the overlap between two such wavefunctions belonging to neighboring atoms can be quite small, and on the other side that d and f orbitals do not behave as regular band forming orbitals, such as s and p orbitals, in the sense that they tend to retain atomic-like aspects.
Bands having prominent d and f character are usually crossed by the Fermi level: as a result, d and f electrons "hesitate" between localized and itinerant behavior. For instance, there are $4f$ compounds where the presence of local magnetic moments, as detected by a Curie-Weiss behavior of the susceptibility and typical of the insulating systems, coexists with a metallic behavior. This scenario tends to remain valid when the above elements form compounds with other elements, in particular oxides. It should nonetheless kept in mind that in a multi-electron atom there is "more" than the on-site Hubbard repulsion U, this usually corresponding to some sort of many-body problem.

1.2 Perovskites and the Ruddlesden-Popper series

Perovskites, named after the Russian mineralogist L. A. von Perovski, are compounds having the general chemical formula ABX_3, where A is a metal with oxidation state 2+, B is a metal with oxidation state 4+, and X is a nonmetal, usually oxygen, with oxidation state 2– [4]. Depending on which atoms/molecules form the structure, perovskites can show an impressive variety of interesting properties, including colossal magnetoresistance, ferroelectricity, charge ordering, spin dependent transport, high thermopower, etc., with a strong interplay between structural, electronic and magnetic properties being commonly observed in the members of the family. As a consequence,

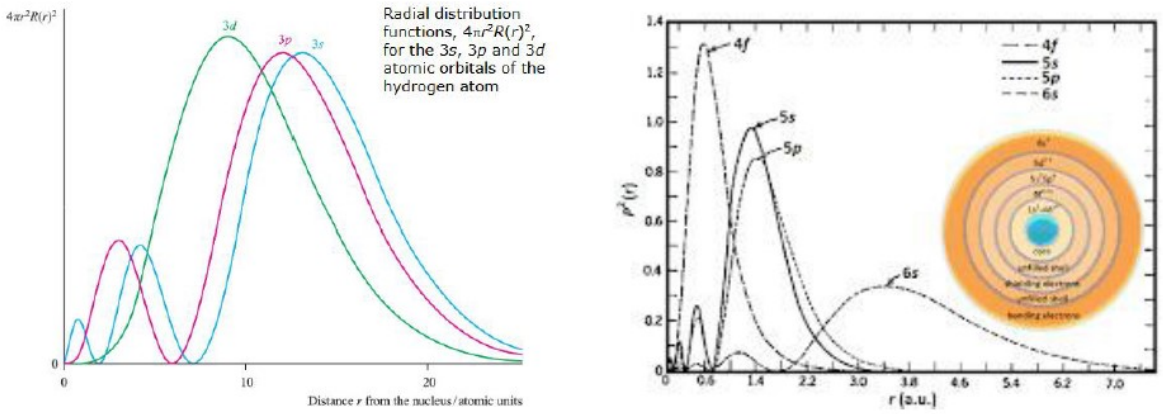

Figure 1.4: Typical radial orbital extensions.

perovskite materials exhibit intriguing and unusual physical properties that have been extensively studied both from a theoretical point of view and for potential applications to several systems, such as sensors and catalyst electrodes, certain types of fuel cells, solar cells, lasers, computer memories and spintronics devices.

A special group of systems belonging to the family of layered perovskites is the Ruddlesden-Popper oxide series, named after S.N. Ruddlesden and P. Popper [5, 6]. They consist of consecutive ABO_3 perovskite layers sandwiched between two AO rock salt layers along the crystallographic c-axis direction [7], and are described in terms of the general formula $AO(ABO_3)_n$ or, equivalently, $A_{n+1}B_nO_{3n+1}$ [8]. Here A and B are cations, commonly given by rare/alkaline earth atoms and transition metals atoms, respectively, oxygen is an anion and n indicates how many connected layers of vertex-sharing BO_6 octahedra are present in the perovskite-like structure (see Fig. 1.5). Similar to the ABO_3 perovskite oxides, the crystal structure of the Ruddlesden-Popper series can accommodate substantial amounts of oxygen at the interstitial sites, thus showing a rather high flexibility in the value of the oxygen stoichiometry. In this context, the compound Ca_2RuO_4 studied in this thesis is an example of the $n = 1$ member of a group of $4d$-based Ruddlesden-Popper ruthenates having the general formula $A_{n+1}Ru_nO_{3n+1}$ with A = Ca or Sr.

A great interest in the Ruddlesden-Popper ruthenate compounds was generated by the discovery in 1994 of superconductivity in Sr_2RuO_4 [10, 11]. Sr_2RuO_4 has a superconducting transition temperature T_c of only 1.5 K, but is still the only superconductor isostructural to the high-T_c cuprates $La_{2-x}Sr_xCuO_4$ and $La_{2-x}Ba_xCuO_4$ which does not contain copper. Unlike BCS superconductors with s-wave pairing, Sr_2RuO_4 is characterized by an unconventional superconducting phase which for some years was routinely supposed to exhibit spin-triplet p-wave pairing associated with time-reversal symmetry breaking [12, 13, 14]. This proposal, however, was recently called into question by a NMR study [15] reporting results on the behavior of the Knight shift which contradict the most prevalent theoretical interpretation of the order parameter as a

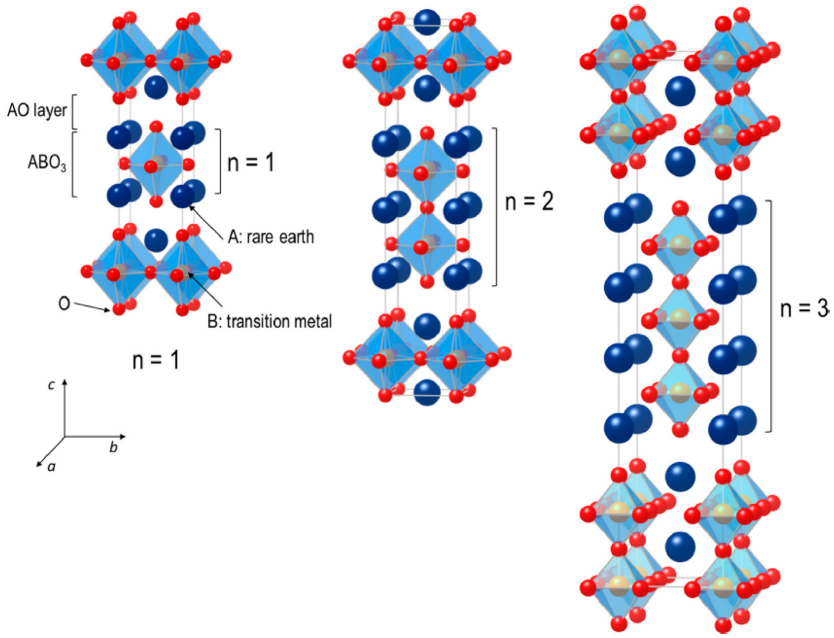

Figure 1.5: Crystal structure of the systems of the Ruddlesden-Popper series with chemical formula $AO(ABO_3)_n$. Red, blue and yellow symbols correspond to oxygen (O), alkaline or rare earth (A), and transition metal (B) atoms, respectively. The integer n denotes the number of consecutive perovskite layers (ABO_3) alternating with rock-salt layers (AO) along the crystallographic c-axis direction [8, 9].

chiral p-wave state. This technique is sensitive to the symmetry of the order parameter according to the behavior of the Knight shift upon entering the superconducting state. In Ref. [15] a substantial reduction of this quantity was found at the critical temperature, indicative of a decrease in the magnetization and therefore an absence of the spin polarization that would be expected for a triplet state.

On a more general ground, the presence in the ruthenate Ruddlesden-Popper series of ruthenium, which is a transition metal with a partially filled $4d$ shell, makes these systems belong to the general class of the correlated electron materials. However, the larger extension of the $4d$-orbitals compared to the $3d$ ones, makes the value of the intra-orbital Coulomb repulsion U not very high and usually comparable with the bandwidth W of the material. This is accompanied by a stronger p–d hybridization as well as by a stronger electron-lattice coupling, so that these systems tend to be on the border between metallic and insulating behavior and/or on the verge of long-range magnetic order. As a result, small perturbations such as slight pressure-induced lattice distortions, application of a magnetic field, small variations in the doping concentration, etc., can easily induce drastic changes in the ground state.

In particular, the physical properties of the entire Ruddlesden-Popper series critically depend on the deformations and relative orientations of the corner-shared RuO_6 octahedra that, in turn, determine the crystal field splitting and the band structure. Consequently, the fundamental features of the ground state are critically linked to the

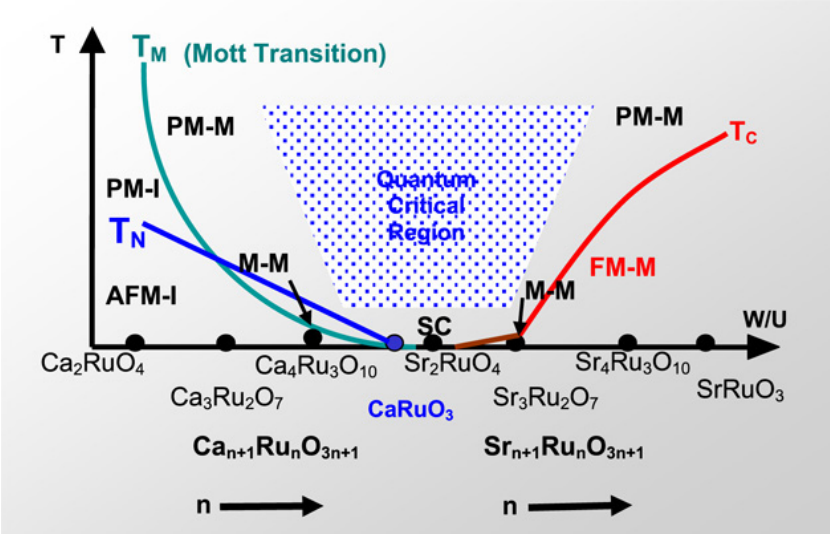

Figure 1.6: Phase diagram (temperature T vs. ratio W/U) qualitatively describing the family of compounds (Ca, Sr)$_{n+1}$Ru$_n$O$_{3n+1}$ (taken from [16]). As it is immediately seen, the ground state can be readily changed by changing the cation (Ca, Sr), and the physical properties can be systematically tuned by varying the number n of the Ru–O layers. SC stands for superconductor, FM–M ferromagnetic metal, AFM–I antiferromagnetic insulator, PM–M paramagnetic metal, M–M magnetic metal.

number n of Ru-O layers and to the type of cation (Ca or Sr): the $Sr_{n+1}Ru_nO_{3n+1}$ compounds are metallic and tend to be ferromagnetic (with Sr_2RuO_4 being an exception [10]), whereas the $Ca_{n+1}Ru_nO_{3n+1}$ compounds are all close to a metal-nonmetal transition, with a tendency to exhibit antiferromagnetism.
The great variety of ground states that one can detect by varying the relative Ca and Sr concentrations [16, 17] is effectively illustrated in Fig. 1.6. This family of compounds thus offers a relevant playground to explore a large variety of distinct electronic and magnetic phases. Interest in these correlated $4d$ systems is also motivated by the fact that they are usually characterized by a non-negligible spin-orbit interaction, this representing a fundamental ingredient in the search of novel quantum phenomena [18].

1.3 Ca_2RuO_4: general properties

1.3.1 Crystal structure and electronic properties

Synthesis and characterization of Ca_2RuO_4 began in the late 1990s [19, 20], when the extensive studies previously conducted on Sr_2RuO_4 motivated researchers to extend their investigations to other related $4d$ transition metal oxides. Despite the similarity of undoped Ca_2RuO_4 and Sr_2RuO_4, many differences in their electronic properties were soon identified. While Ca_2RuO_4 in the ground state is a Mott insulator exhibiting

antiferromagnetic order, Sr_2RuO_4 is a good Fermi liquid approximately below 25 K, becoming, as already pointed out, an unconventional superconductor below $T_c = 1.5\,\mathrm{K}$. The evolution of the ground-state properties in going from one system to another has been investigated in Ref. [21], where the authors were able to control carefully the relative concentrations of Sr and Cr in $Ca_{2-x}Sr_xRuO_4$. More details on this study will be presented in Chapter 3.

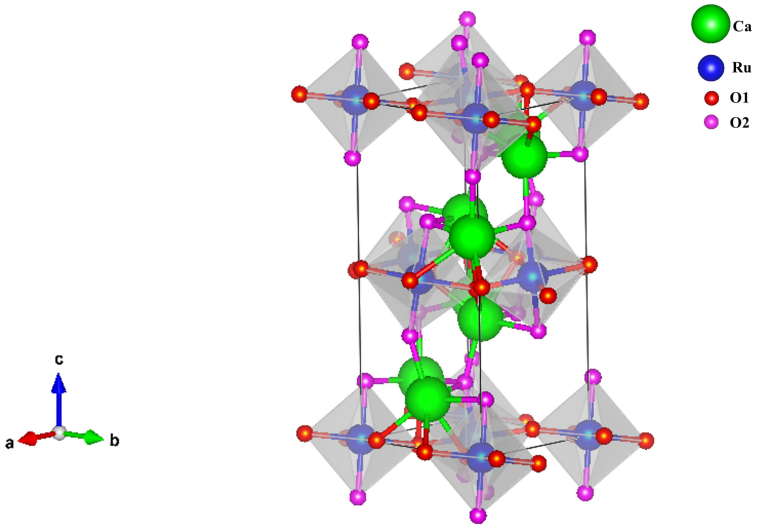

Figure 1.7: Crystal structure of Ca_2RuO_4.

As is well known, crystal structure plays a fundamental role in determining many of the physical properties of a given compound. Its fundamental feature is that the constituent units (atoms, molecules, or ions) are regularly arranged in real space with a periodic order. As a consequence, very accurate information are usually obtained by diffraction methods using X-rays, suited for superficial analysis or thin samples, or neutrons, having high penetration depth and thus more suited for bulk analysis. Experiments based on these techniques have shown that the crystal structures of Ca_2RuO_4 and Sr_2RuO_4 exhibit important differences, despite having both as fundamental structural units RuO_6 octahedra arranged in corner-shared planes alternated by layers containing the cations Ca or Sr. While Sr_2RuO_4 has a I4/*mmm* tetragonal symmetry with a unit cell containing two Ru atoms, the smaller ionic radius of Ca compared to the one of Sr ($r_{Ca} = 1.18\,\text{Å}$ and $r_{Sr} = 1.31\,\text{Å}$) leads in Ca_2RuO_4 to substantial deviations from this configuration. Actually, with respect to the ideal tetragonal structure ($a = b$, c), the RuO_6 octahedra show alternating rotations about the direction, say z, of the apical Ru-O2 bond, together with tilts of z with respect to the a-b plane initially containing the Ru-O1 bonds (x and y axes), and distortions making x and y slightly different. As a result, the unit cell of Ca_2RuO_4 is orthorhombic and contains four Ru atoms (see Fig. 1.7), the space group being the *Pbca* one. In this configuration, Ca_2RuO_4 is a Mott insulator [19, 20] with a gap estimated to be about 0.2 eV. An insulator-to-metal transition occurs at $T_{IM} \simeq 360\,\mathrm{K}$ and is accompanied by

a structural transition from an orthorombic insulating phase with a short c-axis length of the RuO_6 octahedra (*S-Pbca*), to a quasi-tetragonal metallic one with long c-axis length (*L-Pbca*) [22]. Clear evidence of this transition is given by the temperature dependence of the resistivity [22] and of the c-axis lattice parameter [23], shown in Figs. 1.8 and 1.9, respectively.

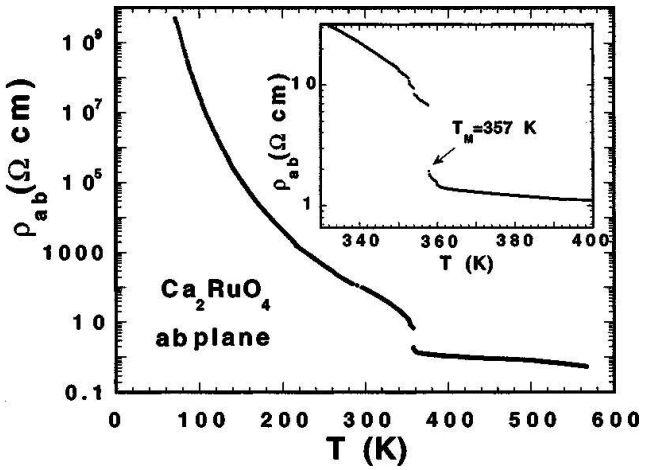

Figure 1.8: Temperature dependence of the ab-plane resistivity. The inset shows the abrupt jump at the transition occurring at $T = 357\,\mathrm{K}$ [22].

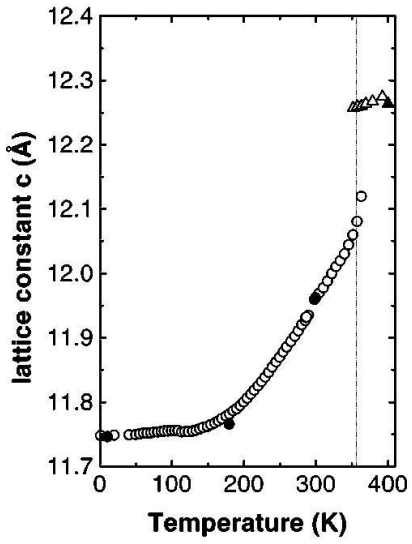

Figure 1.9: Temperature dependence of the c-axis lattice constant [23].

The a and b-axes lattice constants also vary in the transition from the metallic to the insulating phase; in particular the a-axis contracts by 1.5 % and the b-axis expands by 3 % on cooling over an interval of 250 K (Fig. 1.10). The combined effect of these thermally-induced deformations is to induce in the system an increasingly strong orthorhombic distortion that contracts the volume by 1.3 % as T is lowered from 400

K to 70 K [22, 24, 25, 26] (see Fig. 1.10). The structural transition is so dramatic to break single-crystal samples into pieces when passing from the L-structure to the S-one [27].

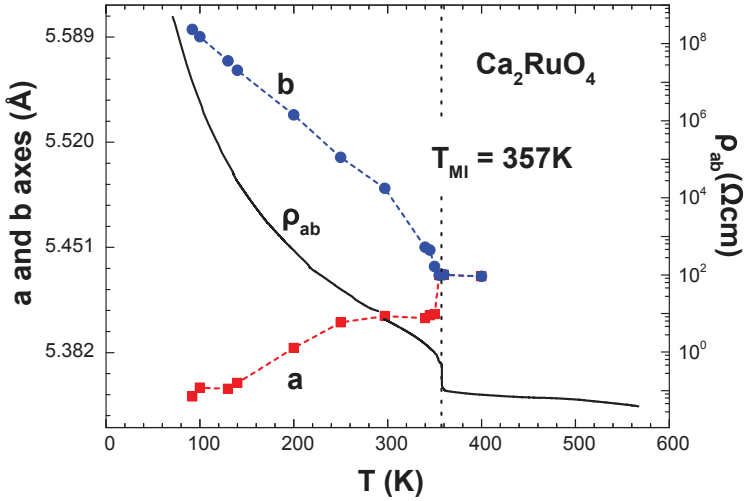

Figure 1.10: Temperature dependence of the a- and b-axis lattice constants. The ab resistivity vs. T (right scale) is also shown (adapted from Ref. [22, 28]).

The RuO_6 complex is an octahedron whose vertices are occupied by six O atoms and its center by a Ru atom. Such a type of Ru-O coordination, according to the crystal field effect, splits the d levels of the ruthenium atom in two groups: the doublet e_g, higher in energy and including $d_{x^2-y^2}$ and $d_{3z^2-r^2}$ orbitals, and the triplet t_{2g}, lower in energy and including d_{xy}, d_{yz} and d_{xz} ones (see Fig. 1.11 (a)). In the first group, e_g, the orbitals have lobes pointing directly toward the directional p orbitals of O and therefore lie higher in energy. On the other hand, in the second group, t_{2g}, the actual distances from the Ru atom of the in-plane oxygens O1 and of the apical oxygens O2 (see Fig. 1.11 (b)), denoted above by z and by x and y, respectively, determine the degree of degeneracy of the three t_{2g} levels. A perfect octahedron ($z = x = y$) leads to an exact degeneration, whereas denoting by $\overline{x}$ the average between x and y, the smaller is the ratio $\overline{x}/z$, i.e. the more elongated in the z direction the RuO_6 octahedron is, the higher in energy the d_{xy} orbital is relative to the d_{yz}-d_{xz} doublet [29].
It is well established that the low-energy properties of Ca_2RuO_4 are determined by the four $4d$ electrons of the Ru^{4+} ions. The order in energy of the t_{2g} levels, which can of course accommodate up to six electrons, is thus fundamental to establish how these electrons occupy such levels, in this way determining the transport properties of the related state. In the insulating short c-axis state ($z/\overline{x} < 1$), the orbital d_{xy} is lower in energy than the d_{yz}-d_{xz} doublet, with a crystal field gap sufficiently large that the electrons prefer to arrange in pairs in the d_{xy} level, although the local Coulomb repulsion would hinder this arrangement (see Fig. 1.12 (a)). The remaining two electrons go into the d_{yz}-d_{xz} doublet with parallel spins, according to the Hund's rule, and such a configuration, at sufficiently low temperatures, leads to an insulating antiferromag-

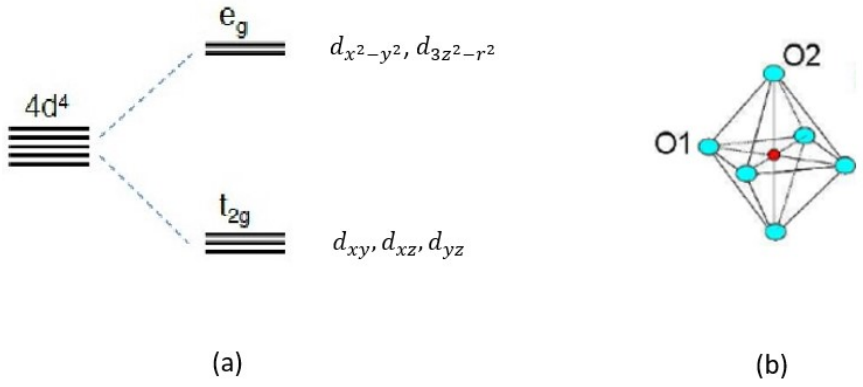

Figure 1.11: (a) Energy levels of the Ru $4d$ orbitals as splitted by the Jahn-Teller effect; (b) RuO_6 fundamental crystal unit.

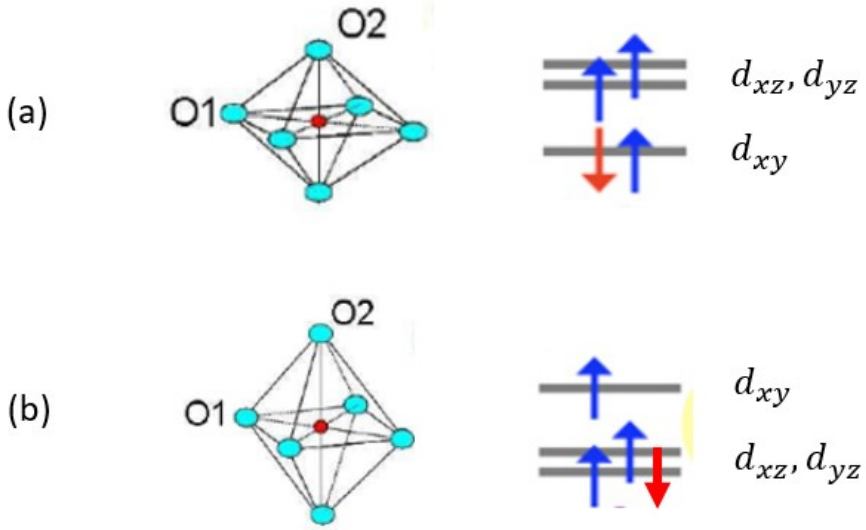

Figure 1.12: (a) RuO_6 unit and t_{2g} levels occupation in the insulating and in the metallic phase ((a) and (b), respectively).

netic state. At higher temperatures, the ratio $z/\overline{x} < 1$ gets closer and closer to 1 from below, and the three levels tend to become almost degenerate. In this situation, the strong correlations make sill behave the system as an insulator by splitting the d_{yz} and d_{xz} levels and originating from them lower, completely filled, and upper, completely empty, Mott-Hubbard bands [30, 31]. By further increasing the temperature, the ratio $z/\overline{x}$ becomes sufficiently larger than 1 to push the d_{yz}-d_{xz} doublet below the d_{xy} level in such a way to lead the system to a metallic phase. In this case, three electrons fill the lowest levels according to the Hund's rule and one electron gets free to move in the lattice (Fig. 1.12 (b)).

A further relevant element affecting the electronic properties of Ca_2RuO_4 is the spin-orbit coupling. As is well known, compared to the Coulomb repulsion U and to the crystal field potential Δ, this interaction is negligible in systems with partially filled

$3d$ shells, is strong in $5d$ systems and comparable with U and Δ in $4d$ ones. For this reason, the competition of spin-orbit coupling and crystal-field splitting in a system such as Ca_2RuO_4 that contains ruthenium, has been discussed controversially over many years [32, 33, 34, 35]. A recent study [35] seems to indicate that Ca_2RuO_4 is firmly rooted in the range of dominant crystal field, but with the spin-orbit coupling still playing an important role.
As far as magnetic properties are concerned, Ca_2RuO_4 shows canted antiferromagnetism below the Néel temperature $T_N = 110\,\mathrm{K}$ [24], originating from oxygen-mediated superexchange coupling between Ru $4d$-electrons. More precisely, neutron diffraction studies [25, 36] have shown that the in-plane alignment of the canted spins gives rise to magnetic moments that can be either parallel or antiparallel to the crystallographic b-axis, with opposite directions in two consecutive planes (A-centered mode, see Fig. 1.13). A minor antiferromagnetic phase (A-centered mode) develops between approximately 110 K and 150 K, with the spins arranged in such a way to give moments in two consecutive planes pointing in the same direction, rather in the opposite one.

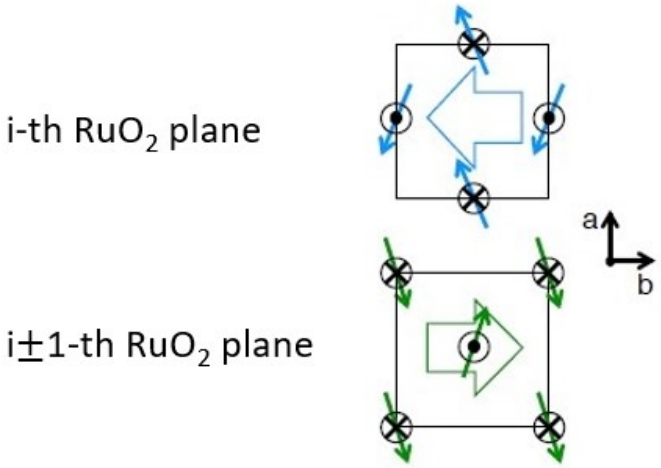

Figure 1.13: Spin configuration in the A-centered mode antiferromagnetic phase developing below $T_N = 110\,\mathrm{K}$ (adapted from Ref.[36]).

1.3.2 Current-induced Mott transition

A relevant feature shown by Ca_2RuO_4 is represented by the possibility of inducing the insulator-to-metal transition at room temperature by unusually low electric field [27] or current density thresholds [29, 37, 38, 39], approximately equal to 40 V/cm and few A/cm^2, respectively. Remarkably, these values correspond to energies significantly lower than the Mott insulating gap. This behavior is very peculiar since this kind of transition, besides being quite rare, typically occurs at low temperatures and requires

much higher voltages of the order of 1-100 kV/cm. It is also relevant that in Ca_2RuO_4 the induced metallic state can be maintained down to 4 K by simply applying a weak constant electrical current. The capacity to switch between different resistive states at room temperature with relatively weak electrical stimuli makes Ca_2RuO_4 a natural candidate for the design of specific electronic devices.
In particular, in the last few decades there has been a growing interest in developing energy-saving devices based on the control of a metal-insulator switching. This has been realized, for instance, by applying to the system under consideration the high-pressure measurements that will be briefly described in the next section. However, the apparatus allowing to achieve these high-pressure conditions is usually quite complicate and not easy to use in an efficient way. In contrast, the control of the metal-insulator switching by means of an electric field requires much simpler devices and has many advantages for practical use. In addition, electronic states investigated via a current-induced transition are controlled in a much more direct way compared with the case of the application of pressure where the control is only indirect via the change of lattice parameters.

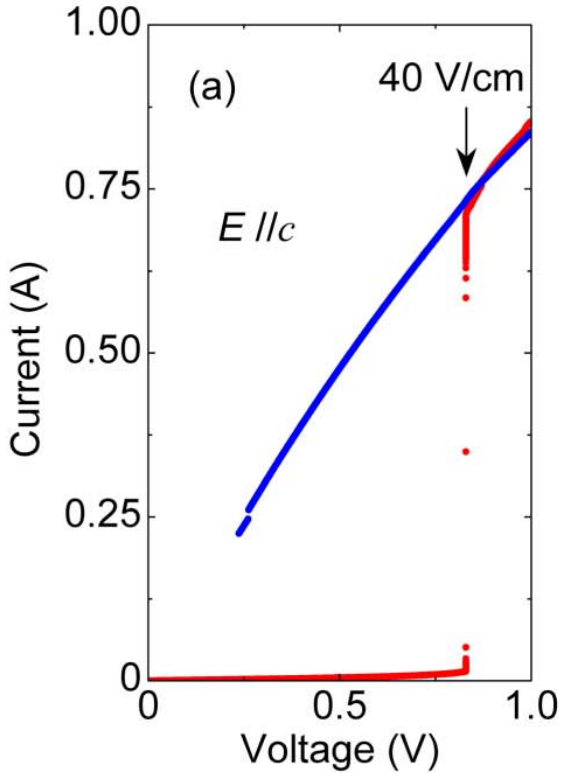

Figure 1.14: Voltage-current characteristics at $T = 295\,\mathrm{K}$, showing a large hysteresis during the voltage sweeps (from Ref. [27]).

The above-described insulator-to-metal switching is evident in the current-voltage I-V curve shown in Fig. 1.14, measured at 295 K by using a two-probe method applied to Ca_2RuO_4 single crystals [27]. We can see that initially, the increase of V along the

c-axis makes the current I rise at a slow rate corresponding to a nonmetallic behavior with a resistivity approximately equal to 60 Ω·cm. Then we have a discontinuous jump from 18 to 700 mA at 0.8 V, indicating switching, followed by a current increase at a rate typical of metallic conduction, with a resistivity $\sim 0.4\,\Omega$·cm. As already pointed out, a peculiar result is that the switching occurs at a critical value $E_{cr,\parallel}$ of the electric field very low, i.e. 40 V/cm, compared to the one found for other Mott insulators, usually of the order of MV/cm. This result remains almost unchanged when the field is applied perpendicular to the c-axis, with $E_{cr,\perp} \sim 50$ V/cm, so that we can say that the critical electrical field is almost independent of its direction [40]. If the voltage is subsequently decreased, the system exhibits pronounced hysteretic behavior. Indeed, the current decreases with V following a typical metallic behavior, but once V is reduced to about 10 V/cm, the sample breaks into several pieces. Remarkably, this does not happen in the reverse situation, when the voltage increases, before the transition from insulator to metal occurs.

The current-induced transition is accompanied by the structural change from the *S-Pbca* to the *L-Pbca* phase, as in the case of the temperature-induced transition. In analyzing the relationship between structure and electronic properties, it must be considered that in Ca_2RuO_4 the stability of the electronic phase is controlled by the effective correlation energy U as well as by the orbital degeneracy of the ruthenium ions t_{2g} levels, both of which are highly sensitive to the distortions of the RuO_6 octahedra (flattening, tilt and rotation) which produce changes in the orbital occupancy.

A clear signature of the structural transition is found in the behavior of the c-axis lattice constant as a function of the electric field, shown in the left panel of Fig. 1.15. It is observed that with increasing field, the lattice parameter, approximately equal to 11.92 Å in the *S-Pbca* phase, gradually goes up, reaching a value ~ 12.01 Å at $E_{cr,\parallel} = 40$ V/cm, where it abruptly changes to ~ 12.28 Å, signalling the transition to the *L-Pbca* phase. A similar behavior is found in the case of a temperature-induced transition (right panel of Fig. 1.15), with the important difference that once the switching occurs, the lattice parameter remains almost constant when the electric field varies from 40 to 70 V/cm, whereas it increases linearly when the temperature is raised up to ~ 640 K. This makes evident that the field-induced variation of the c-lattice constant is intrinsic and not due to heating [29, 39].

Thanks to the relatively simple electrically-driven tuning methods mentioned above, Ca_2RuO_4 attracted considerable interest from the scientific community. Although a considerable effort has been done to understand the mechanism underlying the metal-insulator transition as induced by electrical sources, fundamental issues remain open and need further investigations. To this purpose, the change of the electronic structure across the current-induced transition has very recently been analyzed by angle-resolved photoemission spectroscopy (ARPES) performed on Ca_2RuO_4 single crystals grown at the MUSA Laboratory of the CNR-SPIN unit of Salerno. This study will be presented and discussed in Chapter 3.

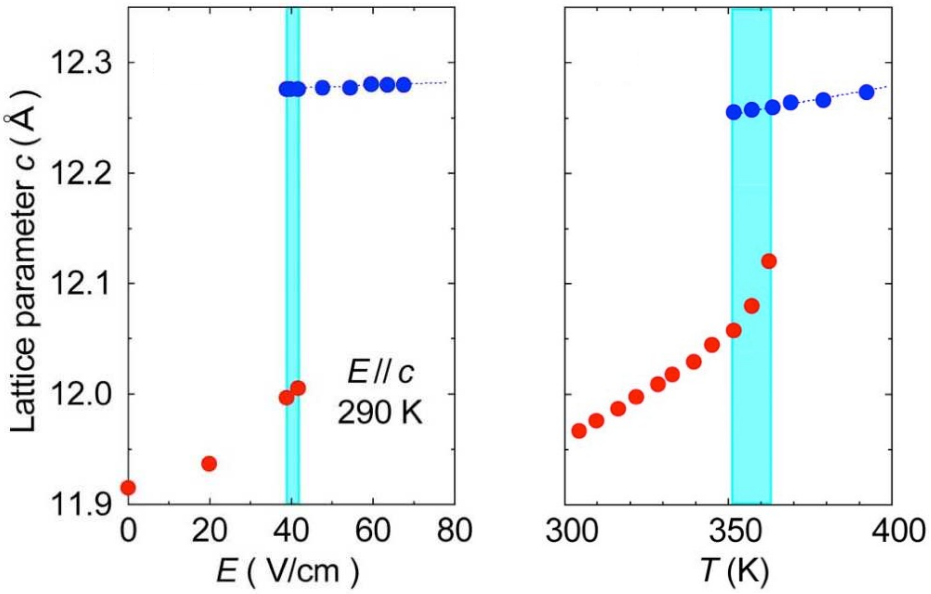

Figure 1.15: Electric-field variation (left panel, from Ref. [27]) and temperature variation (right panel, from Ref. [23]) of the lattice parameter c. In both cases the shadowed region around the transition corresponds to a mixed phase between the $S-Pbca$ and the $L-Pbca$ phase.

1.3.3 Effects of pressure and chemical substitution

Metal-insulator Mott transitions are driven by electron–electron interactions but are often accompanied by structural reorganization (see, for instance, Ref. [41]). The related interplay between electronic and lattice degrees of freedom has often been studied by applying hydrostatic pressure or uniaxial strain to the system under investigation. By acting on the relative interatomic distances, this experimental technique allows a fine tuning of the main physical properties across the transition.
In recent years, this type of analysis has also been performed on Ca_2RuO_4 by several groups [42, 43, 44, 45, 46]. A transition from paramagnetic insulator to paramagnetic quasi-two-dimensional metal has been shown to be induced at room temperature by a moderate hydrostatic pressure of 0.5 GPa (see Fig. 1.17(a)) [42]. In the metallic phase the in-plane resistivity ρ_{ab} decreases for decreasing temperature, while the one, ρ_c, measured in the c direction increases (Fig. 1.17(b)), showing a quasi-two-dimensional character similar to the one found in cuprates and in Sr_2RuO_4. Below a slightly pressure-dependent temperature falling in a range going approximately from 20 to 10 K, ρ_c starts decreasing and ρ_{ab} drops sharply to its residual value, with the system undergoing a further transition from antiferromagnetic insulator to ferromagnetic metal [42]. The metallic character of this low-temperature ferromagnetic phase has been confirmed in Raman experiments [43] and in diffraction studies [44]. The structural changes which accompany the pressure-induced transition at $P = 0.5\,\mathrm{GPa}$

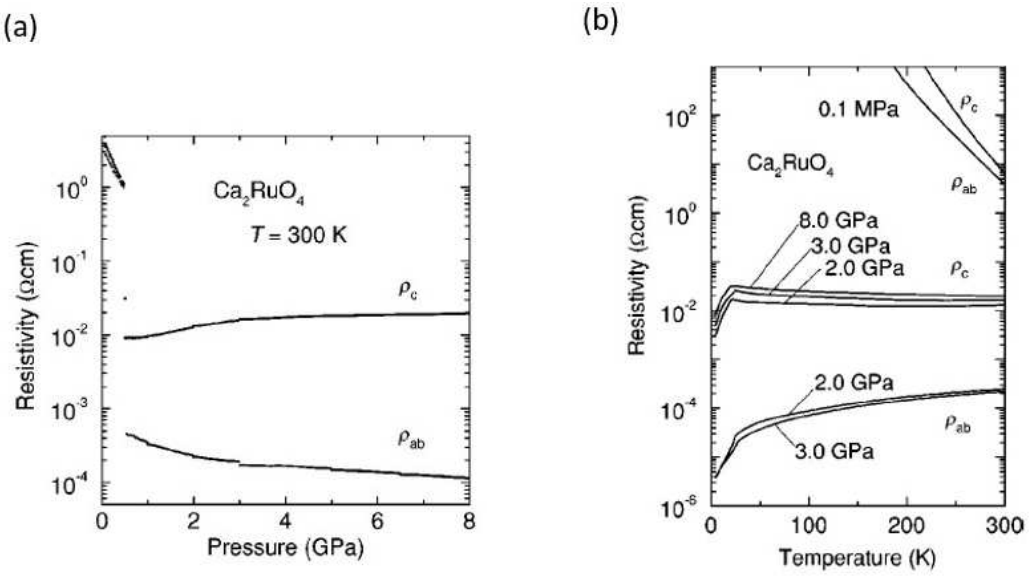

Figure 1.16: (a) Pressure variation at 300 K of the resistivities ρ_{ab} and ρ_c in the ab plane and in the c direction, respectively. The insulator-to-metal transition is signaled by the drastic fall of ρ_{ab} and ρ_c occurring at 0.5 GPa. (b) Temperature variation of ρ_{ab} and ρ_c at fixed values of the pressure (from [42]).

are a discontinuous change of both the tilt and rotational angle of the RuO_6-octahedra, with the tilt angle which gradual decreases when pressure is raised above this value. Once P reaches a values $\simeq 5.5\,\mathrm{GPa}$, the tilt almost disappears, leading the system to a phase with a higher symmetry structure [44].

It is remarkable that the transition to the low-temperature ferromagnetic metallic phase occurs at a much lower value of the pressure if one applies uniaxial strain along the ab plane, rather than doing it hydrostatically. More precisely, applying pressure either parallel to the in-plane Ru-O bond of the RuO_6 octahedra or diagonal to the Ru-O bond, it was found that the above-mentioned transition is induced at $T = 12\,\mathrm{K}$ by a pressure equal to 0.4 and 0.2 GPa, respectively [45]. The better efficiency of the uniaxial strain compared to hydrostatic pressure can be explained by noting that with an in-plane pressure the crystal is free to expand along the c direction, in this way reducing the flattening distortion which characterizes the insulating phase.

Uniaxial strain was in particular applied to lightly praseodymium-doped Ca_2RuO_4 while performing angle-resolved photoemission (ARPES) experiments [46]. Since the main interest was in the investigation of the electronic properties in the metallic phase, praseodymium was added since its main effect is to suppress the structural phase transition accompanying the metal-insulator transition, in such a way to make it occur at a critical temperature $T_{\mathrm{IM}} \sim 85\,\mathrm{K}$ for a doping level of $x = 0.07$, thus significantly lower than $T_{\mathrm{IM}} \sim 360\,\mathrm{K}$ corresponding to the undoped case (see Fig. 1.17 (a)). The transition is made evident by the temperature dependence of the resistivity shown in Fig. 1.17 (b) for different values of the praseodymium concentration. As shown in the

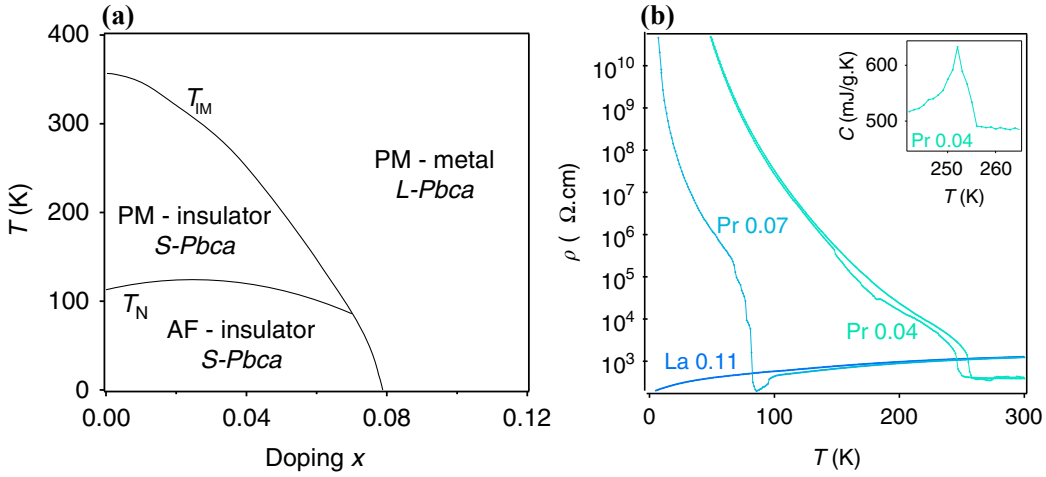

Figure 1.17: (a) Phase diagram of $Ca_{2-x}Pr_xRuO_4$ in the absence of applied pressure. (b) Resistivity curves for $Ca_{2-x}Pr_xRuO_4$ ($x = 0.04$, 0.07) and $Ca_{2-x}La_xRuO_4$ ($x = 0.11$), the latter being used as a reference for the metallic ground state. The inset shows the peak in the specific heat at the structural phase transition for $x = 0.04$ (from [46]).

inset of the same figure, a further evidence of the transition is provided by the peak in the specific heat which develops at T_{IM}.

Through careful uniaxial strain tuning, this study allowed to show that metallicity emerged from a peculiar redistribution of charge within the t_{2g} levels of the ruthenium atoms. Consistently with previous ARPES results [47], the performed experiments revealed in the insulating phase spectroscopic features associated with fully occupied d_{xy} and half-filled d_{xz}/d_{yz} orbitals, the latter being split by correlations into a filled lower and an empty upper Hubbard band. Across the strain-induced insulator-to-metal transition, the intensity of the lower Hubbard band collapses and a coherent quasi-particle peak, indicative of metallicity, appears at the Fermi energy [46]. In Chapter 3 of this thesis, the experimental procedure of growth of $Ca_{2-x}Pr_xRuO_4$ single crystals using the floating zone method is presented, together with the results of their structural, transport and magnetic characterization.

An important aspect of the pure Ca_2RuO_4 compound, already highlighted in the previous sections, is the high sensitivity of its properties to the relative energies of the t_{2g} orbitals and their electronic occupancies [21, 48]. Relevant information on the multi-band structure of Ca_2RuO_4 and in particular on the mechanism of the insulator-to-metal transition, can thus be obtained with controlled substitutions of its cations. In this context, divalent Ca has been substituted by trivalent La, which has a ionic radius only slightly larger than Ca ($r_{La} \sim 1.216$ Å vs. $r_{Ca} \sim 1.180$ Å), in order to alter the number and the occupancies of the $4d$ electron [26, 36]. The substitution of a small percentage of Ca for La, which has the advantage of leaving the original lattice structure essentially unchanged, is believed to effectively increase the t_{2g} bandwidth W by reducing the highly distorted Ru-O-Ru bond angle (151° for $x = 0$) [19], with a

simultaneous filling of the t_{2g} bands with the added electron coming from the La ion. Single crystals of $Ca_{2-x}La_xRuO_4$ were grown by the floating zone (FZ) method described in Chapter 2 [36, 46]. The need of investigating the properties of this material by using single crystals is strictly related to the strongly anisotropic character of all perovskitic materials. As one can infer from the phase diagram reported in Fig. 1.18, upon La doping both $\rho(T)$ and $T_{\rm IM}$ decrease dramatically. The non-metallic region with canted antiferromagnetic ordering shown by the parent compound Ca_2RuO_4 develops only at small doping ($0.00 < x < 0.15$), in which case the ground state is in a broad sense a Mott insulator, whereas the metallic ground state appears with increasing x ($x \geqslant 0.15$). In the non-metallic region, canted antiferromagnetic ordering

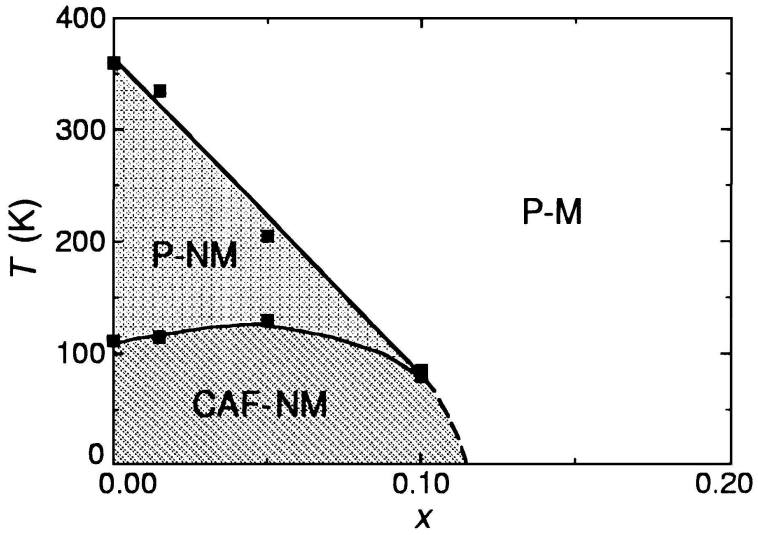

Figure 1.18: Phase diagram of $Ca_{2-x}La_xRuO_4$ single crystals. P: paramagnetic, CAF: canted antiferromagnetic, M: metal, and NM: non-metal. The insulato-to-metal transition is associated with the first-order structural transition [36].

occurs below a temperature $T_{\rm N}$ generally lower than the insulator-to-metal transition temperature $T_{\rm IM}$. For increasing values of x, $T_{\rm IM}$ approaches $T_{\rm N}$ and both vanish above $x = 0.15$.

A different doping procedure providing useful information on the pure compound consists in the substitution of Ca with Sr. Moreover, $Ca_{2-x}Sr_xRuO_4$ represents a rare case of system where the metal-insulator transition is highly susceptible to chemical pressure because of strong orbital-lattice coupling [21, 23, 49]. How the system evolves with the Sr concentration is summarized by the phase diagram in Fig. 1.19. It shows a variety of structural, magnetic and electronic phases associated to peculiar distortions of the crystal structure, which generally tend to become more and more pronounced with decreasing Sr concentration. We can see that for x slightly above the insulator-to-metal transition value ($x \simeq 0.2$), an antiferromagnetically correlated metallic region characterized by a non-Fermi-liquid behavior is observed. Besides that, at $x \simeq 0.5$ the system exhibits a crossover to a nearly ferromagnetic state, which evolves

at $x \simeq 2$ into the spin-triplet superconductor Sr_2RuO_4. The evolution with x can be explained by noting that the lattice deformations present in both pure and lightly Sr-doped Ca_2RuO_4 stabilize the insulating state by inducing an orbital polarization which gives rise to half-filled configuration near the Fermi level [30, 32, 50, 51, 52]. Different types of measurements (Raman, optical conductivity, etc.) indicate that the effective bandwidth in the insulating region is relatively insensitive to the Sr content [30, 50, 51, 52, 53]. Instead, the orbital polarization gradually relaxes with the Sr substitution, eventually vanishing at the transition in such a way to stabilize the metallic state.

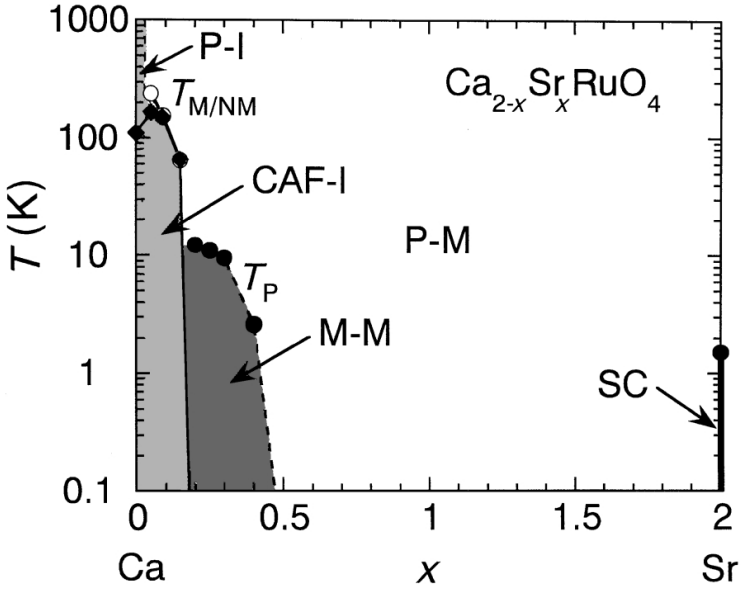

Figure 1.19: Phase diagram of $Ca_{2-x}Sr_xRuO_4$. P-M stands for paramagnetic metal, M-M for magnetic-metal, CAF-I for canted antiferromagnetic insulator, P-I for paramagnetic insulator, SC for superconductor (from [21]).

Fig. 1.20 presents the temperature dependence of the in-plane resistivity $\rho_{ab}(T)$ measured on $Ca_{2-x}Sr_xRuO_4$ single crystals grown by the floating zone method [55], for x in the range $0 \div 0.2$. While Ca_2RuO_4 is a Mott insulator at low T and exhibits a insulator-to-metal transition above 300 K [22, 25, 54], slight Sr substitution dramatically decreases the transition temperature T_{IM} to well below 300 K. The transition is clearly seen by an abrupt increase of ρ_{ab} by a factor of 10^4 as T is lowered below T_{IM}. From Fig. 1.20 we can also see that ρ_{ab} in the metallic phase and T_{IM} both rapidly decrease with x, with the system becoming fully metallic at $x = 0.2$.

1.3.4 Transition metal doping

Besides the case of doping on the alkaline metal sites, many studies have been performed in recent years on single crystals of Ca_2RuO_4 doped on the transition metal

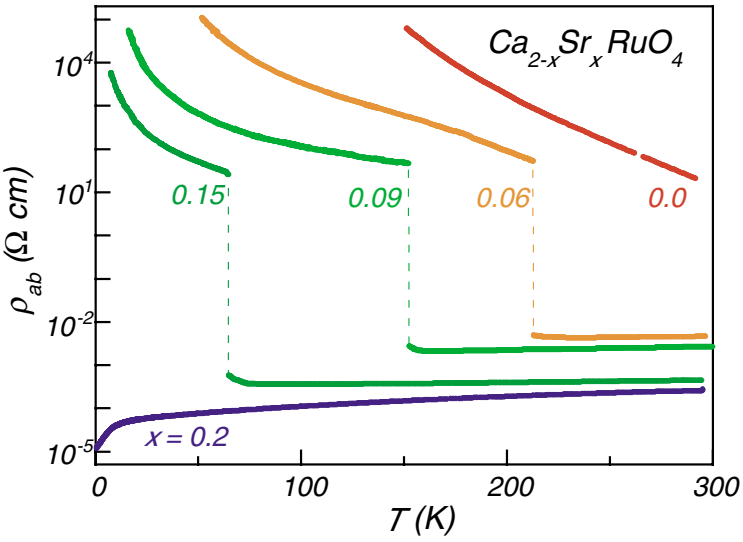

Figure 1.20: T-dependence of the in plane resistivity $\rho_{ab}(T)$ for $Ca_{2-x}Sr_xRuO_4$ [54].

(Ru) site. Single crystals of $Ca_2Ru_{1-x}M_xO_4$ with M = Cr, Mn and Fe, grown by the floating zone method, have been used mainly to investigate the transitions between the different magnetic phases induced by this kind of doping.
Figs. 1.21 and 1.22 report data from experiments performed on chromium-doped single crystals ($Ca_2Ru_{1-x}Cr_xO_4$ with $0 < x < 0.135$). From Fig. 1.21 one can see that the substitution of Ru with Cr leads to a trend opposite to that of cooling. Indeed, Cr doping reduces and eventually suppresses the orthorhombic distortion, given that $[b-a] = 0.247$ Å for $x = 0$, and $[b-a] = 0.018$ Å for $x = 0.135$ at $T = 90$ K [56, 57].

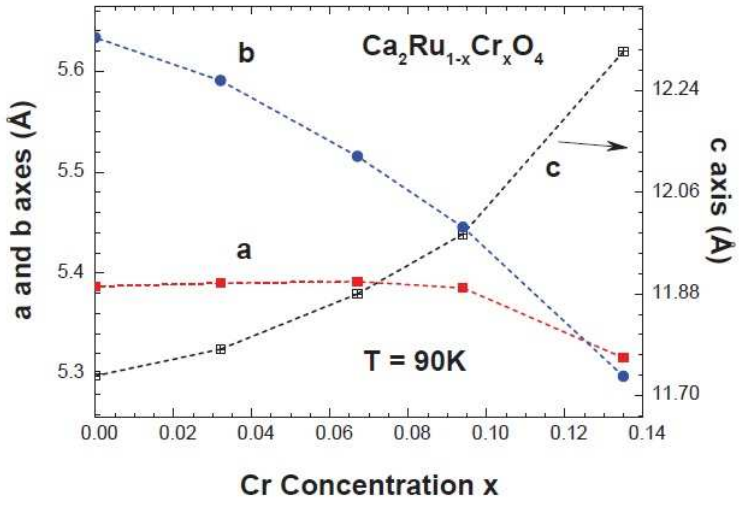

Figure 1.21: Cr concentration x dependence of the a-, b- and c-axis lattice parameters (right scale) for T = 90 K (from [56]).

With increased Cr concentration, the c-axis is considerably elongated, reflecting the

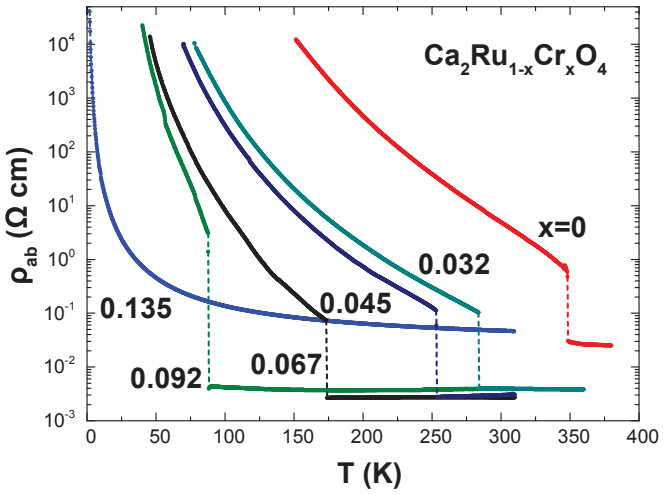

Figure 1.22: Temperature dependences of the *ab*-plane resistivity ρ_{ab} for $Ca_2Ru_{1-x}Cr_xO_4$ with $0 \leqslant x \leqslant 0.135$ (from [56]).

elongation of the RuO_6 octahedra by Cr doping. At the same time, the flattening of RuO_6 octahedra with decreasing temperature is suppressed by Cr doping. Moreover, the increase on cooling of the unit cell volume, indicative of a large orthorhombic distortion, is also shown to be suppressed when Cr doping is increased, the same happening also for the variations of the tilt, the rotation and the Ru-O1-Ru bond angle [56].

Concerning transport properties, from the jump in the temperature dependence of the *ab*-plane resistivity ρ_{ab} shown in Fig. 1.22, we can see that the critical temperature T_{IM} at which the metal-insulator transition occurs decreases dramatically upon Cr doping. From the value $T_{\mathrm{IM}} = 357$ K of the undoped case, it drops to 284 K when $x = 0.032$, with a further decrease to 81 K when Cr doping reaches the value $x = 0.092$, followed by the complete disappearance of the transition at $x \simeq 0.135$. The continuous decrease of T_{IM} with the increase of the Cr doping is directly associated with the suppression of the structural distortion discussed above. This effect competes with cooling which on the contrary tends to flatten and distort the RuO_6 octahedra, in this way making orthorombicity increase. It is also relevant that the increase with Cr doping of the Ru-O2 bond distance and the Ru-O1-Ru bond angle destabilizes the collinear AFM state, leading in turn to weak ferromagnetic behavior accompanied by spin canting [57].

Chemical substitution on the Ru site has also been used to investigate the transitions between the different magnetic phases occurring when external conditions are varied. In particular, resonant X-ray diffraction experiments have been performed [58] on manganese-doped Ca_2RuO_4 (see Chapter 3 for more details) to study the role played by structural, magnetic and orbital degrees of freedom on the mechanism driving the two distinct, so-called A-centered and B-centered, antiferromagnetic phases exhibited by this system. The methods used to control by substitutional doping the transition between these two phases are relevant since their use paves the way to the design of

specific magnetic systems by dopants engineering.
Similarly to Cr doping [56, 57], Mn doping preserves the low temperature orthorhombic symmetry *Pbca* but weakens the orthorhombic distortion by reducing the difference between the a- and b-axis ($[b-a]$ changes from 0.25 Å for $x = 0$ to 0.07 Å for $x = 0.25$) as shown in Fig. 1.23. The increasing c-axis lattice parameter with higher Mn concentration clearly indicates that Mn dopant weakens this distortion. The

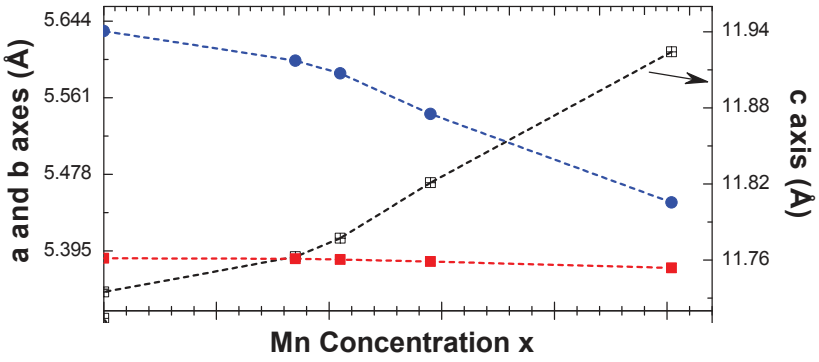

Figure 1.23: Dependence of the a-, b-, and c- lattice parameters (right scale) at $T = 90\,\mathrm{K}$ on the Mn concentration [59].

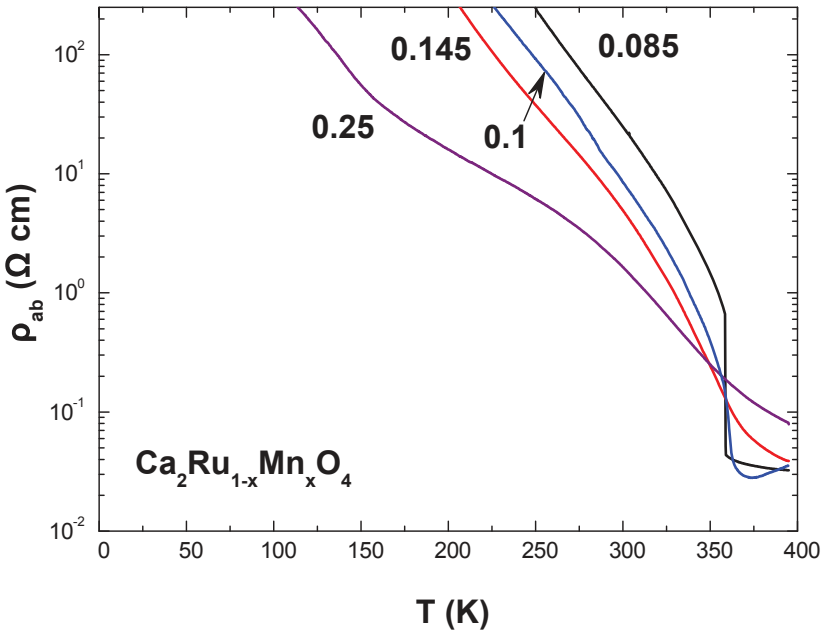

Figure 1.24: Temperature dependence of the ab-plane resistivity ρ_{ab} for $Ca_2Ru_{1-x}Mn_xO_4$ with $0 < x < 0.25$ [59].

insulator-to-metal transition temperature increases from $T_{\mathrm{IM}} = 357$ K for $x = 0$ to around 380 K for $x = 0.085$ and 0.10, but the sharpness of the transition diminishes for $x = 0.14$ and vanishes for $x = 0.25$ (see Fig. 1.24). Since the IM transition is primarily due to the structural phase transition between the high-T tetragonal to the low-T orthorhombic distortion, its broadening is more likely due to the diminishing

of the structural phase transition as Mn doping readily reduces the difference between the a- and b-axis evident in Fig. 1.23. It is remarkable that single crystals of Ca_2RuO_4 [22, 24] and $Ca_2Ru_{1-x}Cr_xO_4$ [56, 57] pulverize themselves when undergoing the violent tetragonal-orthorhombic phase transition, a unfavorable feature that is incommodious to measurements and any possible applications of the materials; in contrast, single crystals of $Ca_2Ru_{1-x}Mn_xO_4$ with $x > 0.1$ undergo a nonviolent, second-order phase transition, while retaining the other favorable underlying physical properties existent in $Ca_2Ru_{1-x}Cr_xO_4$ [56, 57]. This makes $Ca_2Ru_{1-x}Mn_xO_4$4 more desirable for fundamental studies and potential applications. Regarding the magnetic properties of the Mn-doped Ca_2RuO_4 the magnetic ordering temperature T_N systematically rises with increasing x from $T_N = 120$ K for $x = 0.085$ to 130 K for $x = 0.10$ and eventually 150 K for $x = 0.25$, as seen in magnetic susceptibility measurements [59].
Finally, let us mention that the orthorhombic distortion in Ca_2RuO_4 is also weakened by the substitution of Ru with Fe [59]. Fig. 1.25 shows the dependence on the Fe concentration of the lattice parameters at $T = 90$ K for $0.08 < x < 0.22$. Similarly to the cases of Cr and Mn doping, the orthorhombic distortion is considerably reduced when x is increased, with the a- and b-axis lattice parameters tending to get gradually closer as the Fe concentration is increased [59].

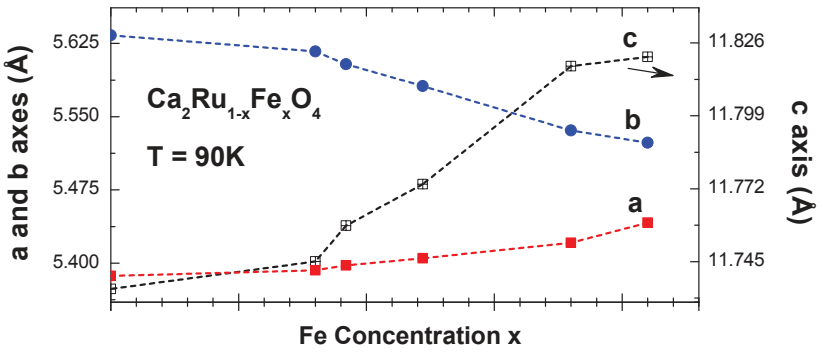

Figure 1.25: Dependence of the a-, b- and c- lattice parameters of $Ca_2Ru_{1-x}Fe_xO_4$ with $0 < x < 0.22$ at $T = 90$ K [59].

As a final consideration, we can say that comparing the three different dopant at Ru sites discussed above, the thermal expansion effect of the lattice parameter is most significant with Cr doping and becomes weaker with the increase of the atomic number. One possible explanation is that this may be due to the difference of ionic size which changes the M-O bond length, with the structure being in general more relaxed with larger ionic radii.

Chapter 2

Experimental methods

2.1 The Floating Zone Technique

The experimental research presented in this thesis was focused on the growth of single crystals of Ca_2RuO_4 doped with praseodymium (Pr) and manganese (Mn) and on their structural and morphological characterization. The single crystals were grown by means of the floating zone method (FZ) using an image furnace with two-mirrors symmetry. This method is a popular technique for growing single crystals. Particularly, it is a crucibleless process, so that the contamination from the crucibles could be avoided. The image furnace is equipped with a sealed quartz chamber, which allows the growth of single crystals to be performed in a wide range of carefully controlled atmospheres and pressures. In Fig. 2.1 a sketch of an image furnace is reported. As this 'free-standing' technique eliminates the possibility of contamination from sample holders or crucibles, the purity of the resulting crystal will be at least as good as that of the initial polycrystalline starting material [60].
Starting samples need to be in the form of polycrystalline rods, produced by reacting together stoichiometric quantities of the required starting compounds, before crystal growth can be carried out. Inside the sealed quartz tube the feed rod (upper rod of Fig. 2.1 and Fig. 2.2) is suspended using a platinum wire (which is non-reactive and has a high melting point) while the rod seed (lower rod of Fig. 2.1 and Fig. 2.2) is attached from a shaft above a crystal of either the same compound or one with similar lattice parameters.
The two ceramic rods are mounted in such a way that their tips meet at the focal point of an ellipsoidal mirrors present in the FZ furnace. Light from an halogen (or xenon) bulbs is focused by using ellipsoidal mirrors inside the furnace, creating a region of where high temperatures are gradually reached. The temperature in this region is gradually increased until both tips of rods reach their melting points. At this point the tips are brought together to make a molten zone (see Fig. 2.2), and are held to-

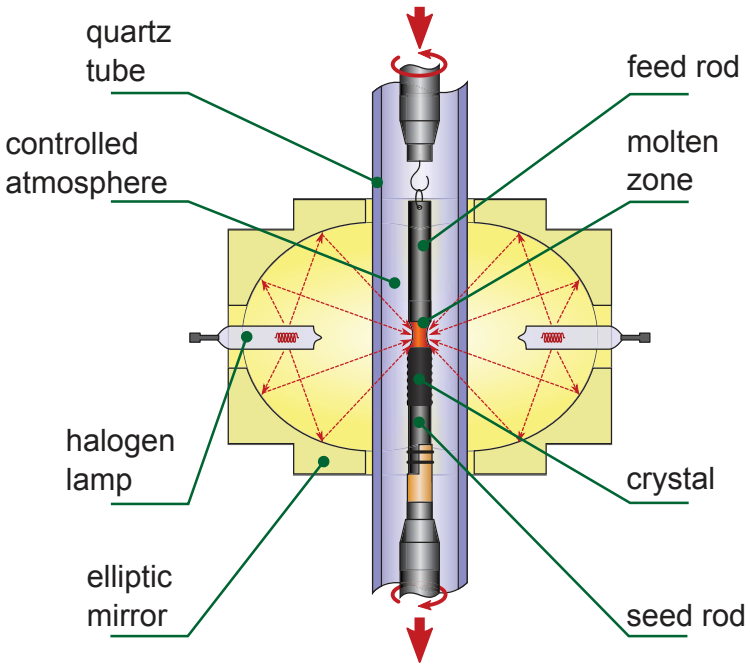

Figure 2.1: Schematic diagram of a two ellipsoid floating zone image furnace. A molten zone is formed and held between two solid rods by its own surface tension. Two elliptical mirrors enable focusing of the infrared radiation into a narrow band around the rod. Once a small section of the rod has been melted, the molten (floating) zone is translated along the sample length by moving the material with respect to the radiation focus. Crystal material is grown on the solidifying end of the float zone [28].

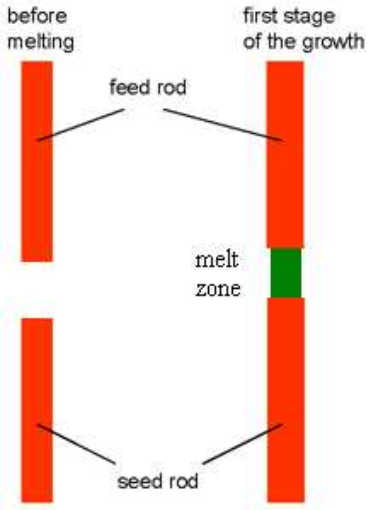

Figure 2.2: Schematic illustration of single crystal growth using the floating zone technique.

gether by the surface tension of the material. After the molten zone is created it starts moving upwards (the seed and feed setup move down). The growth then occurs at the boundary between the seed rod and the molten zone, where the microscopic preference of the cooling melt is to grow with the same symmetry as the one of the seed crystal, as schematized in Fig. 2.3 [60]. It is advisable to start the growth on a crystalline and

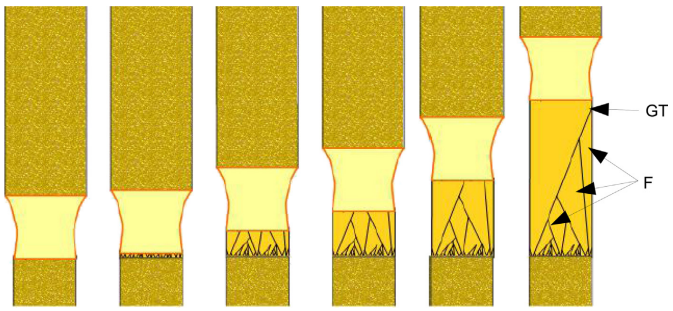

Figure 2.3: Schematic of stages of nucleation on ceramic rods and grains expansion. Individual grains can exhibit facets (F) on the crystal lateral side. After last secondary grain termination (GT), single crystal continues to grow [60].

oriented seed as this facilitates the beginning of crystallization and allows the control of the crystal orientation. Growing on a crystalline seed also prevents the absorption of liquid from the molten zone into a porous seed rod. In practice, the appropriately oriented seed is rarely available. Crystals of new materials are grown, as a rule, on ceramic seeds obtained by a time-consuming grain segregation process.

Up to now it has been pointed out that image furnaces have several control variables that can alter the produced crystal: atmosphere content, pressure, crystal growth speed, feed speed of the ceramic rod, power into halogen (xenon) lamps, rotation speed of rods. During the growth the rods rotate in opposite directions. The rate of rotation is important as it is responsible for a pattern of forced convection flows within the zone and for the defects resulting from it. The rotation speed is optimized experimentally for each material. Successful growth requires a very stable zone, where stability depends on the starting rods as well as the alignment of both the feed and the seed rods. Furthermore, the stability of the molten zone can be maintained by remotely controlling the power to the bulbs to raise/lower the temperature in the zone, and by controlling the individual rate at which each shaft is lowered. Crystal growth can be carried out in atmosphere of air, oxygen, argon or a combination of these gases. Another important factor is the alignment of the lamp because it influences the temperature distribution within the molten zone. Stability of the growth process and quality of the obtained crystal depends strongly on the stability of the zone. Stability of the gas pressure (and flow) is important for a constant temperature distribution. Furthermore, achieving a stable liquid zone requires a homogeneous, uniformly dense ceramic rod acting as the source of material for crystallization. Gas bubbles incorporated into the feed rod can seriously influence the zone, interrupting the crystal growth process. The growth of a large single crystal may typically take from some hours to several weeks, depending on the growth rate required.

The goal of growing stoichiometric crystals is often hampered by mass loss of one of the constituent components. The flux feeding floating zone (FFFZ) technique is a modification of the floating zone technique which makes it possible to grow stoichio-

metric crystals even if one of the constituent components has an high volatility [61]. The FFFZ method circumvent this problem compensating for the mass loss by increasing the initial amount of the volatile constituent that is easily lost during the growth [61, 62]. The nominal molar ratio of the constituent compounds becomes a primary variable in the FFFZ method and it needs to be optimized in order to have that the grown single crystal is stoichiometric [63].
All the single crystals Ca_2RuO_4, $Ca_{2-x}Pr_xRuO_4$ and $Ca_2Ru_{1-x}Mn_xO_4$ studied in this work were grown by the FZ technique using an image furnace with two elliptical mirrors and two 2.0 KW halogen lamps (Fig. 2.4), located in the MUSA Laboratory of the University of Salerno and SPIN Institute of the CNR. This furnace can work at temperatures up to 2200°C and its geometry guarantees an uniform temperature distribution in the horizontal direction within the zone where the crystal growth takes place.

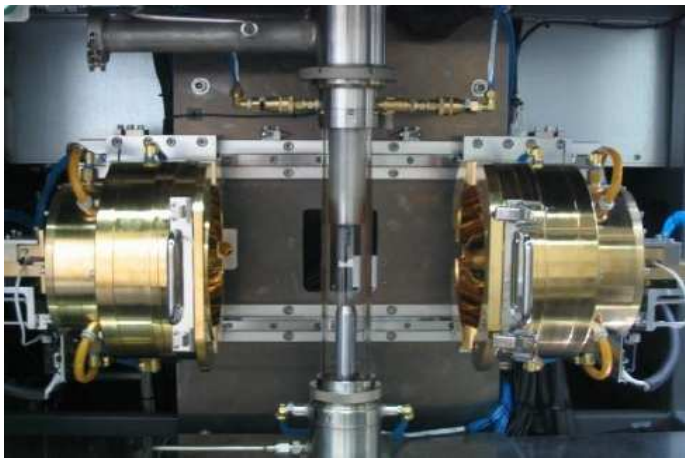

Figure 2.4: Canon Machinery image furnace with two mirrors.

The parameters involved in the growth process are: feed translation speed (V_{feed} mm/h) and seed ($V_{crystal}$ mm/h), feed rotation speed (R_{Up} rpm) and seed (R_{Low} rpm), pressure (MPa) and flow (l/min) of the gas inside the quartz tube.
As previously mentioned the crystals grown by the FZ technique have the advantage of low impurity content, high homogeneity and large size. However, high volatility of Ru makes FZ synthesis of ruthenium-based samples difficult due to at least two reasons: (1) incoming light in a focused infrared image gets obscured by volatile components which deposit on the surrounding quartz tube, this necessitating the use of relatively high rates of growth, (2) the need to use excess Ru to compensate volatility [64, 65, 66]. To avoid the darkening of the quartz tube during the growth, we successfully used a cold trap positioned close to the FZ, along with a high rate of gas flow. Moreover, the second problem was circumvented adopting the FFFZ. To ensure a stoichiometric crystal growth, an excess amount of RuO_2 was added to the feed rod [61]. This became an important growth parameter.

2.2 Scanning Electron Microscope (SEM)

The scanning electron microscope (SEM) is used to provide an enlarged image of the surface of a sample with a resolution and depth of field much higher than an optical microscope. The image is produced by making a thin electronic "brush" (beam) perform a movement of exploration (scanning) of the sample surface and representing on a computer screen the intensity of the emitted electron (called "secondary") as a function of the position [67]. The basic structure of the SEM is illustrated in Fig. 2.5.

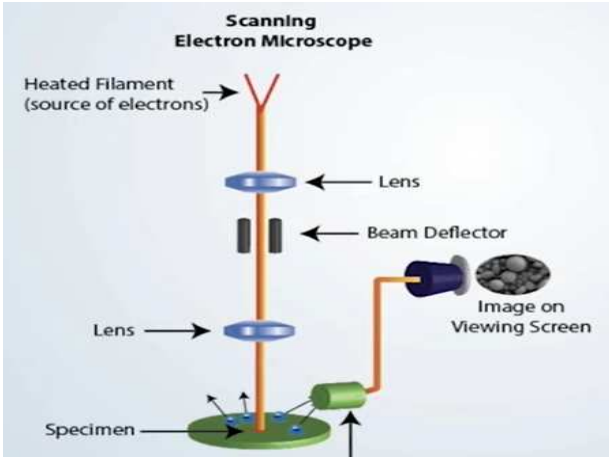

Figure 2.5: Schematic of a typical scanning electron microscope.

A cathode generates electrons which are then accelerated by the electric field existing between the cathode, held at a high negative potential, and the anode connected to ground. This device produces a beam of high-energy electrons, which is focused on the sample. The energy deposited in the sample yields a variety of signals, as depicted schematically in Fig. 2.6. Appropriate detectors are used to collect and process the various signals described above. The gun, the SEM column and the sample are kept under vacuum to decrease the contamination of the sample surface and to avoid the interaction of electrons with air particles.
Both Secondary Electrons (SE) and Backscattered Electrons (BSE) are used for imaging. Secondary electrons come from 5 - 10 nm under the sample surface, depending on the beam energy, the angle which the sample can form with the direction of the beam (tilt) and the atomic number of the material: they are the result of the interaction of the primary electrons beam and of the out-going backscattered electrons with the atoms of the sample. BSE come from a larger and deeper volume (0.1 - 0.5 μm under the sample surface): they are electrons of the primary beam rebounded after the collision with the specimen. BSE provide information about surface topography and also about the atom distribution on the sample surface identifying areas with different percentage of brightness and contrast. The backscattering coefficient is directly proportional to the atomic number Z. Then, areas containing atoms with a high average

Z appear brighter in contrast.

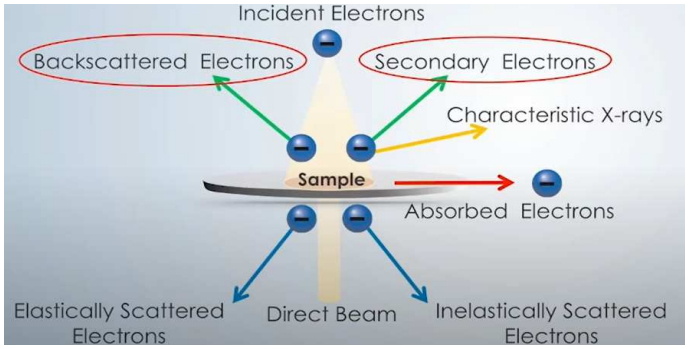

Figure 2.6: Schematic illustration of the principal results of the interaction of an electron beam with a specimen.

2.3 Energy dispersive X-ray spectroscopy

Energy dispersive X-ray spectroscopy (EDS or EDX) and Wavelength dispersive X-ray spectroscopy (WDS or WDX) make use of the X-ray spectrum emitted by a solid sample bombarded with a focused beam of electrons to obtain a local chemical analysis. All elements from atomic number 4 (Be) to 92 (U) can in principle be detected, though not all instruments are equipped for 'light' elements ($Z < 10$). Qualitative analysis involves the identification of the lines in the spectrum and is fairly straightforward owing to the simplicity of X-ray spectra [68]. Quantitative analysis (determination of the concentrations of the elements present) entails measuring line intensities for each element in the sample and for the same elements in Calibration Standards of known composition. Fig. 2.7 reports the interaction volume (i.e. how far from the surface the signal is taken out) of a sample of Cu bombarded with a beam energy of 30 keV. X-rays of the elements in the sample are generated in a volume of the order of a cubic micrometer below the surface [69]. The energy resolution of EDS is relatively poor compared to that of WDS, which leads to frequent problems of spectral interference. This is due to the fact that the wavelength of the X-photons is characteristic of the excited element and allow to identify it. In fact, each element has its own unique spectrum, with peaks corresponding to specific X-ray transition lines.
Measurements to determine the morphological and final stoichiometry of the polycrystalline and the single-crystal samples were made using a scanning electron microscope (SEM LEO-EVO 50). It is equipped with four detectors, that can detect some of the signals generated from the impact of the electron beam with the sample, at an energy of few tens of keV. The EDS system is an Oxford INCA Energy 300 and the WDS system is an Oxford INCA Wave 700 [70]. Both X-ray microanalysis systems have software for calculating sample composition.

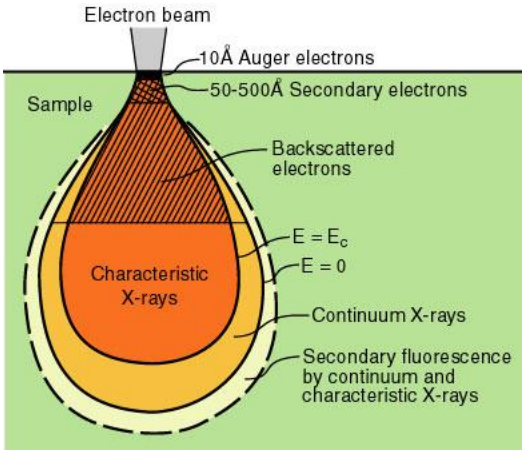

Figure 2.7: Schematic description of interaction volumes for various electron-specimen interactions [68].

Since the electron probe analyses only to a shallow depth, specimens should be well polished so that surface roughness does not affect the results. Sample preparation is essential as in the case of reflected light microscopy, provided that only vacuum compatible materials must be used.

2.4 Electron Backscattered Diffraction

Electron Backscattered Diffraction (EBSD) is a technique which allows crystallographic information (crystallographic orientations, misorientations, texture trends and grain boundaries) to be obtained from samples on a sub-micron scale in the scanning electron microscope (SEM) [71]. EBSD is a surface sensitive technique with data being acquired from a depth of the order of tens of nanometres. In EBSD a stationary electron beam strikes a tilted crystalline sample, and the diffracted electrons form a pattern on a phosphor screen. A sensitive charge-coupled device (CCD) video camera views the diffraction pattern on the screen. The CCD camera is mounted in the SEM chamber, coupled with communication hardware and a computer running the dedicate software. The principal components of an EBSD system are reported in Fig. 2.8.
Diffracted electrons escape only from a depth of the order of a few tens of nanometres deep from the sample surface. At low tilt angles, the total interaction volume close to the surface is very small compared to the interaction volume deep in the material. Consequently, at zero or low tilt, the proportion of diffracted electrons to the overall electron yield may be so low as to be undetectable. Tilting the sample improves the diffracted component to background yield ratio by increasing the volume of excited material near the surface. Thus, EBSD is generally carried out at approximately a 70-degree tilt.
In an electron backscattered diffraction, a beam of electrons is directed at a point of

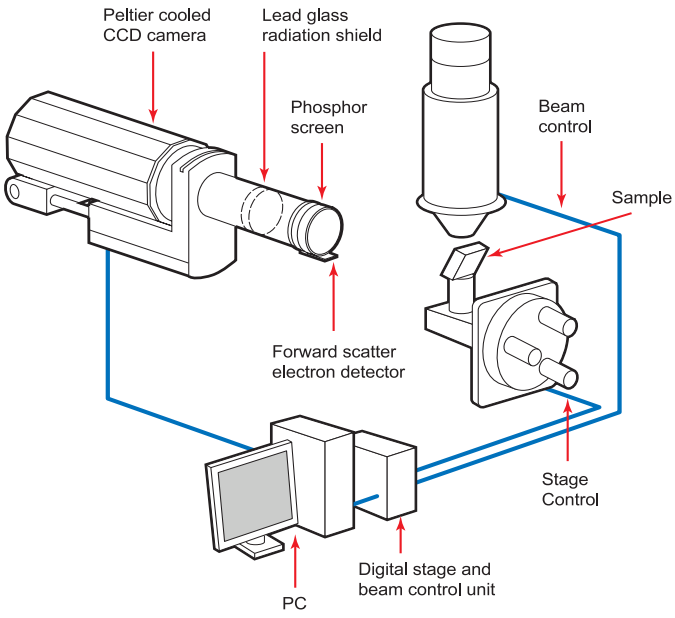

Figure 2.8: Components of an EBSD system [72].

interest on a crystalline sample in the SEM. The atoms in the material inelastically scatter a fraction of the electrons, with a small loss of energy, to form a divergent source of electrons close to the surface of the sample. Some of these electrons are incident on the atomic planes at angles which satisfy the Bragg equation:

$$n\lambda = 2d\sin\theta \tag{2.1}$$

where n is an integer, λ is the wavelength of the electrons, d is the spacing between two consecutive diffracting planes, and θ is the angle of incidence of the electrons on the diffracting plane. These electrons are diffracted to form a set of paired large-angle cones corresponding to each diffracting plane (for more details see Fig. 2.9). When used to form an image on the fluorescent screen, the regions of enhanced electron intensity between the cones produce the characteristic Kikuchi bands [73, 74] of the EBSD pattern. An example of diffraction pattern is shown in Fig. 2.10(a).
The centre lines of the Kikuchi bands correspond to the intersection of the diffracting planes with the phosphor screen. Hence, each Kikuchi band can be indexed by the Miller indices of the diffracting crystal plane which formed it. In Fig. 2.10(b) there is a indexed diffraction pattern and in Fig. 2.10(c) the unit cell orientation which generates the pattern with the corresponding crystal planes is shown. Since the diffraction pattern is bound to the crystal structure of the sample, as the crystal orientation changes the resultant diffraction pattern also changes. The positions of the Kikuchi bands can therefore be used to calculate the orientation of the diffracting crystal [75]. So, in a EBSD analysis the electron beam is scanned over the sample on a grid of points, and at each point a diffraction pattern is obtained and the crystal orientation is measured. The resulting data can be displayed as a crystal orientation map and

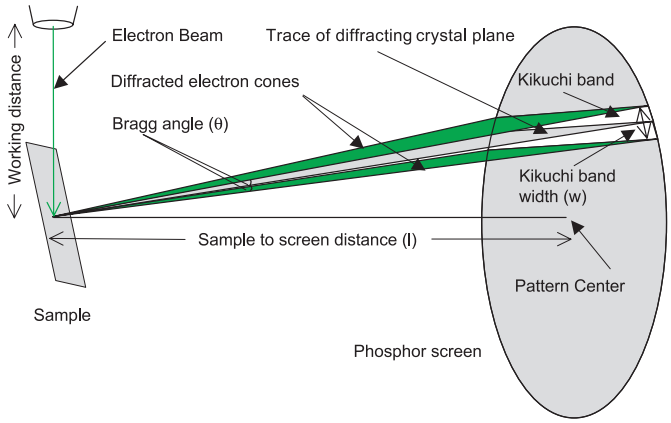

Figure 2.9: Formation of the diffraction pattern [72].

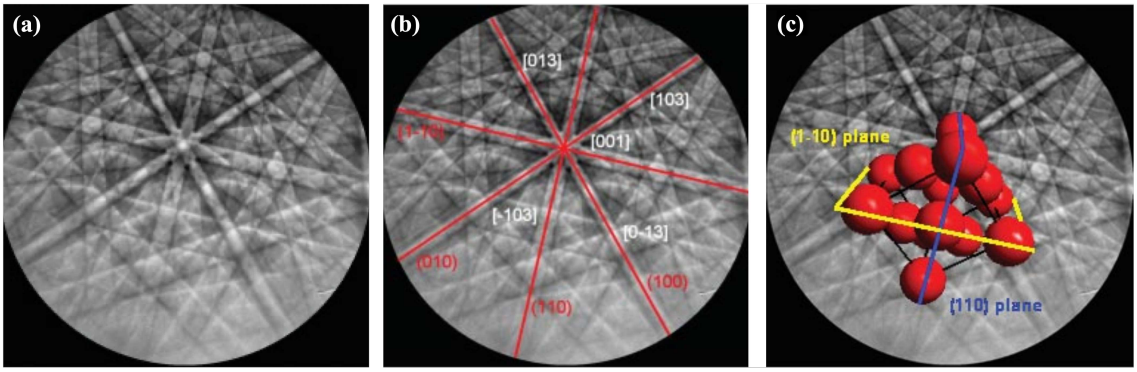

Figure 2.10: (a) A diffraction pattern from nickel collected at 20 kV accelerating voltage and (b) its indexing. The Kikuchi bands are labelled with the Miller indices of the crystal planes that formed them (red) and the crossing points of the bands are labelled with the zone axis symbol (white). (c) The nickel unit cell orientation which generates this pattern with the corresponding crystal planes shown. [72].

processed to provide a wide variety of information about the sample microstructure. Large sample areas can be measured by automatically moving the SEM stage between successive maps.

2.5 X-ray Diffraction

The structure and symmetry of a single crystal play a major role in determining many of its physical properties, therefore their knowledge provides a fundamental tool for studying the physical and chemical properties of materials. The key feature of a crystal is that the constituent units (atoms, molecules, or ions) are arranged with periodic order. This property can be conveniently investigated by diffraction methods. Fig. 2.11 shows two X-ray beams incident on a family of parallel atomic planes of a crystal, separated by the distance d. When a crystal is bombarded at given incidence

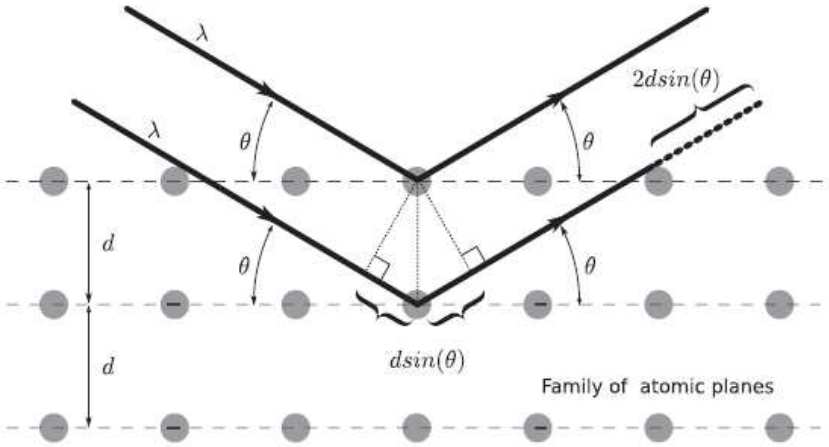

Figure 2.11: Illustration of the fulfilment of the Braggs'equation [76].

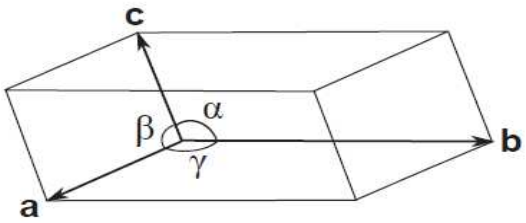

Figure 2.12: 3−dimensions showing cell parameters [76].

angles with X-rays of fixed wavelength (of the order of d), intense reflected X-rays are produced when the scattered X-rays interfere constructively [76]. In order for this to happen, the differences in the travel path must be equal to integer multiples of the wavelength. When this constructive interference occurs, a diffracted beam of X-rays will leave the crystal at an angle equal to that of the incident beam. The general relationship between the wavelength of the incident X-rays, the angle of incidence and the spacing between the crystal lattice planes is known as Bragg's Law [77], expressed as:

$$n\lambda = 2d\sin(\theta) \tag{2.2}$$

Here d is the distance between two consecutive lattice planes, λ is the wavelength of the incident X-rays, θ is the incident angle (Bragg's angle) and n is an integer. This law relates the wavelength of the electromagnetic radiation to the diffraction angle and the lattice spacing in a crystalline sample. By changing the geometry of the incident rays, the orientation of the centered crystal and the detector, all possible diffraction directions of the lattice can be attained.

In crystallography, periodic crystals are defined as solids with long-range 3-dimensional internal order, and each unique piece of the 3-dimensional array is called a unit cell. The latter is delimited by three pairs of parallel planes, and thus is defined by six parameters, namely three axial lengths a, b and c and three inter-axial angle α, β and γ (Fig. 2.12).

The sets of parallel atomic planes that reflect X-ray beams can be chosen in different ways. However, these planes must intersect all the ions of the lattice, and thus the intercepts can be at 1/0, 1/1, 1/2, 1/3, $\cdots$, $1/n$. The conventional way of describing the orientation of these families of planes is with *Miller indices* written in the form (hkl) specifying that the plane makes the intercepts a/h, b/k and c/l with a unit cell (h, k and l are three integers). The orientation of the planes can also be represented by vectors normal to the scattering planes. The direction of each vector is denoted by square brackets containing the Miller indices of the set of plane. For example [100] corresponds to a vector normal to (100) planes.
The study of the structural properties of our samples has been performed by X-ray diffraction using a Bruker D2-PHASER-2nd-generation. X-ray powder diffractometer with CuK_{α_1} radiation ($\lambda \sim 1.54056$ Å) was used. The $\theta - 2\theta$ scans are recorded from 10° to 70° using a step of 0.02° and a counting time of 5 s for each step. Data are processed using PANalyticals HighScore Plus suite and Inorganic Crystal Structure Database.
Moreover the the quality of the grown crystals in this work was assessed by a high-resolution X-ray diffractometer (Panalytical, model X'Pert PRO) equipped with a four circle cradle. The incident beam is generated by a X-ray tube focusing a CuK_{α} radiation with $\lambda = 1.5406$ Å on the sample by an asymmetric four crystal Ge(220) Bartels monochromator followed by a graded parabolic Guttman mirror. The diffracted beam reaches the detector with an angular divergence of 12 arcsin crossing a triple axis attachment and undergoing three (002) reflections within a channel cut Ge Crystal [63, 78]. In this instrument the sample can be tilted in ψ and rotated in φ besides being moved in ω and 2θ. Here ω represents the angle between the sample surface and the incident beam, 2θ the angle between the incident and diffracted beams, φ the rotation angle around the normal to the sample surface, and ψ the tilt angle about a line in the sample surface normal to the ω and 2θ axes. By changing the plane exposed to the beam, one can acquire three linearly independent scans around appropriate reflections satisfying the Bragg law and calculate the lattice parameters of the sample.

2.6 Resonant elastic X-ray scattering (REXS): a brief introduction

In the study of complex materials, resonant elastic X-Ray scattering (REXS) provides a sensitive probe for the analysis of spatial modulations of spins, charges, and orbitals [79].
REXS is concerned with the detection and the analysis of scattered X-Rays intensities from sample materials when the X-Ray energy is tuned near absorption edges of the

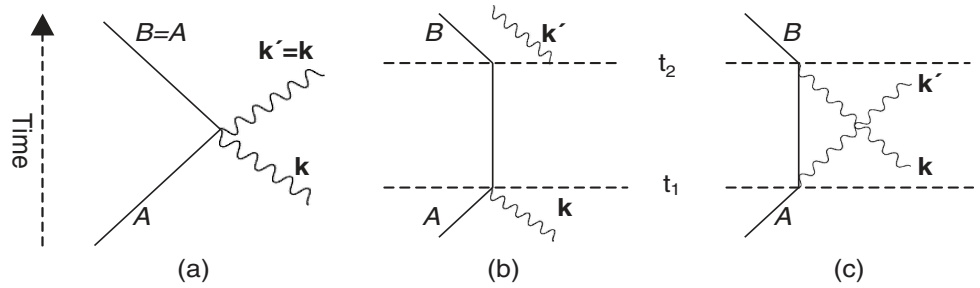

Figure 2.13: Feynman diagrams for X-ray interaction with electrons. The time lines are shown with dashed arrows. Solid lines are electron paths and wiggles are photon paths. In all three cases, electrons in an initial state A end in a final state B. [82]

material components. It involves virtual transitions from core levels into unoccupied states close to the Fermi level which depend strongly on the spin, charge and orbital configuration of the resonant scattering centers [80]. Furthermore, the resonance process strongly enhances the scattering cross-section and allows the study of selected atomic species present in a crystal.

A unique feature of REXS is that it is both element- and orbital-specific. In fact, the chemical sensitivity comes from the element specificity of the absorption edges, whereas the choice of the absorption edges allows the selection of the electronic core level to be excited, with different final states that can be probed through multiple transitions. In addition, REXS is a sensitive probe of multipolar moments, which allows, through the application of symmetry arguments, to distinguish between magnetic and non-magnetic effects. It is also relevant that REXS intensities exhibit a dependence on the photon energy that contains information about the relevant energy scales in the system. Because of its extreme sensitivity to symmetry [81], REXS exploits the polarization of the X-Ray beams, so both linear and circular polarization are considered. Furthermore, the dependence of REXS on the scattering geometry allows to probe the symmetry of local fields by varying their orientation with respect to the scattering plane (azimuthal scan).

In a REXS process, X-Rays are emitted as well as absorbed. Therefore, both absorption and emission events must take place. There are three pathways on how a scattering event can occur. They can be illustrated in the Feynman diagrams shown in Fig. 2.13. In case (a), an X-Ray photon with momentum **k** interacts with the electron in initial state A but is immediately re-emitted with momentum **k'**, leaving the electron in the same state A. Therefore, the photon energy cannot change as long as the total energy is conserved. In case (b), a photon is first absorbed at time t_1 but a photon with a momentum **k'** is emitted at a later time t_2. In case (c), the electron emits a photon first and absorbs at later time. This process is not as important as the other two since the probability of such a process under ordinary conditions is small.

In order to perform resonant scattering, a tunable energy X-Ray source is required. Conventional X-Ray sources rely on the deceleration of electrons on collision with an

anode and produce X-Rays predominantly at energies characteristic of the anode material (usually tungsten, molybdenum or copper). In addition, lower intensity X-Rays are produced over a wide spectrum where the high energy cut off is determined by the accelerating voltage. Although early determinations of REXS scattering factors were derived from such sources, the advent of synchrotron radiation providing sources of tunable X-Rays energy marked an explosion in the field of REXS research. In fact synchrotron sources offers the possibility of having highly tunable X-Ray beams, good energy resolution and efficient instrumentation.

2.7 Angle-Resolved Photoemission Spectroscopy

Knowledge of the electronic band structure is essential to explain many physical properties of solids, and serves as the foundation for understanding all solid-state devices. The formation of electronic bands is mainly from the overlapping of the wavefunctions of the outermost electrons (valence electrons) of the atoms and molecules. The electronic band structure is itself a property of the crystal, and as a result possesses the symmetry of the crystal [83]. One of the most suitable and widely used techniques to study the electronic structure of a material is the photoemission spectroscopy (PES) [84]. Based on the photoelectric effect as explained by Einstein in 1905 [85], photoelectrons are created via the interaction between the irradiating photons and the sample. Shown in Fig. 2.14(a) is the schematic of PES. The electrons are excited by the incident photons on the sample, and if the excited electrons have sufficient energy to escape to the vacuum, they can be detected by an electron energy analyzer.
In a simple model which does not take into account any energy loss during the photoemission process, the total energy must be conserved. This implies that the kinetic energy of the emitted electrons is given by [87]:

$$E_K = h\nu - E_B - \Phi \tag{2.3}$$

where $h\nu$ is the photon energy, E_B is the binding energy of the initial state of the electron with respect to the Fermi level, and Φ is the work function of the material, corresponding to the potential barrier at the surface that the electron must overcome to be photoemitted. Photons with a known energy are used to excite electrons out of the sample in a PES experiment. The kinetic energy and the momentum of the excited electrons can be measured by an electrostatic analyzer placed close to the surface. As indicated in Fig. 2.14(b), in the schematic representation of PES, the photoelectrons come from the occupied energy levels, including the valence bands (VB) and the core-level states which correspond to the closed atomic shells. Moreover, as shown schematically in Fig. 2.14(b) there are secondary electrons excited by the photoelectrons that define the vacuum level cutoff [88]. The PES is a very surface-sensitive

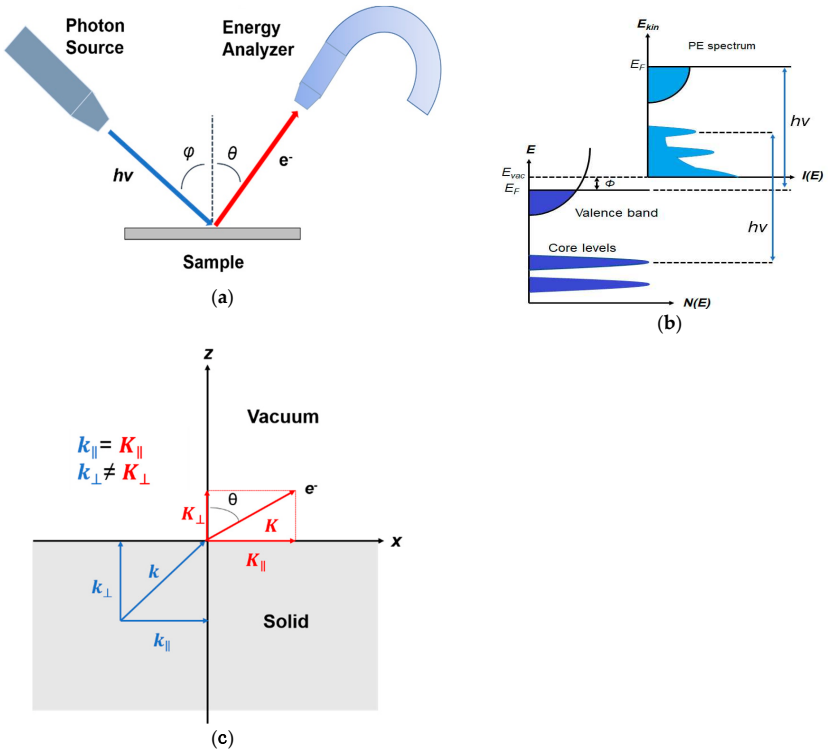

Figure 2.14: (a) Schematic of a photoemission experiment. The electrons are excited by the incident photons on the sample, then the excited electrons escape to the vacuum and are detected by an electron energy analyzer. (b) Schematic representation of photoemission spectroscopy (PES). The photoelectrons are excited from the occupied energy levels, including the valence bands as well as the core-level states. Additionally, secondary electrons excited by the photoelectrons that define the vacuum level cutoff are shown. (c) Photoemission geometry and relation of the electron wave vectors in vacuum ($\boldsymbol{K}$) and in solid ($\boldsymbol{k}$). Note that only the parallel momentum component is conserved [86].

technique, i.e. the electrons are emitted from the most superficial layers of the material.

In a photoemission process, not only the energy but also the momentum can be detected. The energy band dispersion $E(\mathbf{k})$ of a crystalline sample can be obtained if the momentum of the photoelectrons is also measured in addition to the kinetic energy with an angle-resolved electron energy analyzer. This technique is named as angle-resolved photoemission spectroscopy (ARPES) [89, 90].

Fig. 2.14(c) shows the photoemission geometry, illustrating the relation of the electron wave vectors in vacuum ($\boldsymbol{K}$) and in solid ($\boldsymbol{k}$). For the final states in the solid one can assume a free-electron-like dispersion, and the energy of the excited electrons before escaping the surface is:

$$E_k = \frac{\hbar^2 \boldsymbol{k}^2}{2m^*} + V_0 \tag{2.4}$$

where m^* is the effective mass of the photoexcited electron in the final state, V_0 is the potential step to be overcome by the photoexcited electron to leave the surface. When the electrons exit the surface to enter the vacuum, the measured kinetic energy E_K is

described by the following expression [86]:

$$E_K = \frac{\hbar^2 \boldsymbol{k}^2}{2m^*} = \frac{\hbar^2 \left(\boldsymbol{K}_\parallel^2 + \boldsymbol{K}_\perp^2\right)}{2m_0} \tag{2.5}$$

where m_0 is the free electron mass, $\boldsymbol{K}_\parallel$ and $\boldsymbol{K}_\perp$ are the surface normal and parallel components of the wave vector $\boldsymbol{K}$ in vacuum, respectively. If the angle of emission with respect to the surface normal is θ, then the two components are:

$$\boldsymbol{K}_\parallel^2 = K \sin\theta \qquad \boldsymbol{K}_\perp^2 = K \cos\theta \quad . \tag{2.6}$$

Note from Fig. 2.14(c) that the parallel momentum component is conserved ($\boldsymbol{k}_\parallel = \boldsymbol{K}_\parallel$), while the perpendicular momentum component is not ($\boldsymbol{k}_\perp \neq \boldsymbol{K}_\perp$). Thus, the surface parallel and normal components of the momentum of the photoexcited electron in the solid can be expressed as:

$$\hbar \boldsymbol{k}_\parallel = \sqrt{2mE_K} \cdot \sin\theta \tag{2.7}$$

$$\hbar \boldsymbol{k}_\perp = \sqrt{2m\left(E_K \cos^2\theta - V_0\right)} \tag{2.8}$$

where m can be taken as m_0 if the final state is of high enough energy. The band dispersions along the $\boldsymbol{k}_\parallel$ or the $\boldsymbol{k}_\perp$ direction of the sample can be measured by varying the emission angle θ or the incident photon energy to tune the electron kinetic energy E_k.

Typical photon sources for ARPES are He lamp and synchrotron light source [84]. A He lamp is a laboratory-based light source emitting photons at fixed energies (He I at $h\nu = 21.2$ eV, and He II at $h\nu = 40.8$ eV). A synchrotron light source is much more versatile with adjustable monochromatic photon energies, this being essential to reach the whole Brillouin Zone.

In this thesis the Nano-ARPES technique was used (see Chapter 3). This technique focalizes the photon beam on sample areas of the order of up to hundreds of nanometers, allowing the study of the electronic structure in sample domains having sizes that conventional ARPES cannot reach [91].

Chapter 3

Results

Availability of pure high-quality single crystals is crucial for the study of the intrinsic properties of most solid-state systems. This is particularly true for the ruthenates of the Ruddlesden-Popper series, $Ca_{n+1}Ru_nO_{3n+1}$, which, as discussed in Chapter 1, have a layered-type structure, and therefore exhibit strongly anisotropic properties which can be measured reliably only on single-crystal samples. Besides, these compounds must be free of structural defects, impurities or undesired phases which can drastically change the properties of the material. In Chapter 1 we showed how the IMT transition in Ca_2RuO_4 can be tuned and/or suppressed with doping. Crystal growth of ruthenate compounds has been carried out since the 1990s and has been the subject of many works [15, 19, 28, 46, 92]. Most of the studies on high-quality single crystals consist of well-controlled growth procedures carried out on high-temperature solution in which particular care has been paid to avoid the inclusion of impurities or spurious phases. This Chapter aims to illustrate the crystal growth procedure used to synthesize praseodymium- and manganese-doped Ca_2RuO_4 crystals by the floating zone method. To identify the optimized growth parameters and to select crystals appropriate for synchrotron experiments, as REXS and ARPES, the grown crystals have been carefully characterized, as described below. Indeed, the morphological, compositional, structural, electric and/or magnetic properties of crystals obtained using different growth parameters have been routinely investigated.

The surface of the crystals was inspected by polarized-light optical microscope (PLOM, Nikon model ECLIPS LV100ND); image analysis was performed by Imaging Software Nikon NIS Elements. Scanning electron microscopy (SEM) (LEO, model EVO 50) was also used to investigate the morphology of the crystals. To probe the sample composition, elemental analysis was carried out by energy dispersive spectroscopy (EDS) (Oxford INCA Energy 300); the composition was obtained by averaging the values of three measurement points; maps of elements were also acquired to investigate the elemental distribution. X-ray diffraction (XRD) measurements were performed at room temperature employing both a D2 phaser diffractometer from Bruker and a X'Pert

MRD diffractometer (Philips) using monochromatic CuKα with the same configuration described in Ref. [63]. The XRD spectra were acquired on cleaved samples in the 2θ range from 5° to 80°. The crystal microstructure of thoroughly polished crystals was analyzed by means of electron back scattered diffraction (EBSD), (for details see Chapter 2). The EBSD measurements were performed using an Inca Crystal 300 EBSD system added to a SEM LEO (Zeiss, model EVO 50) with a LaB_6 gun. EBSD was carried out using an acceleration voltage of 20 kV, beam current of ∼5 nA, and a working distance of ∼20 mm.
Each specimen was mounted with phthalic glue, and polished with progressively finer diamond suspension from 3 to 0.05 μm. For each diamond suspension polishing proceeded for 30-60 minutes, until a smooth, reflective surface was observed. After the final polishing step, the specimens were removed from the glue with acetone.
Electrical resistance and $V - I$ characteristics as functions of T were measured by the two-terminal method applying a current bias to the crystals along the c-axis direction, as described in [29, 39, 40]. The current was applied using a Keithley 2635 SourceMeter, while a Keithley 2182A Nanovoltmeter was used to read the voltage drop. Since the resistance values of the crystals are high compared to the ones of the wiring and the contacts, the two-terminal method does not affect the measurement accuracy. Considerable effort was put into making the electrical connections on the samples to reduce the contact resistance and thus avoid local Joule heating. The best method we found to have a suitable contact adhesion was to use Indium pads squeezed on the sample surface together with gold wires. However, in some cases, due to the very small sample dimensions (few mm^2), this method was not applicable. In that case, to connect the gold wires on the sample, a conductive silver epoxy glue was used. Finally, DC magnetic measurements were performed employing a 9 T Physical Properties Measurement System (PPMS) by Quantum Design, equipped with an AC Measurement System (ACMS) insert, using the DC extraction method.

3.1 $Ca_{2-x}Pr_xRuO_4$

3.1.1 Crystal growth of $Ca_{2-x}Pr_xRuO_4$

Performing single crystal growth with the FZ technique takes a long time because the process parameters to control, as described later, are many. Furthermore, for the growth of crystals with Ru a further parameter must be considered, that is, the excess of Ru in the starting material. This was necessary because of the RuO_2 high volatility [93, 94]. Here, we focused on the growth of single Ca_2RuO_4 crystals doped with 4% of Pr because, as said in Chapter 1, with this doping the metal-insulator transition temperature goes down to $T_{IM} \sim 250$ K which is lower than room temperature. This

allows us to obtain crystals of larger dimensions than those of pure compound, more suitable for advanced characterization, like Angle-resolved photoemission spectroscopy (ARPES) and neutron measurements.
The initial step of the crystal growth process is grinding together, for at least thirty minutes, $CaCO_3$ (purity 99.99%, Ba = 1 ppm), RuO_2, (purity 99.9%, Na = 5 ppm) and Pr_6O_{11} (purity 9.9%) in the ratio obtained considering the chemical reaction:

$$(2-\mathrm{x})\,\mathrm{CaCO_3} + \mathrm{yRuO_2} + \frac{\mathrm{x}}{6}\mathrm{Pr_6O_{11}} \longrightarrow \mathrm{Ca_{2-x}Pr_xRu_yO_{4+\delta}} + (2-\mathrm{x})\,\mathrm{CO_2} \qquad (3.1)$$

where x = 0.04 and (y-1)RuO_2 is the excess of Ru added to compensate its volatility during the growth. The resulting powder is pressed with a pressure of 10 MPa into cylindrical pellets with diameter of approximately 2 cm and a height of about 5 mm. The pellets are placed on a Al_2O_3 crucible (Fig. 3.1), piled up on top of a thinner bedding pellet to prevent contamination, and baked in air at a temperature of 1000°C for 12 hours, to allow the solid-state reaction to take place (calcination process). Various tests were carried out to precisely determine the calcination parameters. The chosen ones are those listed in Tab. 3.1. For almost all the samples a preliminary thermal step of 12 hours at 500°C has been done to remove any possible trace of intermediate Praseodymium oxides in the starting Pr_6O_{11} powder, according to [95].

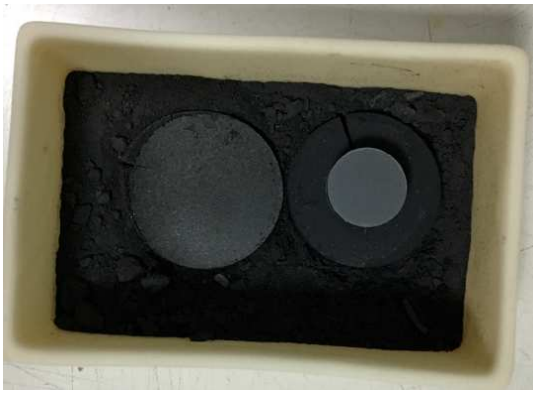

Figure 3.1: $Ca_{1.96}Pr_{0.04}RuO_4$ pellets.

The pellet is then ground into a powder, which is placed inside a narrow cylindrical balloon to form a rod of about 5 mm in diameter and 10-12 cm in length. The rod is inserted into a straw to keep it straight and pressed in water with a pressure of 40 MPa by means of an isostatic press. After removing the straw and cutting the balloon, the rod is placed inside an alumina boat. The boat is closed with an alumina lid and placed in the oven for the sintering process. Tab. 3.2 shows the parameters for sintering. After the sintering process, the feed rod is obtained and it is ready for the growth process; a picture of $Ca_{1.96}Pr_{0.04}RuO_4$ feed rod is reported in Fig. 3.2.
At the first growth a small part of the feed was broken to make a seed rod. During the growth, feed and seed are lowered at different rates and the growth rate is defined by the speed of the seed rod; furthermore seed and feed rotate in opposite direction

				Calcination			
Sample name	Pr	Ru	Ru Excess	T_1 (°C)	time (h)	T_2 (°C)	time (h)
CPRO_01	0.04	1.09	9%	500	12	1000	12
CPRO_03	0.04	1.24	24%	-	-	1000	12
CPRO_05	0.04	1.31	31%	500	12	1000	12
CPRO_06	0.04	1.23	23%	500	12	1000	12
CPRO_07	0.04	1.19	19%	500	12	1000	12
CPRO_09	0.04	1.21	21%	500	12	1000	12.

Table 3.1: Parameters used for calcination with different Ru concentrations. A ramp of 250°C/h was used for the first calcination temperature T_1, while a ramp of 300°C/h was used for the second process temperature T_2.

				Sintering			
Sample name	Pr	Ru	Ru Excess	T_1 (°C)	time (h)	T_2 (°C)	time (h)
CPRO_01	0.04	1.09	9%	1000	12	–	–
CPRO_03	0.04	1.24	24%	1000	12	–	–
CPRO_05	0.04	1.31	31%	500	1	1000	12
CPRO_06	0.04	1.23	23%	500	1	1000	12
CPRO_07	0.04	1.19	19%	500	1	1000	12
CPRO_09	0.04	1.21	21%	500	1	1000	12

Table 3.2: Parameters for the sintering phase as the Ru concentration varies. A ramp of 250°C/h was used for the first calcination temperature T_1, while a ramp of 300°C/h was chosen for the second processes at temperature T_2.

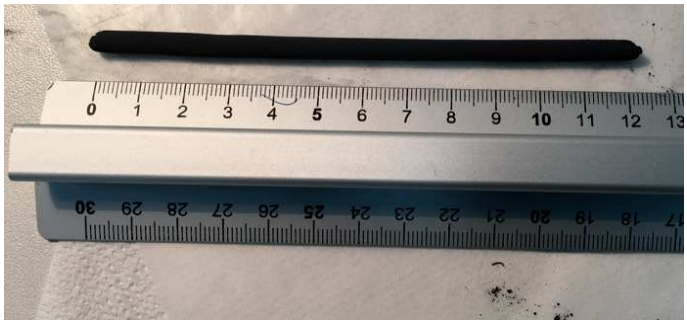

Figure 3.2: Feed road of $Ca_{1.96}Pr_{0.04}RuO_4$ after the sintering process.

to help stabilize the melt (Fig. 3.3). A quartz tube is used to keep the growth in

Figure 3.3: The molten zone.

partial Ar+O_2 pressure to reduce the evaporation of RuO_2 (Fig. 2.4). The first point to be taken into consideration concerns the control of impurities in the material under examination; in particular it was necessary to identify the growth parameters allowing to avoid the inclusion of unwanted phases. All the growth parameters used in the research project presented here are summarized in Tab. 3.3.

Sample	Feed speed (mm/h)	Growth speed (mm/h)	Rotation of feed/seed (rpm)	P (MPa)	Flow (l/min)	Comments
CPRO_01	30	20	33/33	0.9	2	Fused area with solid parts, unstable growth
CPRO_03	30	20	33/33	0.87	2	Stable melt, zone growth ok
CPRO_05	30	20	33/33	0.85	2	Stable melt, zone growth ok
CPRO_06	30	20	33/33	0.85	2	Stable melt, zone growth ok
CPRO_07	30	20	33/33	0.85	2	Fused area with solid parts, unstable growth
CPRO_09	30	20	33/33	0.85	2	Fused area with solid parts, difficulty in melting homogeneously

Table 3.3: Crystal quality with varying growth conditions. The used atmosphere is a mixture of Argon-Oxygen (Ar+O_2) with 90%-10% composition.

Crystal growth was only possible by using an excess of Ru equal to or greater than 23% in the starting feed rod in order to grow $Ca_{(2-x)}Pr_xRuO_4$ crystals with x = 0.04.

For lower percentages, growth failed due to molten zone instability.

3.1.2 Results and discussion

Morphological and compositional study

Observation by polarized optical microscope of samples from the batches CPRO_03, CPRO_06, grown with an excess of Ru of 23 and 24%, respectively showed two types of morphology. As reported in Fig. 3.4, some crystals display a homogeneous single phase (panel (a)) while others show a dark main matrix with bright dots and lamellar inclusions (panel (b)).

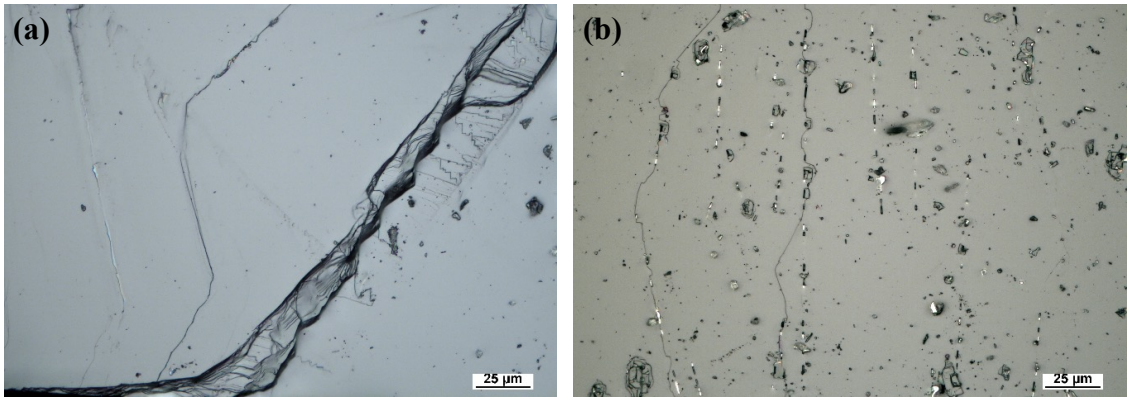

Figure 3.4: Optical image of (a) pure $Ca_{1.96}Pr_{0.04}RuO_4$ single crystal and (b) $Ca_{1.96}Pr_{0.04}RuO_4$ crystal with Ru inclusions (bright lamellae).

The morphological and compositional investigations with SEM/EDX performed on various cleaved samples from batches CPRO_03 and CPRO_06 confirmed the presence of two types of crystals. In Fig. 3.5 SEM images and EDX compositional analyses performed on crystals from batch CPRO_06 are reported.
Fig. 3.5(a) SEM shows image of a homogeneous single phase crystal. Quantitative compositional microanalyses by EDX, performed on different spots, confirmed a composition given by $Ca_{1.96\pm0.01}Pr_{0.04\pm0.01}Ru_{1.03\pm0.01}O_{4.50\pm0.06}$. Fig. 3.5(c) reports an example of EDX spectrum and elemental composition acquired on the sample in Fig. 3.5(a). In addition, crystals from batch CPRO_06 with different morphology are shown in Fig. 3.5(b), where it is evident the presence of a main crystal with lamellar arranged inclusions. The EDX analyses on those crystals showed a composition of $Ca_{1.96\pm0.01}Pr_{0.04\pm0.01}Ru_{1.03\pm0.01}O_{4.50\pm0.06}$ for the main matrix and the presence of Ru inclusion in the lamellar domain.
Examination by polarized optical microscope of samples grown using 30% excess of Ru (batch CPRO_05) reveals the presence of a lamellar pattern typical of eutectic solidification [96, 97] on the whole sample surface. The lamellae are aligned along a

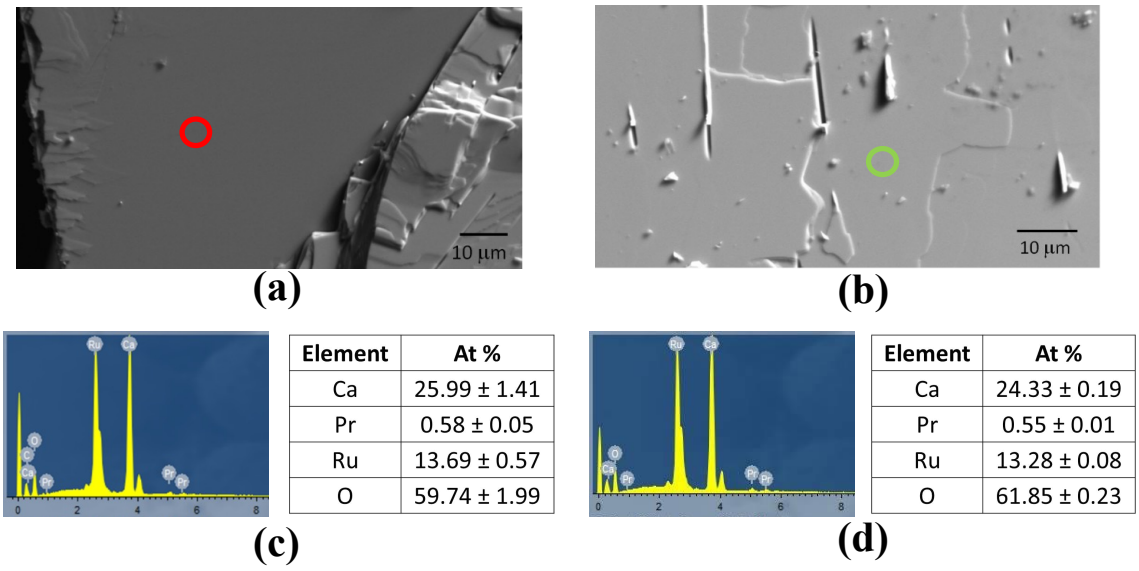

Element	At %
Ca	25.99 ± 1.41
Pr	0.58 ± 0.05
Ru	13.69 ± 0.57
O	59.74 ± 1.99

Element	At %
Ca	24.33 ± 0.19
Pr	0.55 ± 0.01
Ru	13.28 ± 0.08
O	61.85 ± 0.23

Figure 3.5: SEM images of (a) $Ca_{1.96}Pr_{0.04}RuO_4$ single crystal; (b) $Ca_{1.96}Pr_{0.04}RuO_4$ single crystal with Ru inclusions; (c) and (d) EDX spectrum and quantitative analysis of the spots in panel (a) and (b).

certain direction, as shown in Fig. 3.6. Moreover, in this case the lamella cover 6.71% in areas of approximately 1.12 x104 μm^2 with a separation between adjacent lines of about 10 μm.

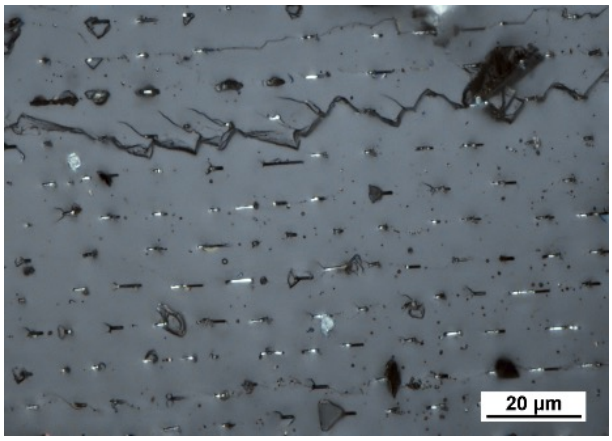

Figure 3.6: Optical image of a $Ca_{1.96}Pr_{0.04}RuO_4$ single crystal with a large excess of Ru.

Investigations by SEM on several crystals from the same batch (i.e., CPRO_05) always show the presence of bright dots and lamellae regularly dispersed in a main dark matrix, thus confirming the pattern typical of eutectic solidification. The EDS elemental maps (Fig. 3.7) acquired on those samples reveal that the bright inclusions are domains rich in Ru, while no accumulations of Pr were found. Quantitative EDX analysis acquired in the regions without Ru inclusions show a composition equal to $Ca_{1.96\pm0.01}Pr_{0.04\pm0.01}Ru_{1.07\pm0.01}O_{4.97\pm0.06}$. The latter is comparable to what is found in crystals grown with a lower excess of Ruthenium. This result suggests that the phase

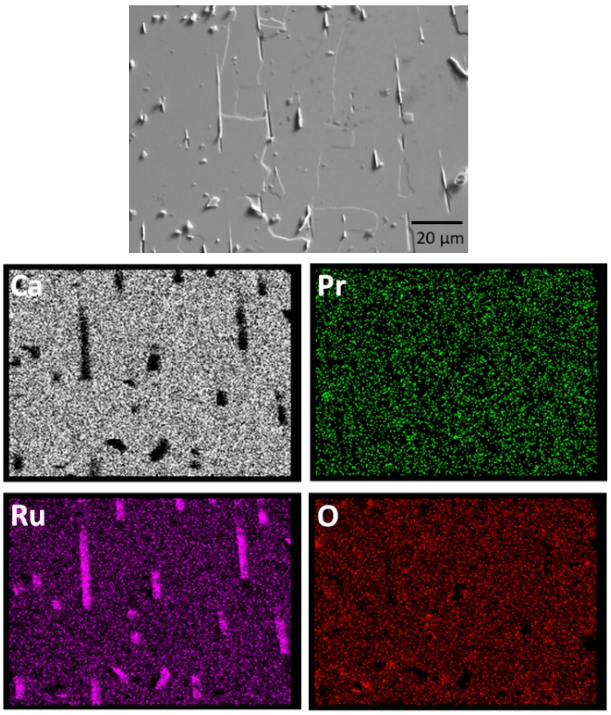

Figure 3.7: EDX compositional map of a $Ca_{1.96}Pr_{0.04}RuO_4$ crystal with Ru lamellae.

of the matrix in the eutectic-like sample is not different from the pure $Ca_{1.96}Pr_{0.04}RuO_4$ crystal. Furthermore, whatever excess of Ruthenium has been used, a thorough comparison of the morphologies of crystals with Ru inclusions shows that the lamellae seem always to line up along a certain direction

Structural study

The results of XRD analysis on the eutectic-like samples and the pure samples from the batch CPRO_06 are reported in Fig. 3.8(a); for comparison, the XRD pattern of an undoped Ca_2RuO_4 single crystal is also plotted.
The X-ray diffractograms show peaks ascribable to the expected (00l) Bragg reflections coming from the Ca_2RuO_4 phase; no extra peaks related to other phases are identified. Actually, in the spectrum of the samples exhibiting the eutectic-like structure, a signal due to metallic Ru was also found (Fig. 3.8(b)). Only the (100) reflection appeared, thus supporting the picture of a preferential alignment of the Ru precipitates in relation to the orientation of the $Ca_{1.96}Pr_{0.04}RuO_4$ matrix. Regarding the main peaks, it should be noted that only the (00l) reflections of the $Ca_{1.96}Pr_{0.04}RuO_4$ phase are detected, indicating that the crystals tend to cleave along the a-b plane. Shift towards lower 2θ values were observed in the Pr doped Ca_2RuO_4 crystals with respect to the undoped ones. The peak shift is greater in crystals without the Ru inclusions compared to the eutectic-like samples. The c-axis parameters, evaluated from the spectra in Fig. 3.8(a), were 12.216 Å and 12.209 Å for pure Pr-doped and the eutectic-like crystals, respec-

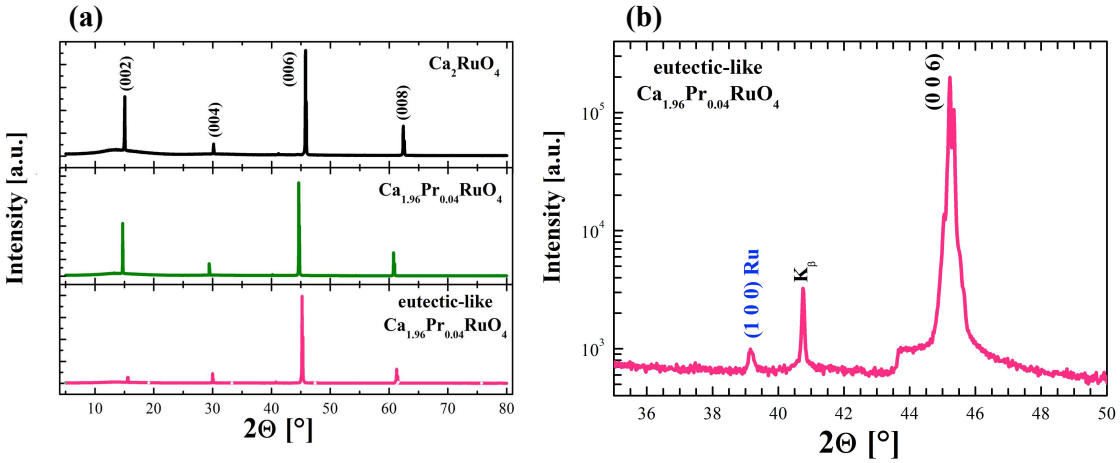

Figure 3.8: θ-2θ scan of pure Ca_2RuO_4, 4% Pr-doped Ca_2RuO_4 and eutectic like $Ca_{1.96}Pr_{0.04}RuO_4$ crystals. (b) Zoom of XRD spectrum of an eutectic-like $Ca_{1.96}Pr_{0.04}RuO_4$ crystal showing Ru peak.

tively. It is worth mentioning that the value $c = 11.838$ Å is found for the undoped Ca_2RuO_4 crystals. Comparing the measured c-axis parameters, the following trend is inferred $c_{\text{Pr doped crystals}} > c_{\text{eutectic like crystal}} > c_{Ca_2RuO_4}$. Then, the Ru inclusions seem to induce a reentrant behavior for the c-axis parameter. All the measured parameters are close to the values reported in the literature for similar systems; in particular, a value of c approximately equal to 12.2 Å was reported for $Ca_{1.96}Pr_{0.04}RuO_4$ samples that at room temperature were in their metallic phase and exhibited long c-axis and orthorhombic structures with *Pbca* space group [46].

To further analyze the emergence of a preferential orientation for Ru metal inclusions, pole figures have been acquired for eutectic like samples from different batches; i.e. CPRO_03, CPRO_05 and CPRO_06. In Fig. 3.9 the pole figure obtained from a cleaved CPRO_06 crystal is shown. To perform the pole figure measurement, the sample was tilted in Ψ and rotated in Φ. The data in Fig. 3.9 are collected by using the (100) reflection of Ru obtained at a fixed value $2\theta = 38.39°$. The appearance of only one pole for (100) of Ru phase definitely confirms, in the case of Pr-doped Ca_2RuO_4 crystals, the solidification of Ru inclusions with preferential orientation. As shown in Ref. [94], the use of the electron backscatter diffraction (EBSD) technique provides another useful way of investigating the microstructure of multiphase ruthenates single crystals, yielding information concerning the crystallography. Fig. 3.10 shows SEM image and EBSD phase map of a polished Pr-doped Ca_2RuO_4 crystal with lamellae of Ru confirming the crystallinity of both phases. EBSD measurements have been performed on different eutectic like Pr-doped Ca_2RuO_4 crystals. In all the inspected samples the lamellae of ruthenium are aligned with each other. An example of inverse pole figure (IPF) maps showing Ru inclusions with the same orientation is reported in Fig. 3.11. They are acquired along three different directions, i.e., parallel to the sample normal (ND) and to the two in-plane orthogonal directions, rolling (RD) and

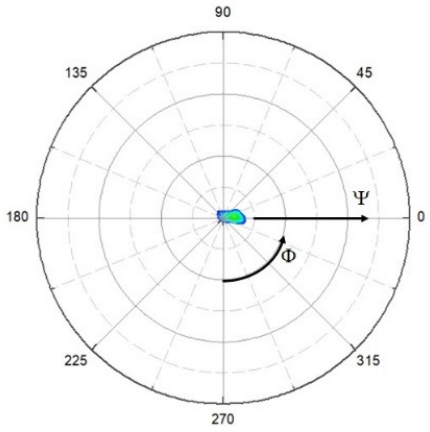

Figure 3.9: X-ray pole figures of the sample CPRO23. The fixed 2θ angle was 38.39° corresponding to Ru (100) planes.

transverse (TD), and yield the coherent crystallographic orientation of Ru lamellae as determined by EBSD (top left Fig. 3.11(c)). The color code is given in the stereographic triangle below (Fig. 3.11(d)). To study the crystallographic orientation of the

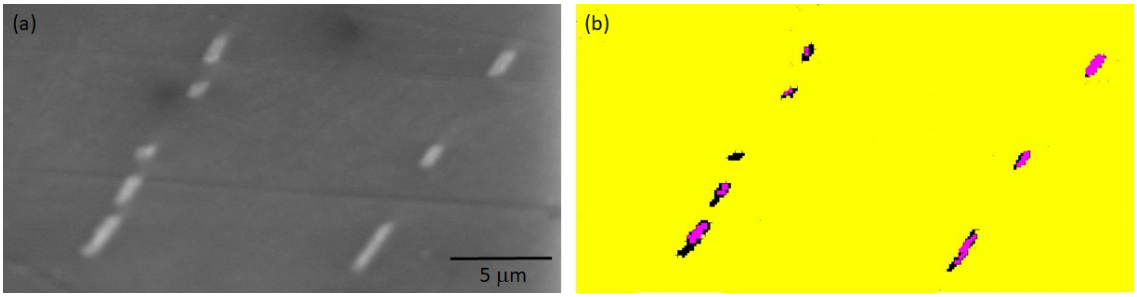

Figure 3.10: Polished Pr-doped Ca_2RuO_4 crystal with lamellae of Ru: (a) SEM image and (b) EBSD phase map.

main $Ca_{1.96}Pr_{0.04}RuO_4$ phase, the room temperature crystallographic cell of Ca_2RuO_4 doped with 4% of Pr reported by Riccó *et al.* [46] was entered in the software database for the phase identification. The results of EBSD reported in Fig. 3.12(a) show that the *c*-axis of the $Ca_{1.96}Pr_{0.04}RuO_4$ phase, in agreement with XRD investigation, is always perpendicular to the sample surface, hence *a* and *b*-axes are in-plane. However, a thorough inspection of in-plane EBSD orientation maps in Fig. 3.12(b-c) show the presence of grains. In order to visualize the grains and to determine the misorientation between two neighboring domains, a misorientation grain map has been extracted from the results reported in Fig. 3.12. It shows that in the left part of the sample there is a predominant grain and no micro-grains, while a huge numbers of micro-grains appear in the region limited by the lamellae of ruthenium. The misorientation between adjacent domains is quantified in Fig. 3.13(b). A particular misorientation is prominent as shown by the profiles taken along the two lines indicated in Fig. 3.13(a). Both line profiles show a 90° misorientation indicating the formation of twin domains.

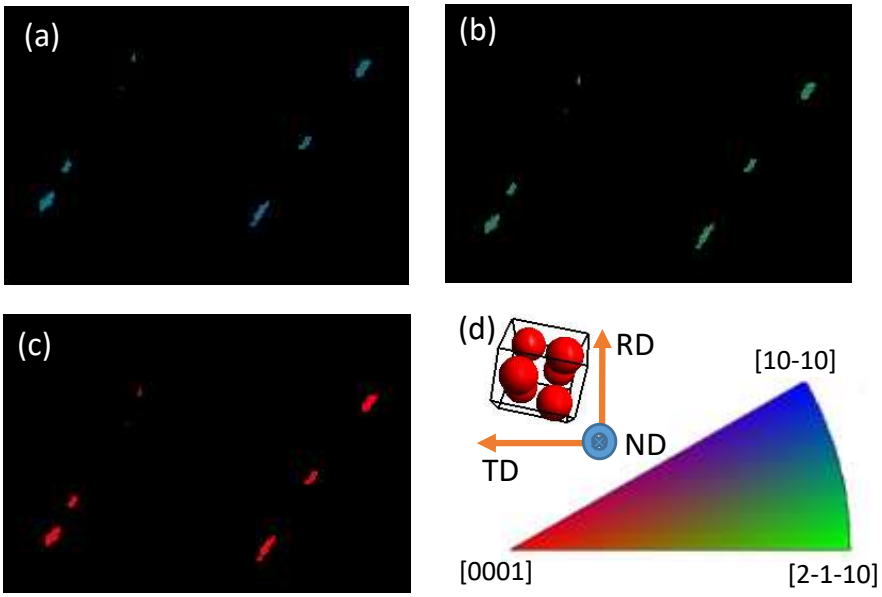

Figure 3.11: IPF maps in the three spatial directions (a) normal - ND, (b) rolling – RD and (c) transverse -TD, of Ru inclusions of the sample in Fig. 3.10, (d) crystallographic orientation of Ru cells as determined by EBSD. The color code is given in the stereographic triangle.

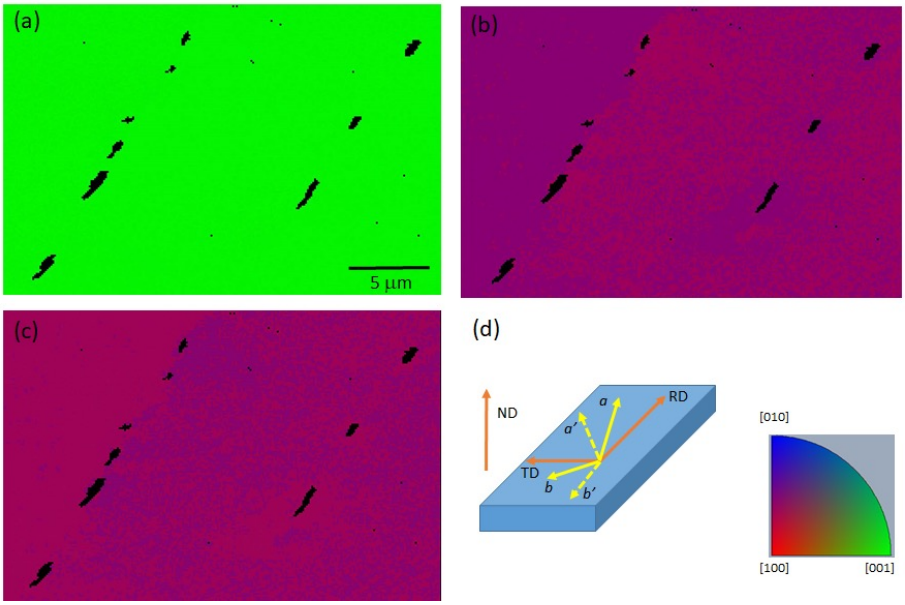

Figure 3.12: IPF maps of $Ca_{1.96}Pr_{0.04}RuO_4$ phase in the three spatial directions (a) normal, (b) rolling and (c) transverse, acquired for the sample in Fig. 3.10. The scale bar is the same for all three figures;(d) the color code for the maps is given in the stereographic triangle. The yellow arrows indicate the orientation of the $Ca_{1.96}Pr_{0.04}RuO_4$ phase.

Magnetic and transport study

To examine the influence of Pr doping and Ru inclusions on magnetic and electrical properties of Ca_2RuO_4 crystals, magnetization and resistivity measurements as func-

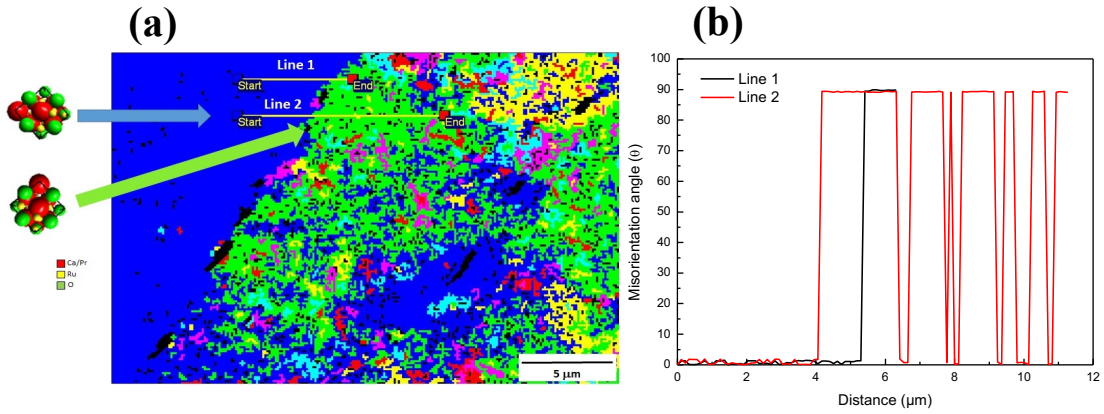

Figure 3.13: (a) Grain misorientation map of the Pr-doped Ca_2RuO_4 phase in eutectic-like crystal with the corresponding orientation of the unit cell for some domains (colors of the arrows correspond to the colors of the domains). (b) Angular misorientation profiles with respect to the left part of the crystal along lines 1 and 2 in (a).

tions of temperature have been performed.

Measurements of the magnetic moment m as a function of the temperature T have been performed on pure Pr-doped crystal by cooling the sample down to 5 K in the absence of field. Then, the field has been set equal to 1 T and 2 T, applied parallel to the c-axis, and data have been acquired while increasing the temperature up to 300 K (Zero Field Cooling). After that, the sample has been cooled down again with the field still applied (Field Cooling). Care has been taken to the reduction of the trapped field in the magnet before starting each measurement. In Fig. 3.14, a cusp-like behavior is visible for both the applied magnetic fields indicating a dominant antiferromagnetic ordering. It is worth pointing out that the temperature peak, characterizing the Neél temperature T_N of the sample, can be individuated at $T_N = (122 \pm 2)$ K, that is about 10 K higher than the T_N of the undoped compound [24, 98]. For $T < 60$ K, the hysteresis between ZFC and FC curves, together with the increase of the magnetic signal while decreasing the temperature, indicates that the magnetic structure of the sample has a ferromagnetic component. On the other hand, for $T > T_N$ the absence of hysteretic behavior between ZFC and FC curves, together with the decrease of the magnetic moment for increasing temperature, signals a paramagnetic ordering of the sample.

To evaluate the electrical response, the temperature dependence of the resistance measured along the c-axis for Pr-doped Ca_2RuO_4 crystals, both for the single phase and with different percentage of Ru inclusions, have been acquired (Fig. 3.15). The R-T curve of the 4% Pr-doped Ca_2RuO_4 reveals a metal-insulator transition at 270 K, while the crystals with Ru inclusions do not show a sharp transition from the metallic to the insulating state. In addition, performing measurements on crystals with different percentage of Ru inclusions, a re-entrant behavior is observed, i.e. crystals with higher Ru content show a metallic behavior in a smaller temperature range if com-

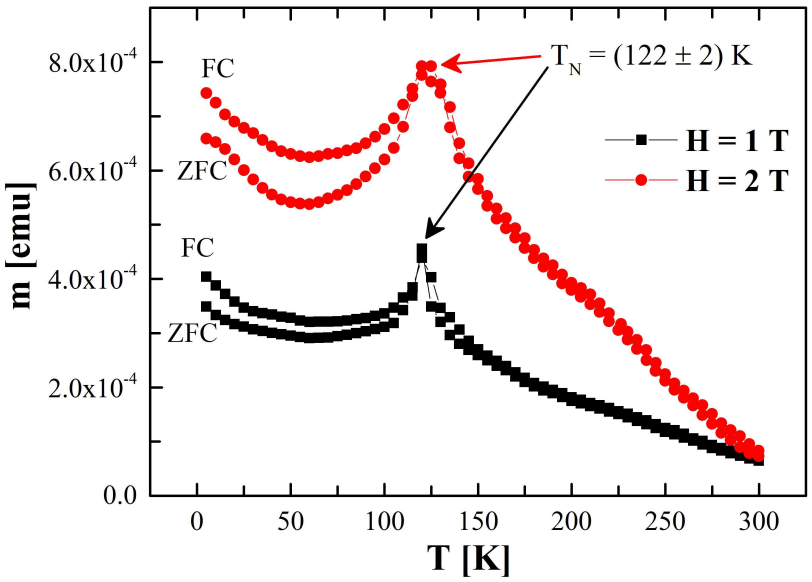

Figure 3.14: ZFC and FC curves of $m(T)$ at H = 1 T (black closed squares) and H = 2 T (red closed circles) for a Pr-doped single crystal.

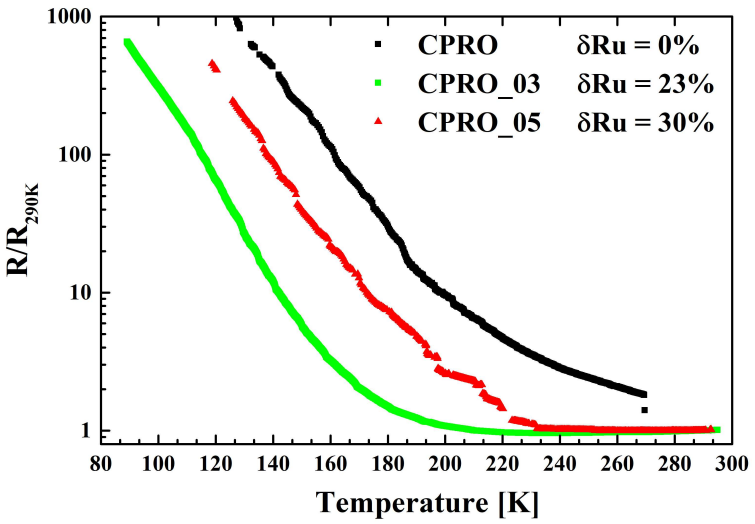

Figure 3.15: Normalized resistance as a function of temperature for 4% Pr-doped Ca_2RuO_4 crystals with and without Ru inclusions. For each crystal the content of Ru is reported in the figure.

pared with crystals with lower Ru content. Furthermore, the R(T) curve of crystals with highest Ru excess falls between the curve of Pr-doped Ca_2RuO_4 and the one with lower Ru inclusions. This finding may be related to a modification of the crystallographic cell parameters and the presence of twin domains observed through XRD and EBSD measurements, this supporting a substantial influence of lattice distortions on the transport properties of doped Ca_2RuO_4.

Finally, Fig. 3.16 reports a selection of $V-I$ characteristics as a function of T obtained by current biasing a eutectic like $Ca_{1.96}Pr_{0.04}RuO_4$ single crystal along the c-axis. It is

possible to observe that the sample shows an insulating behavior in the low I regime and a negative differential resistance for higher I values. The change in the conduction results in a maximum in the $V - I$ characteristics, similarly to what has been reported for Ca_2RuO_4 crystals [29, 39]. Our observations clearly show that a combination of EBSD analysis together with transport measurements using the same sample portions would be crucial to shed light on the microscopic mechanism underlying the transport properties of this complex system. This will be especially important in the design of twin-boundary devices exhibiting in a stable and reproducible way insulator-to-metal transitions induced by low voltage/current.

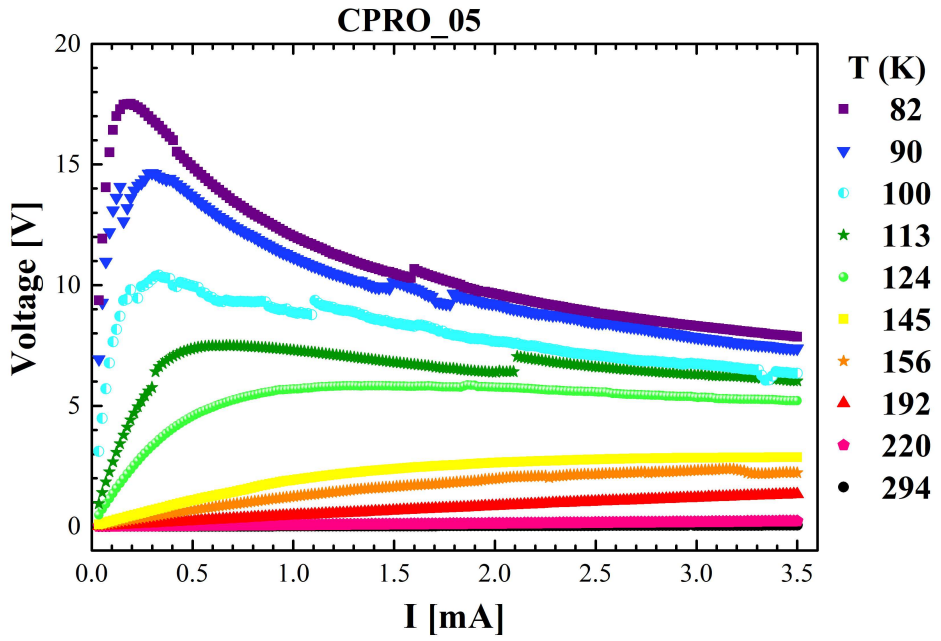

Figure 3.16: $V - I$ characteristics as a function of T acquired on eutectic-like $Ca_{1.96}Pr_{0.04}RuO_4$ single crystal.

3.2 $Ca_2Ru_{1-x}Mn_xO_4$

3.2.1 Crystal growth of $Ca_2Ru_{1-x}Mn_xO_4$

Single crystals of $Ca_2Ru_{1-x}Mn_xO_4$ with x =0, 0.03, 0.05, 0.10, 0.20 have been grown using the FZ technique. For the preparation of the samples the same procedure as the one presented above was used, but it was necessary to fine-tune the various parameters of the different processes. Optimized parameters for calcination and sintering processes of $Ca_2Ru_{1-x}Mn_xO_4$ are shown in Tab. 3.4, Tab. 3.5 and Tab. 3.6.
After several attempts of crystal growth, where growth parameters such as the speeds of feed rod and seed crystal and the counter-rotation speed were varied, large single

			First calcination step	
x (Mn content)	Ru	Ru Excess	T_1 (°C)	time (h)
0	1.15	0.15		
0.2	0.95	0.15	980	24
0.1	1.035	0.135	980	24
0.03	1.105	0.135	980	24
0.05	1.085	0.135	980	24

Table 3.4: Parameters used for first calcination step for different Mn doping. A ramp of 300°C/h was used for the calcination temperature.

			Second calcination step	
x (Mn content)	Ru	Ru Excess	T_1 (°C)	time (h)
0	1.15	0.15	–	–
0.2	0.95	0.15	980	24
0.1	1.035	0.135	980	24
0.03	1.105	0.135	980	24
0.05	1.085	0.135	980	24

Table 3.5: Parameters used for second calcination step for different Mn doping. A ramp of 300°C/h was used for the calcination temperature.

			Sintering	
x (Mn content)	Ru	Ru Excess	T_1 (°C)	time (h)
0	1.15	0.15		
0.2	0.95	0.15	1050	12
0.1	1.035	0.135	1050	12
0.03	1.105	0.135	1050	12
0.05	1.085	0.135	1050	12

Table 3.6: Parameters used for sintering the rods with different Mn doping. A ramp of 300°C/h was used to reach the sintering temperature.

crystals with high crystalline quality have been obtained. The entire set of growth parameters are summarized in Tab. 3.7.

Sample name	x	Feed speed (mm/h)	Growth speed (mm/h)	P (MPa)	Flow (l/min)	Comments
CMRO_03	0.2	30	20	0.85	2.5	Stable
CMRO_06	0.1	25	15	0.85	2.5	Stable
CMRO_09	0.03	25	15	0.9	2.8	Stable
CMRO_11	0.05	30	15	0.85	1.5	Stable
Ca_7	0	30	15	0.85	2.5	Stable

Table 3.7: Summary of crystal growth parameters for different Mn doping. The used atmosphere is a mixture of Argon/Oxygen with 90% Ar and 10% O_2. The rotation of feed and seed was 33 rpm for both.

3.2.2 Compositional and structural study

The composition of the crystals with different Mn content has been inspected by EDX quantitative investigations. To check the final Mn content, several sample pieces have been selected for each nominal Mn doping value. The composition of each measured crystal has been derived by averaging all EDX data acquired over different areas and normalizing them such that Ca=2, while the measured Mn content (x) has been determined using the following equation:

$$(1-x) : x = \%Ru : \%Mn \qquad \rightarrow \qquad x = \frac{\%Mn}{\%Mn + \%Ru} \,. \tag{3.2}$$

An example of SEM image and EDX spectrum of a Mn doped Ca_2RuO_4 is reported

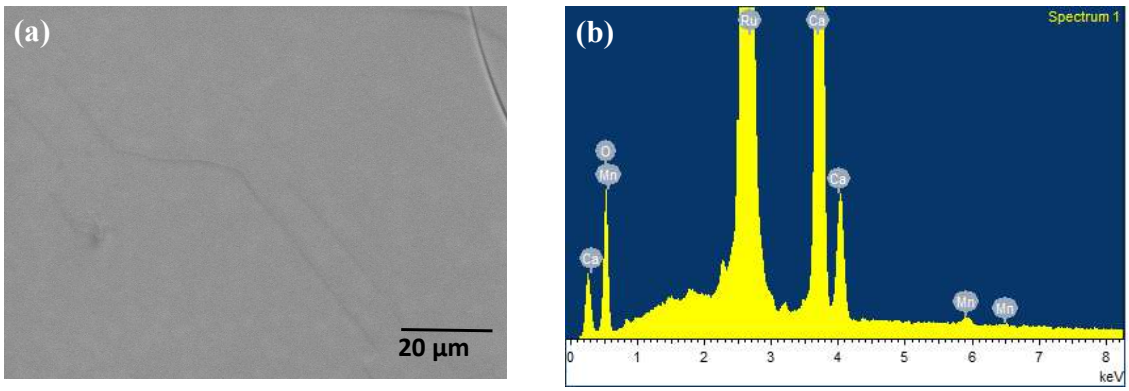

Figure 3.17: (a) SEM Image and (b) EDX spectrum of a Mn-doped Ca_2RuO_4 acquired on a sample doped with 5% of Mn.

in Fig. 3.17, while the compositional results for all the synthesized crystals are summarized in Tab. 3.8.
Furthermore, to test the uniformity of Mn doping on the sample surface, EDX compositional maps have been acquired. The results of EDX maps acquired on a 3% Mn

Sample name	Ca (at%)	Ru (at%)	Mn (at%)	O (at%)	measured x content	Crystal composition
CMRO_09	28.84	15.11	0.49	52.57	0.031±0.004	$Ca_2Ru_{1.05}Mn_{0.03}O_{3.65}$
CMRO_11	26.97	13.06	0.78	59.18	0.056±0.002	$Ca_2Ru_{0.97}Mn_{0.05}O_{4.39}$
CMRO_06	27.38	13.53	1.42	55.15	0.095±0.004	$Ca_2Ru_{1.00}Mn_{0.1}O_{4.03}$
CMRO_03	28.30	12.97	2.62	56.12	0.168±0.003	$Ca_2Ru_{0.93}Mn_{0.17}O_{3.97}$

Table 3.8: Summary of EDX results acquired on samples with different Mn content.

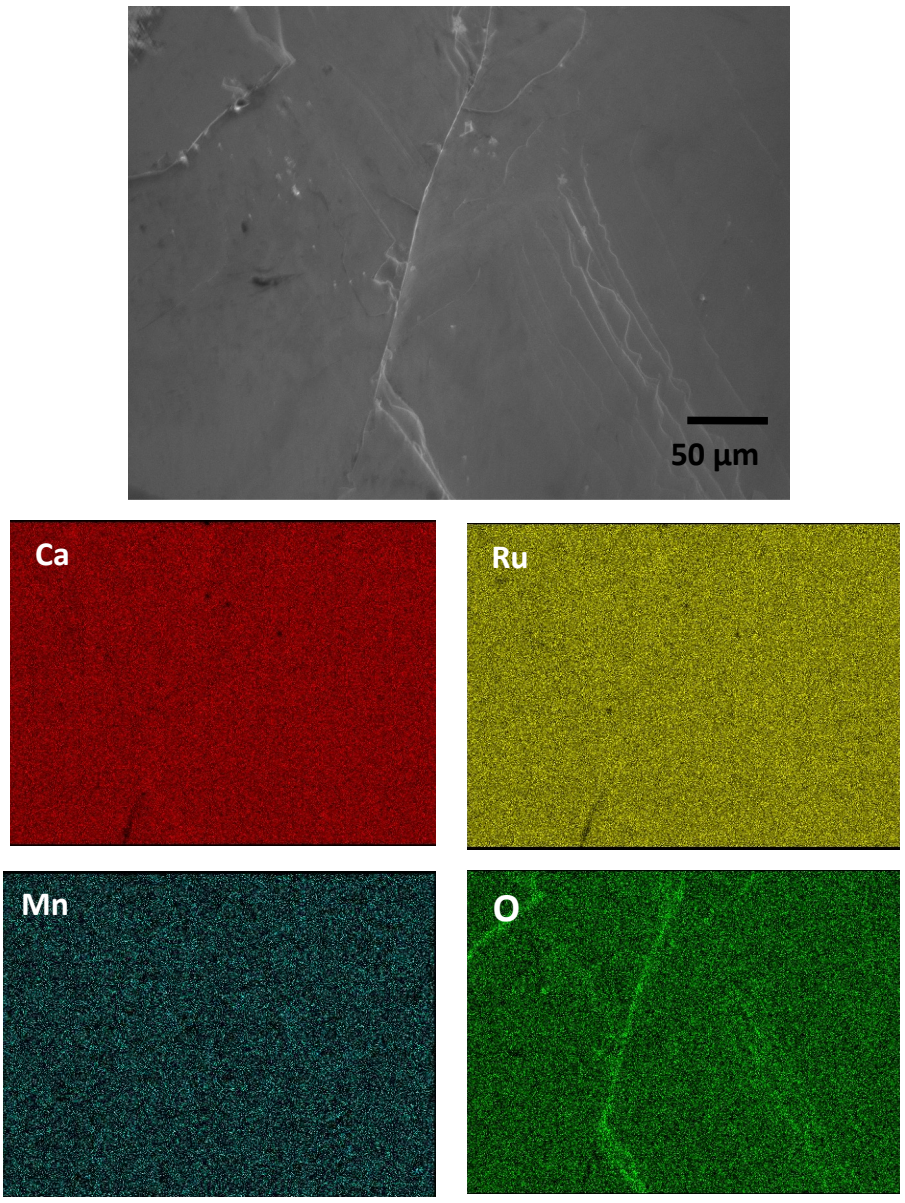

Figure 3.18: SEM image and EDX compositional map of a 3% Mn-doped crystal. A uniform distribution of the elements Ca, Ru, Mn and O has been observed.

doped crystal showing a uniform composition are reported in Fig. 3.18. The same analysis performed on crystals with different Mn content up to 20% confirmed a uni-

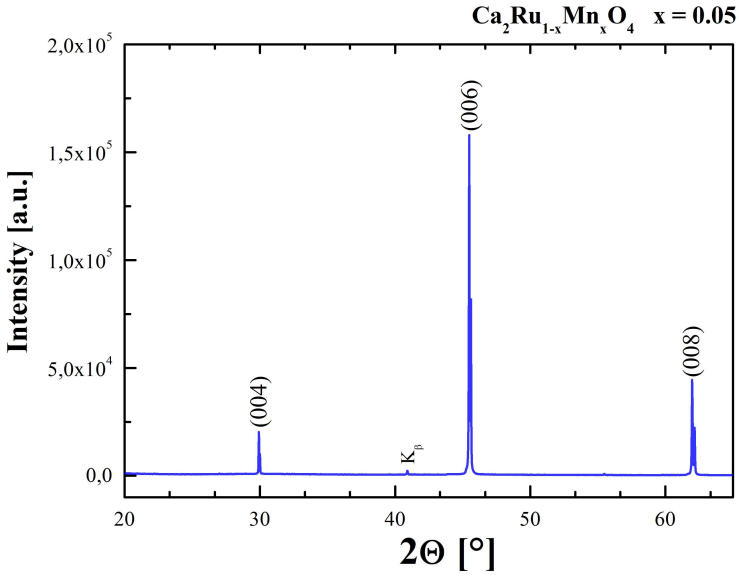

Figure 3.19: X-ray diffraction pattern of the cleaved surface of a $Ca_2Ru_{1-x}Mn_xO_4$ single crystal for $x = 5\%$. All the peaks correspond to reflections coming from $Ca_2Ru_{1-x}Mn_xO_4$.

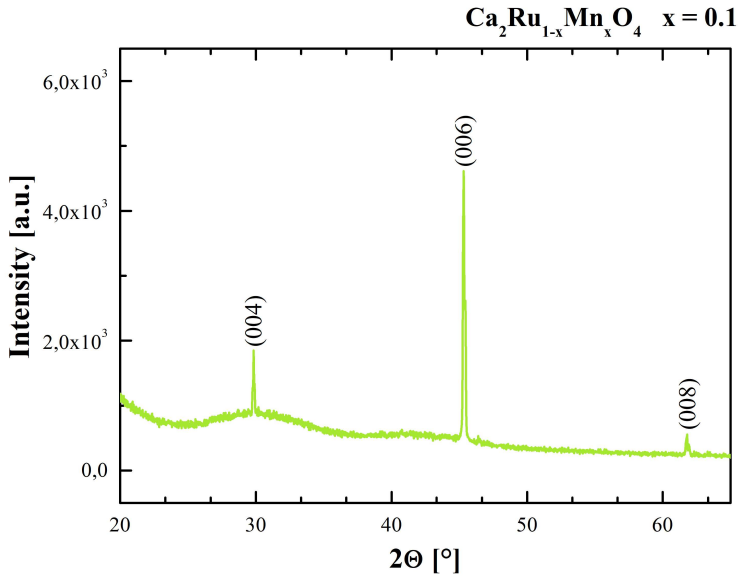

Figure 3.20: X-ray diffraction pattern of the cleaved surface of a $Ca_2Ru_{1-x}Mn_xO_4$ single crystal for $x = 10\%$. All the peaks correspond to reflections coming from $Ca_2Ru_{1-x}Mn_xO_4$.

form distribution of the elements Ca, Ru, Mn and O in all the analyzed samples.
X-ray diffraction (XRD) patterns were obtained by an automatic D2-PHASER 2nd-generation diffractometer. The instrument works in Bragg-Brentano geometry employing Cu-K_α radiation ($\lambda = 1.54$ Å), (see Chapter 2 for more details). The data were collected by step-scanning in the angle range $20° \leqslant 2\theta \leqslant 65°$ at a step size of 0.02° and counting time of 2 s for each step. XRD patterns, for $x = 5\%$ and $x = 10\%$ are shown in Fig. 3.19 and 3.20, respectively. They show that all peaks can be indexed as belonging to the expected $Ca_2Ru_{1-x}Mn_xO_4$ phase.

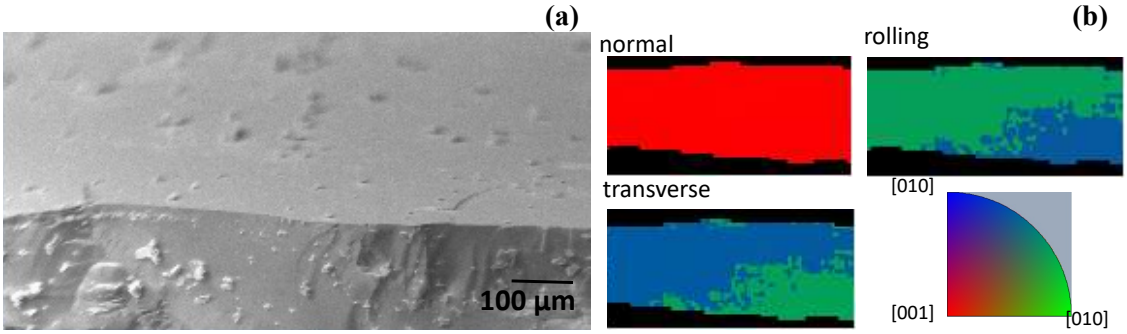

Figure 3.21: (a) SEM image and (b) IPF maps of a $Ca_2Ru_{0.95}Mn_{0.05}O_4$ crystal in all three directions (normal, rolling and transverse). The color code for the maps is given in the stereographic triangle.

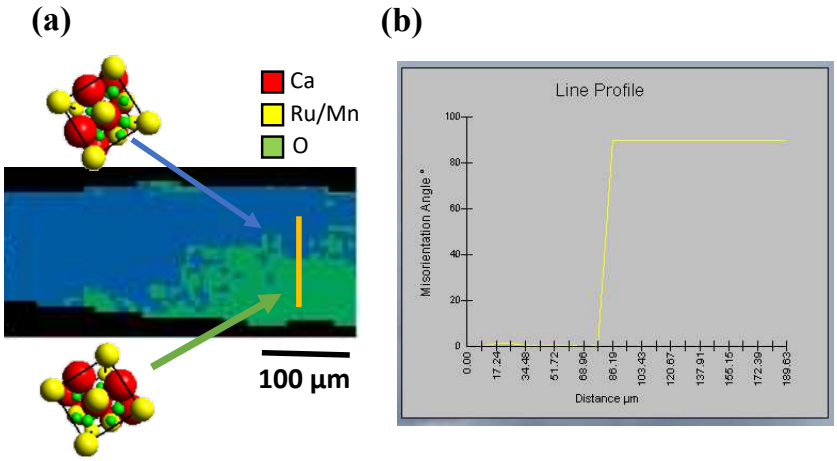

Figure 3.22: (a) Transverse direction orientation map of the sample in Fig. 3.21 with the corresponding orientations of the unit cell for the two domains (colors of the arrows correspond to the colors of the domains); (b) angle misorientation profile along the yellow line crossing the two domains in (a).

To investigate the microstructure and in particular the in plane orientation of the Mn-doped crystals, EBSD maps have been acquired. The results of EBSD reported in Fig. 3.21 show that the c-axis of the $Ca_2Ru_{0.95}Mn_{0.05}O_4$ phase, in agreement with XRD investigation, is always perpendicular to the sample surface, hence a and b-axes are in-plane. Moreover, as it is better shown below, the a- and b- axis are disposed at 45-degrees with respect to the sample edge.
However, a thorough inspection of the EBSD orientation maps (rolling and transverse direction) shows the presence of in-plane misorientation in the analyzed sample. In order to estimate the misorientation between the two domains, a misorientation line profile has been extracted from the results reported in Fig. 3.21. The line profile shows a 90° misorientation (Fig. 3.22(b)) highlighting the probable formation of twin domains also in Mn doped crystals.

3.3 Large scale facilities experiments

3.3.1 Antiferromagnetic transition in Mn doped Ca_2RuO_4 probed by resonant X-Ray diffraction

This section is devoted to presentation of the resonant X-Ray diffraction experiments, and the structural and magnetic measurements performed in collaboration with the group of Dr. Alessandro Bombardi at Diamond Light Source on the single crystals of Mn doped Ca_2RuO_4 grown in Salerno at the Musa Lab of CNR SPIN.

Resonant elastic X-ray scattering measurements

By means of resonant X-Ray diffraction, the evolution of the structural, magnetic, and orbital degrees of freedom for Mn-doped Ca_2RuO_4 have been tracked to investigate the mechanisms which drive the antiferromagnetic transition. While this analysis focuses on a specific case of substitution, it is shown that any perturbation that can impact in a similar way on the crystal structure, by reconstructing the induced spin-orbital exchange, is able to drive the antiferromagnetic reorganization [58].
Ca_2RuO_4 (CRO) exhibits two possible magnetic structures, close in energy, and related only by a local breaking of time-reversal symmetry on a nonsymmorphic symmetry element - a screw-axis or glide-plane operation [19, 24, 25]. The transition between these phases can be generally obtained by orbital reconstruction through substitutional doping. Orbital degrees of freedom are known to set out the character of the magnetic exchange in complex oxides. Here, the modified magnetic exchange and the structural distortions driven by the substitution cooperate to yield a variation of the orbital occupancy that in turn controls the changeover of the AFM patterns.
In Fig. 3.23(c) structural data from the literature on this material are reported, including data on pure CRO and $Ca_2Ru_{1-x}Mn_xO_4$ crystals grown at Musa Lab, covering a variety of different doping scenarios and consequences of pressure or oxygen changes in the stoichiometry. It possible to observe a general trend concerning the interplay of structural and magnetic properties: the A-centered phase is only observed under the most extreme negative distortions of both the cell and the octahedra, i.e. when the RuO_6 octahedra are more flat and the cell is most elongated along the *b*-direction, a situation that only occurs close to the pristine compound. The magnetic reconstruction can be understood by considering that the modification of the orbital occupation at the Ru site alters the character of the Ru-Ru magnetic exchange from antiferromagnetic to ferromagnetic, as schematically described in Fig. 3.23(d), with the magnetic exchange path illustrated in Fig. 3.23(a). The similarity in the octahedral distortions of CRO under different scenarios, as for example changing the ionic radius of the cation (Ca> La or Sr), the oxidation state or applying pressure, allows to harmonize and ac-

count for all the observations of the phase diagram in Fig. 3.23(c). As anticipated, the work presented here was focused along this line on doping the ruthenium site with manganese, a magnetic transition metal with a similar radius but one less electron in valence.

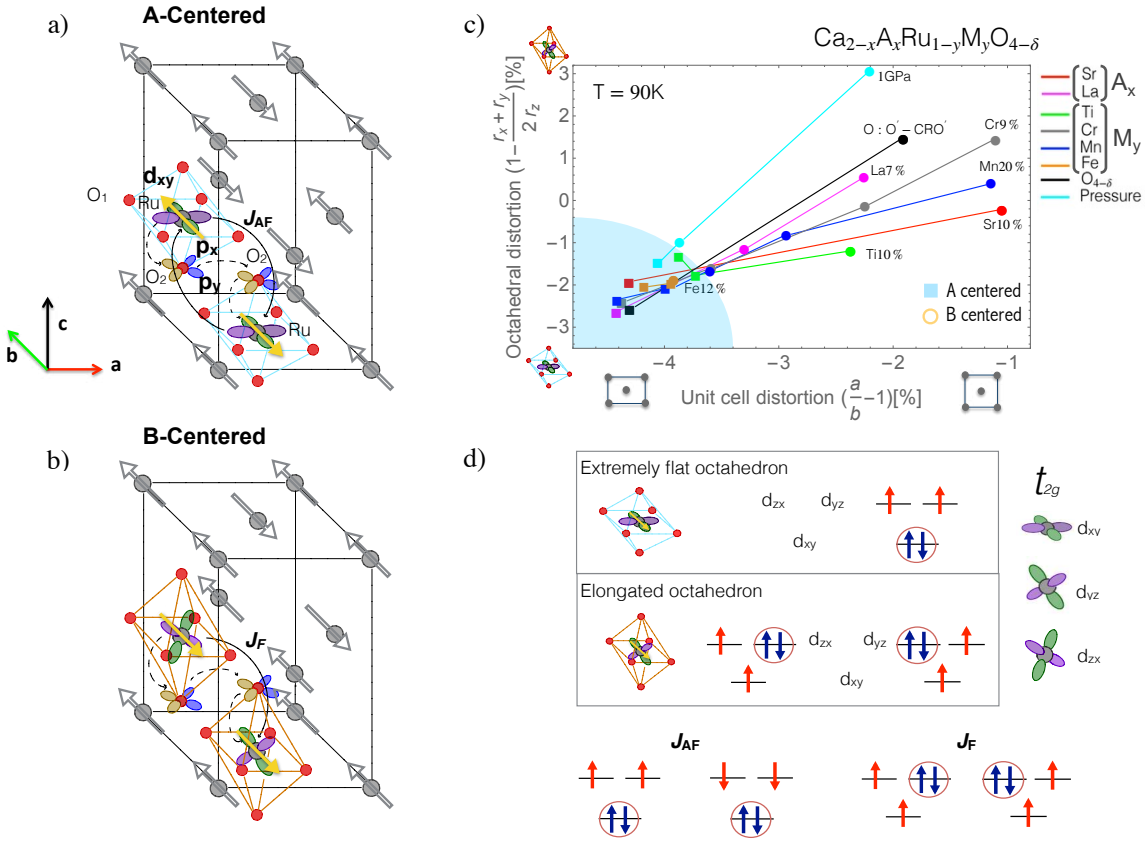

Figure 3.23: Schematics of the magnetic structures reported in pure and Mn-substituted CRO. The A-centered (a) and B-centered phase (b) differ in the stacking sequence of adjacent layers, with moments of the intermediate ruthenium layers pointing in opposite direction. For simplicity, the small canting of magnetic moments along the c-axis and tilting and rotation of the RuO_6 octahedra are not displayed. (c) Variation in octahedral distortion to unit cell distortion across different structure alteration regimes, for structure data of CRO from the literature related to several doping, pressure and changes in oxygen stoichiometry. The octahedral distortion is calculated from $RuO_1(r_x, r_y)$ and $RuO_2(r_z)$ bond lengths. All structures showed are at 90 K. (d) Left side: dominant AFM exchange between Ru spin moments, in doubly occupied d_{xy} orbital configuration favored by the compressive tetragonal distortion of the pure CRO. Right side: dominant FM exchange between Ru spins in the alternated doubly occupied d_{zx}/d_{yz} orbital configuration induced by substitution.

Experimental Results

Single crystals of $Ca_2Ru_{1-x}Mn_xO_4$ with x = $0, 0.03, 0.05, 0.10, 0.20$ were grown using a floating zone furnace and characterized prior to synchrotron beamtime experiments, as

reported in Section 3.2.2. The challenge of growing large crystals of $Ca_2Ru_{1-x}Mn_xO_4$ is related to the abrupt structural transition occurring close to 350 K; however, it was found that cooling slowly through the transition resulted in large plate-shaped samples with the (00l) direction perpendicular to the large face and dimensions of about 1000x1000x100 μm^3. Structural characterization was performed using a molybdenum source X-Ray diffractometer (Oxford Diffraction) with a cryogen (Oxford Instruments) for temperature control between 90 and 500 K. Magnetization measurements were performed using the DC measurement option on a Quantum Design MPMS3. The samples were aligned prior to measurement with X-Ray diffraction and mounted on a quartz rod with GE varnish such that the c-axis was perpendicular to the field and either the $a-$ or $b-$ axis were parallel to the field. Samples were measured in on-cooling in a field of 1000 Oe (field-cool).

Resonant X-Ray scattering (REXS) measurements were performed at beamline I16, Diamond Light Source Ltd. [99] on single grain samples of each composition. The beamline optics were tuned to the ruthenium L3 absorption edge (2.828 keV). At this energy, the focused spot size was about of 180x50 μm^2. Measurements were made with an in-vacuum Pilatus-3 (Dectris) area detector and the scattered beam polarization was analyzed with a highly oriented graphite plate aligned to measure the (002) reflection with an avalanche photo-diode at about 90° to the scattered beam.

Only the (003), (013) and (103) resonant reflections have been investigated, using the (004) reflection to normalize for crystal quality between samples. The resonant spectra for each reflection below and above the magnetic transition are shown in Fig. 3.24. The resonant behavior is a combination of magnetic scattering from the ordered magnetic structure and a non-magnetic part related to the anisotropy of the atomic orbitals. The magnetic part is much stronger below the magnetic transition temperature. Following the resonant peaks on both reflections as the temperature is decreased, there is a clear difference in behavior between the pure compound and those with any level of Mn doping, shown in Fig. 3.25.

Magnetic transitions are evident from significant increases in resonant intensity in all of the samples. In each case these changes coincide with the magnetic transitions observed with magnetization measurements. All Mn-doped samples show a large enhancement of the (103) reflection, consistent with a B-centered magnetic structure. Of these, only the 3% sample shows an intensity variation of the (013) reflection similar to the one observed for the pure compound. The magnetic transitions temperatures, extrapolated from the fit of the temperature dependence of the resonant reflections for each Mn content, are reported in Tab. 3.9. These values exhibit a linear increase with Mn concentration.

Fig. 3.26(a) shows the evolution of the magnetic ordering as a function of the Mn content, as deduced by the L3 resonant behavior measured at 10 K (Fig. 3.26(a) bottom). Both figures are dominated by the signal near 2.838 KeV, associated with the t_{2g} multiplet responsible for the magnetic ordering. The e_g states (at 2.842 KeV),

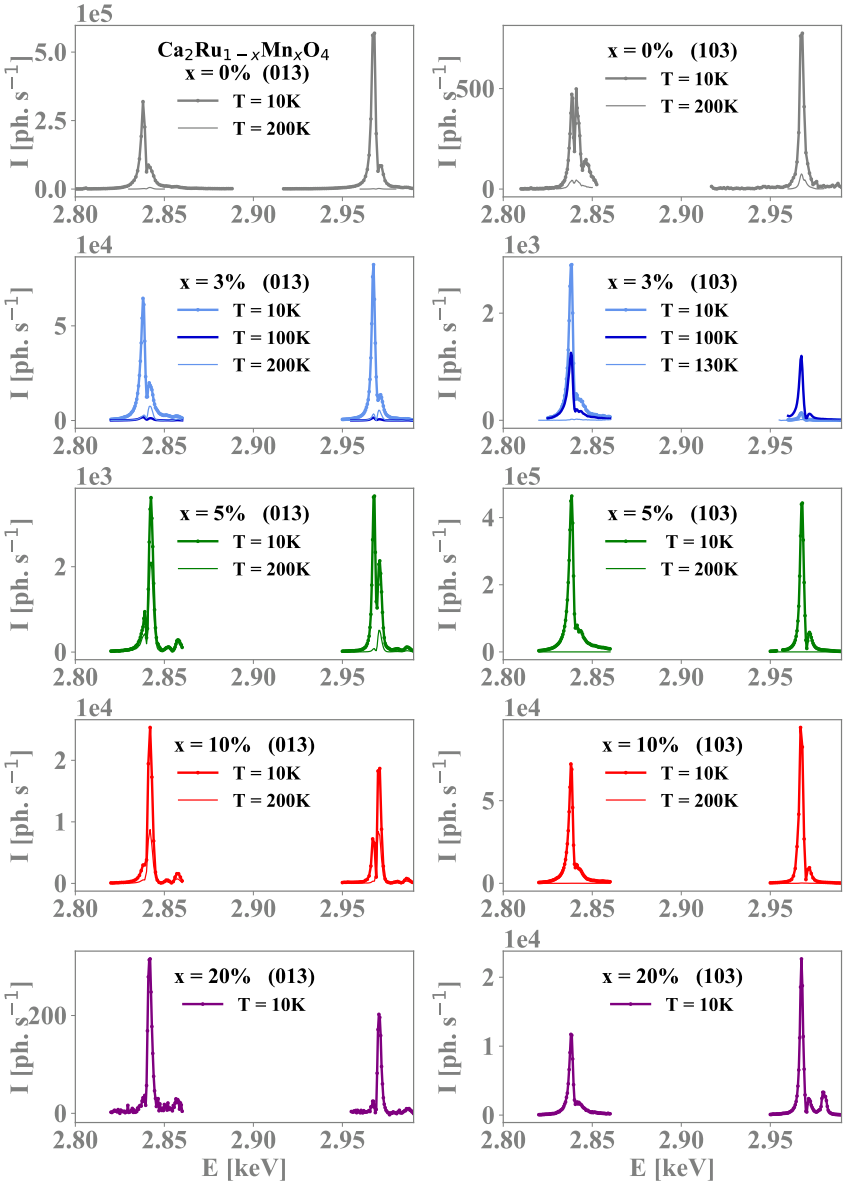

Figure 3.24: Resonant X-Ray spectra at the Ru L3 and L2 absorption edge for reflections (013) and (103) at various temperatures. Spectra are normalised by the (004) charge reflection.

Mn %	Mag. Structure	T_N
0	A-centered	106.2(7)
3	B-centered	116.14(2)
5	B-centered	123.1(5)
10	B-centered	135.4(4)
20	B-centered	140.2(2)

Table 3.9: Transition temperatures of the ordered magnetic phase in different Mn concentrations.

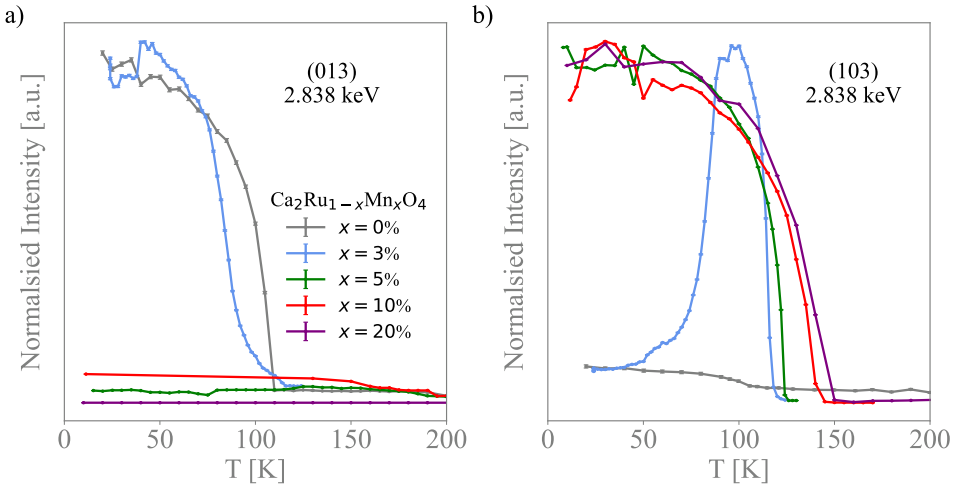

Figure 3.25: Variation of intensity with temperature at the resonant edge at the a) (013) and b) (103) reflections. The intensity of each dependence is normalised to the maximum magnetic signal in each sample.

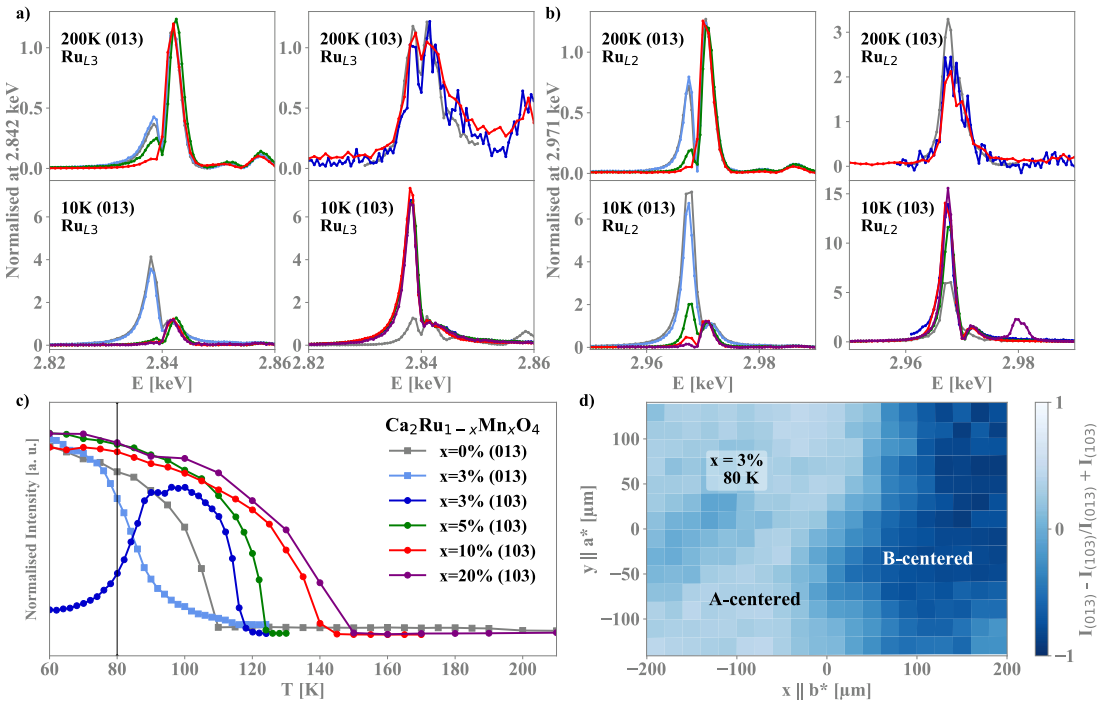

Figure 3.26: Resonant X-Ray spectra at the Ru-L3 (a) and Ru-L2 (b) edges on two charge-forbidden reflections. Below the transition (10 K), the two reflections are dominated by resonant magnetic scattering from the A-phase (013), or the B-phase (103). Above the transition (200 K), the remaining resonant signal is sensitive to the orbital occupation and the variation with Mn concentration indicates a shift in orbital population. (c) The temperature dependence of the resonant reflections highlights the variation of the magnetic transition with concentration and the switch between the A and B magnetic phase in the 3% sample. (d) The variation in reflection intensity of the two reflections at 80 K across the surface of the 3% sample, indicating the presence of magnetic domains of the two magnetic phases.

largely unaffected by the magnetic ordering, were used for renormalization to allow the comparison between different samples. In the case of pure CRO at 10 K a large signal is present on top of the (013) reflection, whereas almost no variation compared to the paramagnetic signal is present on top of the (103) reflection, as expected in the case of an A-centered magnetic ordering.
For all the Mn concentration above 3% we found a reversed situation, with a large enhancement present on top of the (103) reflection and almost no enhancement on top of the (013), clearly indicating that the B-centered magnetic ordering was realized in these compounds. In the 3% system (light blue curve) the two magnetic orderings coexist, and a large enhancement is present on the forbidden reflections.
The thermal evolution of the (013) and (103) measured on top of the t_{2g} multiplet (E = 2.838 KeV) presented in Fig. 3.26(c) confirms the different magnetic ordering, whereas the change in the ordering temperature from the A to the B phase provides an estimate of the variation in the global strength of the effective exchange couplings. In the 3% system, where the two magnetic orderings are nearly degenerate and closely competing, above 90 K the system tends to prefer the B-centered magnetic structure but the A-centered structure is already present and slowly grows with reducing the temperature. Below 90 K, the A-centered structure dominates the magnetic landscape. A sample map at 80 K with a 20x20 μm^2 resolution confirmed the presence of both phases in the whole crystals but with a change of relative weight across different areas (Fig. 3.26(d)), whose origin is not associated with any variation in the Mn content, as Scanning Electron Microscope measurements revealed that the Mn content is homogeneous across the same sample with an accuracy of 10% of the nominal concentration. Such a situation could appear, however, due to local formation of B-centered structure at high temperature, which then persists below the transition to the A-centered phase due to domain formation via the FM field exerted by canting in the B-centered structure.
The comparison of the spectra with increasing the Mn content reveals a significant jump in the intensity associated with the t_{2g} multiplet related to the reflection (013) (Fig. 3.26(b) top left) with the two samples that exhibit a transition toward the A-type magnetic phase (0 and 3%) at T_N showing a much larger feature. This pervasive feature can be associated with the local spin orbit coupling modifying the electronic distribution of the t_{2g} states and altering the specific density of states projection seen in resonant condition on the 0 and 3% compared with the 5 and 10% samples. This behavior provides experimental support to the electronic changes suggested in the t_{2g} levels and can be related to the structural changes occurring in the doped samples and presented in Fig. 3.23(c). These structural changes are well established in pure CRO [25] and have also been reported for a range of different doping regimes highlighted in Fig. 3.23(c).
As with other Ruddlesden–Popper based systems, CRO shows a still not fully understood uniaxial negative thermal expan«sion, in this case along the b-axis, accompanied

by rotation, tilting and flattening of the octahedra under cooling that does not change the space group symmetry of the system. When Ru is replaced by Mn, the substitution moderates the structural distortion at the MIT and reduces the flattening of the octahedra, primarily induced by a reduction in the planar RuO1 bond length and reduced octahedral rotation. This leads to decreased paths between neighboring Ru ions in all directions except between planes along the a-axis, which sees a slight increase on the Ru–O2–O2–Ru$(1/2, 0, 1/2)$ path through the apical O2 oxygen.

Single crystal X-Ray characterization as a function of temperature

Small single crystal samples of each Mn concentration were measured between 90 K and 500 K using an X-Ray diffractometer with liquid nitrogen cryojet. At each temperature, full coverage to a high angle of reciprocal space was obtained and refinements were performed to determine the octahedral bond lengths. The temperature dependences of the lattice and the atomic structure are shown Figs. 3.27 and 3.28, respectively.

The pure compound is subject to significant structural variations in the atomic bond lengths and distortion angles with temperature, including a negative thermal expansion, particularly along the b-axis. This structural evolution becomes less pronounced as the Mn content is increased, highlighted by the decreasing variation in volume and lattice parameters shown in Fig. 3.27. The reduction in volume with increased dopant concentration is primarily led by a reduction in the RuO_1 bond length causing decreased flattening of the octahedra combined with a reduction in the octahedral rotation. The jump in volume at high temperature, normally marked by the insulator-metal transition, also becomes significantly less pronounced as manganese is added. This again is seen in other transition metal doping regimes for CRO, with a flattening of the MIT noted when doping with Sn [100] and the disappearance of the MIT when doing above 10% with Ti [101] and Cr [57]. The flattening of the MIT is however in stark contrast with doping regimes replacing the alkali site, for instance when replacing Ca with Sr [23, 48] or La [26, 36], where the structural transition follows T_{MIT} as it decreases.

Fig. 3.29 shows the variation in exchange path distance between neighboring Ru ions with Mn content at different temperatures. Increasing Mn content does not change the thermal evolution of the path lengths but does decrease the in-plane path lengths. Out of plane exchange paths are changed less but are reduced along the b-axis and increased along the a-axis with the difference between pathways along the two directions decreasing as doping is increased.

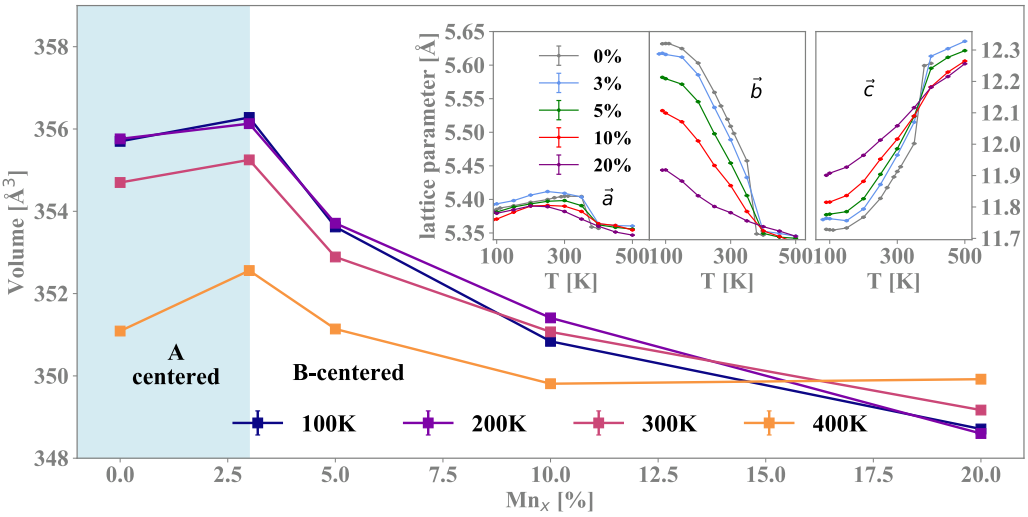

Figure 3.27: Cell volume of $Ca_2Ru_{1-x}Mn_xO_4$ as a function of Mn concentration (x) and temperature (T), determined by X-Ray diffraction. The thermal evolution of the lattice parameters of each composition are given in the inset.

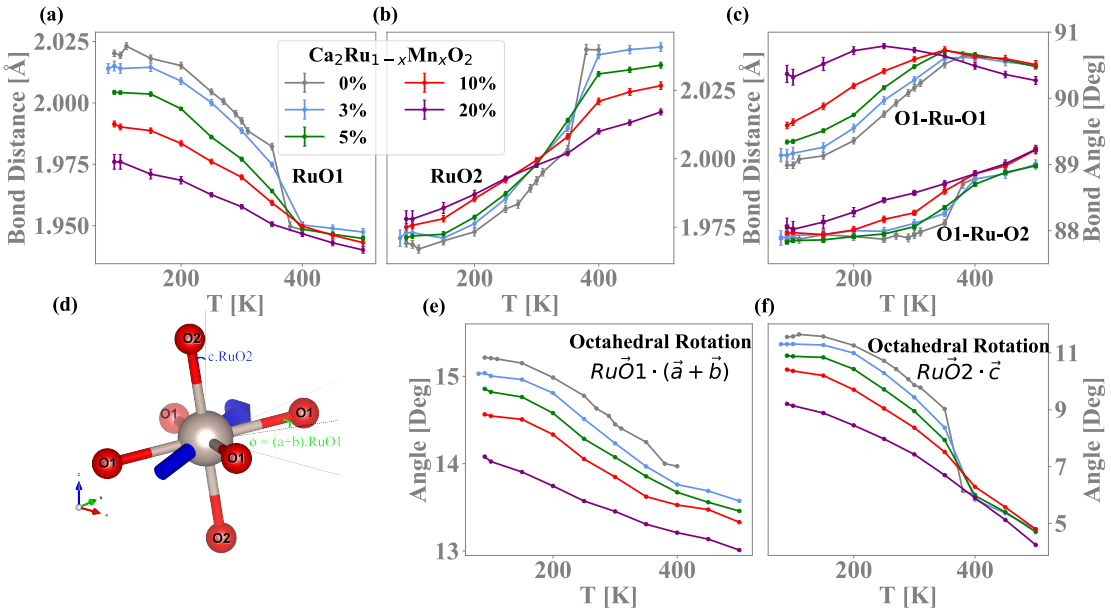

Figure 3.28: Variation with temperature of refined structure parameters from single crystal XRD measurements. Panels (a) and (b) show the change in planar Ru-O_1 and apical Ru-O_2 bond distance, respectively. Panel (c) gives the internal bond angles within the octahedra. The octahedral distortions angles, as defined in panel (d), are shown in panels (e) and (f).

Magnetisation

The field-cooled magnetization of each composition were characterized in both in-plane directions. The measured magnetic moment of all compositions, given in Fig. 3.30, indicate an increasing magnetic transition temperature with increasing Mn content. As found in other systems [102], the replacement of ruthenium induces a weak ferro-

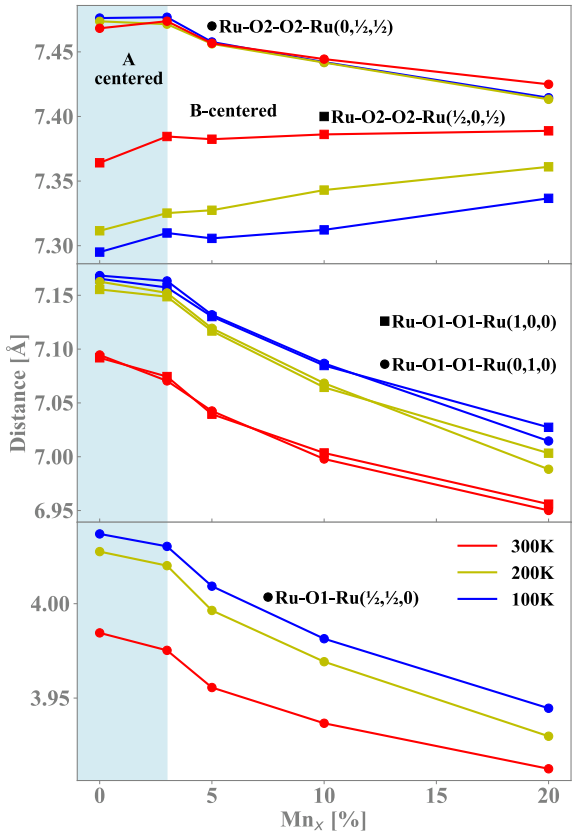

Figure 3.29: Variation in exchange path distance between neighboring Ru ions with Mn content, determined using atomic positions from X-Ray refinements.

magnetic response by the increased moment at low temperature below the ordering transition. The moment increases logarithmically up to 5% but plateaus at higher concentrations, suggesting the ferromagnetic moment is not due to increasing numbers of ferromagnetically ordered Mn ions. In the case of the 3% sample we also see a second transition and a lowering of the moment at a second, lower magnetic transition, such a magnetic response has also been reported when doping with small amounts of Fe [59, 103].

Final remarks

Substitutional doping of Mn in Ca_2RuO_4 allowed through the use of X-Ray scattering techniques to control and measure the subtle change in magnetic ordering induced without symmetry change. REXS measurements allow to unambiguously determine the magnetic ordering and separate the change in orbital population from structural changes observed through traditional X-Ray diffraction measurements.
Since the transition can be induced by means of atomic substitution, the results achieved set out new paths for the design of magnetic phases by dopants engineer-

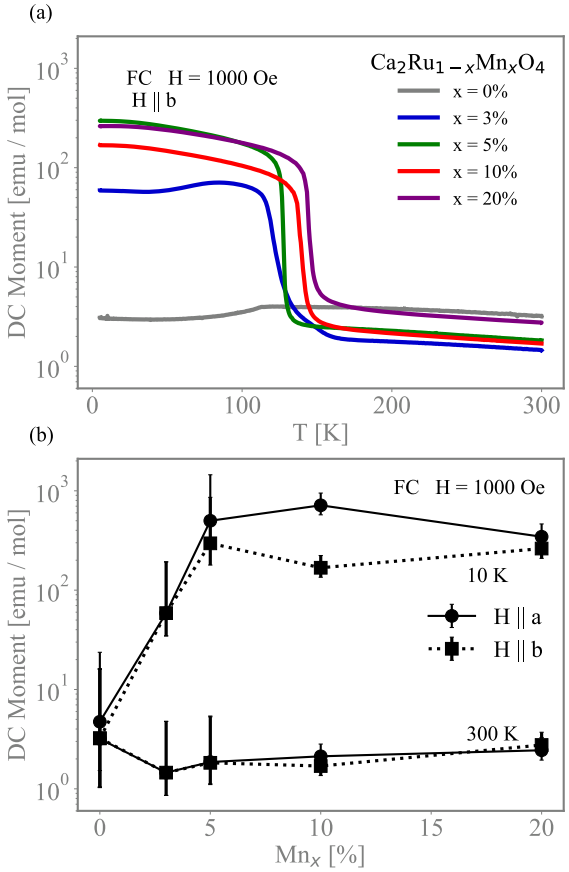

Figure 3.30: Magnetization measurements of single crystal samples. (a) Measurements on heating in a static field after cooling in zero field, indicating magnetic ordering transitions and a FM moment in the doped samples. The size of the measured molar moment below and above the transition is given in (b).

ing or, in perspective, by exploiting surface deposition in ultrathin films to induce magnetic surface reconstructions. Moreover, the possibility of achieving a mechanism to control magnetic properties through nonsymmorphic symmetry elements paves the way to novel materials design with topological antiferromagnetic phases, accompanied by spin-orbital excitations that can be confined at the edge between A and B magnetic domains and in general robust to perturbations due to symmetry based topological protection.

3.3.2 Electronic structure investigation in the current driven insulator-to-metal transition in Ca_2RuO_4 by angle-resolved photoemission spectroscopy

This section reports Nano ARPES experiments where a dc current is applied to Ca_2RuO_4 single crystals. The latter have been grown at the Musa Lab of CNR-SPIN

before the beginning of the present Phd thesis. The results have been obtained in collaboration with the group of Prof. Philip Hofmann from Aarhus University (DK). As discussed in Chapter 1 in Ca_2RuO_4 the insulator-to-metal transition (IMT) can be triggered not only by electric fields and currents [27, 37, 104], but also by temperature [22, 51], pressure [42], doping [21] and strain [46]. The current-induced IMT in this system has been investigated using a large variety of tools. While the results are not generally consistent, owing to the complexity of the phase diagram and the still disputed role of Joule heating [38, 105, 106, 107], there are several established experimental facts: (1) The transition's fingerprint is a region of negative differential resistance in transport measurements [29, 37, 38, 104]; (2) macroscopically, the transition proceeds across the sample starting from the negative electrode [38, 105, 106, 107]; and (3) the IMT is strongly coupled to a structural phase transition involving an expansion of the crystal's c axis: Starting from the so-called "S-phase" with a short c axis, a fully metallic "L-phase" emerges, with a significant c axis expansion. Diffraction techniques confirm the trend of c-axis expansion, accompanied by the simultaneous presence of different structural phases [29, 92, 108, 109, 110]. Joule heating might play a role in creating some of these [92].
Manifestly absent from the experimental results are direct characterizations of the electronic structure in the current-induced phase. Such information can, in principle, be obtained from angle-resolved photoemission spectroscopy (ARPES), but the application of photoemission techniques is hindered by a simple experimental limitation: in a current-carrying sample, the voltage drop inside the sample area illuminated by the ultraviolet (UV) light spot for photoemission is sufficiently large to completely deteriorate the energy resolution of the experiment. In our experiment, this problem was solved by using a very small light spot, on the order of a few μm, allowing us to characterize the electronic structure throughout the IMT. In addition to spectroscopic information, this approach also gives access to the local potential landscape on the surface, and we can thus use it as a local transport measurement [111, 112].

Experimental methods

Single crystals of Ca_2RuO_4 for nano-ARPES experiment were grown using the floating zone technique with Ru self-flux [93], as described in the previous chapter. The structural quality, chemical composition and electrical properties of the samples were tested by X-ray diffraction, scanning electron microscopy, energy dispersive spectroscopy, electron backscattered diffraction and resistivity measurements.
Photoemission experiments were carried out at the ANTARES beamline of the SOLEIL synchrotron facility, in France [113], using 65 eV p-polarized radiation. Samples were glued on an insulating (Al_2O_3) carrier using EPO-TEK H74F non-conductive epoxy and contacted from the side by DuPont 4922N silver paint with an embedded silver

wire. They were cleaved along the *ab* plane *in situ*, in a vacuum better than 5×10^{-10}. mbar. Because of this, and since the cleaving process leaves an unpredictable sample thickness, the thickness of the sample can only be estimated after the experiment. The dimensions were determined to be 1180 μm long by 760 μm wide by 120 μm thick. The resulting cross section, which was used to estimate the current densities, is 9.12×10^{-3} cm^{-2}. The spatial resolution of the measurements was determined by scanning across a sharp feature. For this scan, a lateral step size of 1 μm was used, and found the resolution to be 3.6 μm.
The temperature of the sample was held constant at 200 K for the whole duration of the experiment, although local Joule heating cannot be excluded. The sample current was generated by a Keithley 2450. After every increase in current, and before measuring, the voltage was allowed to stabilize for 20 minutes.

Angle-resolved photoemission spectroscopy measurements

The setup of the experiment is shown in Fig. 3.31(a). The sample is electrically contacted from the sides, so that both the electronic structure and the current-induced potential landscape can be mapped by the scanning of a highly focused UV beam across the sample surface. When this is done as a function of the applied current, it results in a five-dimensional data set: the photoemission intensity as a function of the spatial coordinates x and y, kinetic energy E_k, emission angle Θ and the current I. Due to the presence of the electric field accompanying the current density, the spectra collected at different points are displaced in energy. Fig. 3.31(b) shows an optical microscopy image of the sample used in this experiment. The current-dependent electronic structure has been studied in the area outlined by the orange square. The inset of Fig. 3.31(b) shows a map of the integrated photoemission intensity in this region, with intensity changes that clearly correspond to the sample's microscopic morphology.
Fig. 3.31(c) shows the macroscopic I/V curve, obtained from the applied current and the voltage drop across the entire sample. This is compared to a local I/V curve (Fig. 3.31(d)) derived from the potential gradient measured by ARPES [111]. This gradient $| \bigtriangledown V|$ was determined by tracking the fitted position of the photoemission peak (the B, see later) across the sample and averaging the obtained gradient values over the black square in the inset of Fig. 3.31(c). The two I/V curves reported in Fig. 3.31(c) and Fig. 3.31(d) show the shape typical for the current-induced IMT, with a pronounced region of negative differential resistance [29, 37, 38, 104]. It's important to note that the local I/V curve is equivalent to a genuine four-point measurement and is thereby different from the external measurement, which includes the sample's contact resistance. The similarity of the two I/V curves is essential for the interpretation of the spectroscopic data below: it shows that the local spectroscopic measurements

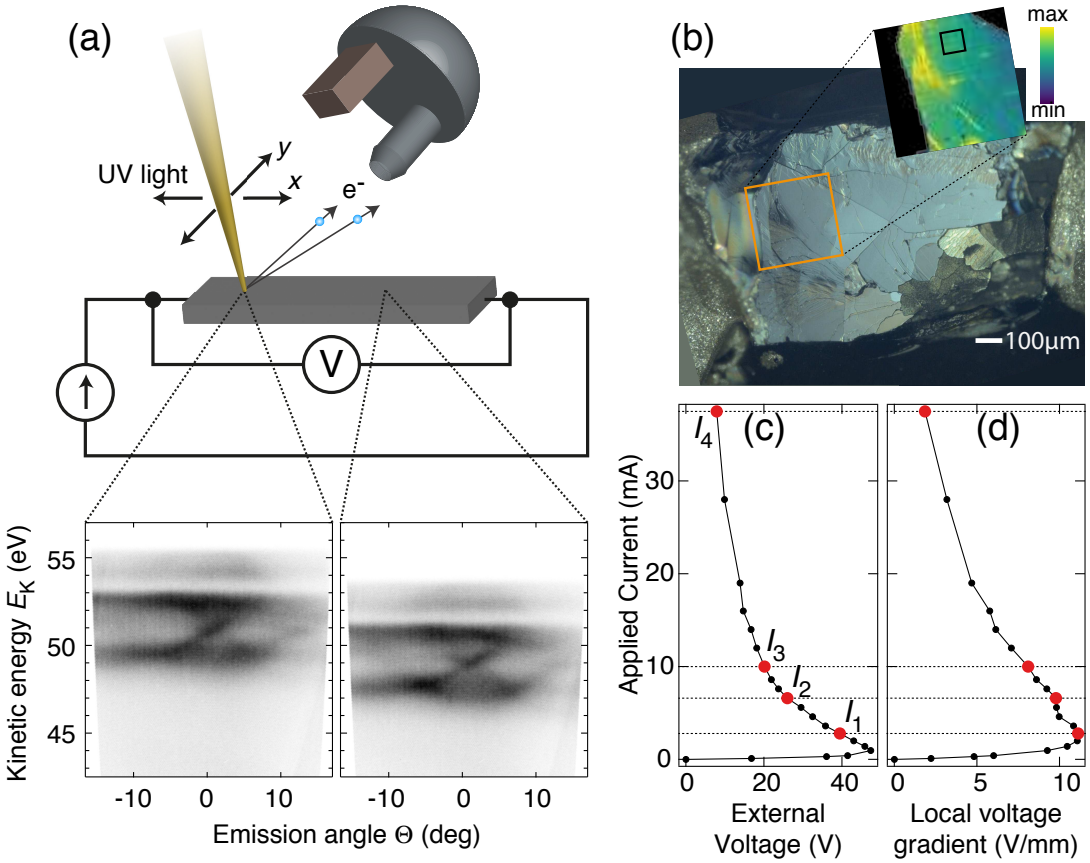

Figure 3.31: (a) Sketch of the experiment. The sample is exposed to a transport current in the *ab* plane. The resulting voltage drop leads to a continuous energy shift of all states between the two electrodes. ARPES measurements are performed using a highly focused UV beam that is scanned across the surface, giving local spectra (photoemission intensity as a function of energy and emission angle) that are displaced in energy, following the local potential landscape across the sample. (b) Optical microscope image of the sample after the experiment. The contacts are seen on the left and right hand side. The area explored by ARPES is marked by an orange square. The inset shows a map of the photoemission intensity inside this area. (c) Externally measured I/V curve and (d) local I/V curve obtained from averaging the observed energy shift between the spectra within the black square marked in the inset of panel (b). The red markers indicate the current values for which data is displayed in Fig. 3.32 and Fig. 3.33.

reported here are representative of a sample area undergoing the IMT.

The spectroscopic changes accompanying the IMT are illustrated in Fig. 3.32 by measurements of the photoemission intensity throughout the Brillouin zone for three selected currents. The low-current spectrum at I_1 is taken close to the turning point of the I/V curve, *i.e.*, close to the highest electric field, demonstrating the feasibility of the approach: despite the field, the spectrum agrees very well with published equilibrium results [32, 46, 47]. The two flat bands at low binding energies (marked by arrows) are related to the d_{zx} and d_{yz} states of the Ru-4d t_{2g} manifold. In the insulating S-phase, these are half-filled, and are a manifestation of the lower Hubbard

band in a Mott state driven by Coulomb interactions [47]. The remaining d_{xy} band is fully occupied, and thus insulating. It gives rise to the circular intensity feature marked by arrows in Fig. 3.32(a) and (b). The more intense bands at higher binding energy are primarily derived from oxygen states. The IMT to a conducting L-phase

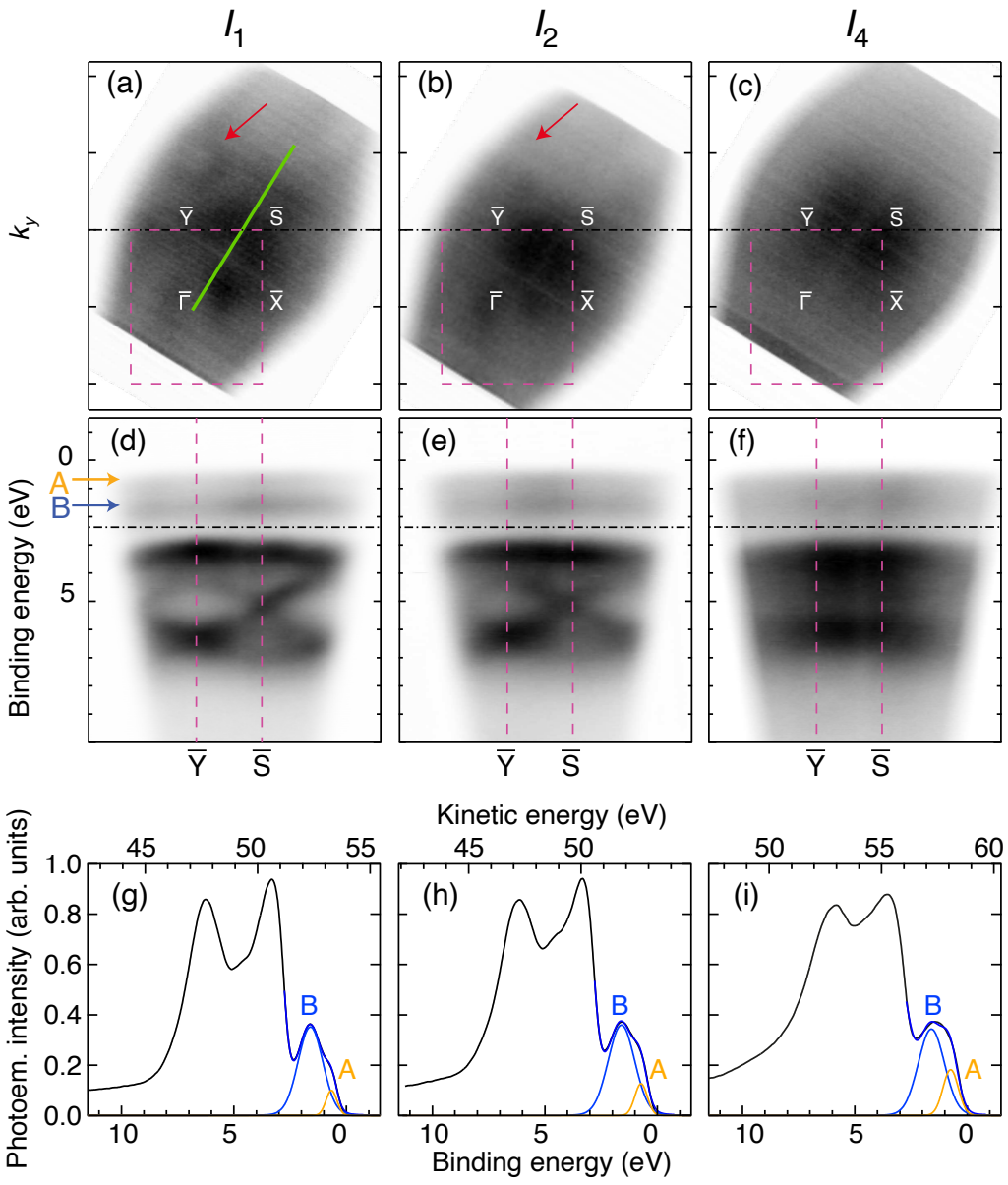

Figure 3.32: Spectral changes accompanying the IMT: (a)-(c) Photoemission intensity at a binding energy of 2.37 eV for I_1, I_2, I_4 (see markers on Fig. 3.31(c)). The surface Brillouin zone is superimposed. The green line marks the direction and range of the spectra in the multidimensional data set and in Fig. 3.33. The red arrow marks a circular constant energy contour stemming from the d_{xy} states. (d)-(f) Intensity as a function of energy along the $\bar{Y}$ $\bar{S}$ direction. (g)-(i) Angle-integrated energy distribution curves derived from data at I_1, I_2, I_4, respectively, integrated along the path identified by the green line in (a). The photoemission intensity at low binding energy has been fitted by two peaks, A and B, in the same way as in Ref. [47]. The fit components are shown and the positions are also marked in panels (d)-(f).

is predicted to drastically change the electronic structure, resulting in a metallic state with a large Fermi surface [114]. Clearly, this is at odds with the ARPES results, which show an absence of Fermi level crossings at the higher currents I_2 and I_4 (see Fig. 3.32). Indeed, an increased current only results in minor changes of the spectra. The signature of the Mott state remains and the most prominent effect appears to be a mere k-broadening that washes out the dispersive features. This is particularly evident in the oxygen bands, but it also takes place in the Ru states. The broadening can either signal that $k_{||}$ ceases to be a good quantum number, possibly because of the creation of defects or small crystalline domains, or it can point towards the simultaneous existence of structural domains with slightly different electronic structures, such that their incoherent superposition is observed in this experiment. Both mechanism are consistent with the observation of a broad distribution of structural modifications in diffraction experiments [92, 108, 110]. The persistence of the Mott state in all of these structural modifications is a key result of this measurements.

An important question is to what degree spectral intensity is filled into the Mott gap, triggering the transition in conductivity. In ARPES studies of superconductors or charge density systems, this can be answered very precisely by aligning all spectra to the Fermi energy E_F of the sample or to that of a metal in contact with the sample [115]. In Ca_2RuO_4 this is not possible, due to the field-induced shifts between the spectra, which completely eliminate a common reference energy. For a removal of these energy shifts it was necessary first reduce the complexity of the spectra, by integrating each of them along the emission angle, resulting in angle-integrated energy distribution curve (EDC), as shown in Fig. 3.32(g)-(i). The integration in angle is justified by the very small dispersion observed, especially in the $\{d_{zx}, d_{yz}\}$ bands. Each EDC is fitted by two Gaussian peaks in the $\{d_{zx}, d_{yz}\}$ energy region, called A and B [47]. These fits are also shown in Fig. 3.32(g)-(i). We then choose a common energy reference point. The A peak is clearly unsuitable because it is closest to the gap where spectral changes are expected. Instead, the B peak was used, which appears to be a good choice for two reasons: (1) It represents a flat band in the equilibrium state; and (2) in contrast to the A peak, it is only weakly affected by the corresponding strain-induced IMT [46]. Therefore, we align the B peak energy in all the spectra 78141 spectra of the now four-dimensional data set. Combining this with the energy difference between the B peak and E_F in equilibrium (1.60 eV, measured against a Fermi edge of polycrystalline Au), we obtain the local E_F for every spectrum. The spectra in Fig. 3.32 are already aligned in this way and are shown as a function of binding energy. The original kinetic energy is also given for panels (g)-(i).

The energy alignment of the spectra now opens the possibility to study the IMT throughout the entire dataset. To this end, Fig. 3.33(a) shows the hallmark of the IMT, the in-gap spectral weight, taken as the integrated intensity in the energy range around the local E_F for maps taken at the currents marked in Fig. 3.31(c). As expected, the in-gap intensity increases with the current throughout the sample. Moreover, the

build-up of in-gap intensity initiates at the negative electrode (on the left hand side), consistent with the optical observation of the phase transition [38, 105, 106, 107]. This is clearly seen by the yellow edge developing on the left hand side of the sample in Fig. 3.33(a) in the panel for I_2. This spreads from left to right across the image as seen for I_3, eventually leading to the situation of I_4. Fig. 3.33(b) shows the spectral development at a selected point in the maps (marked with a white box in (a)), and panel (c) gives the corresponding integrated EDCs in the region of the A and B peaks. The evolution is consistent with that in Fig. 3.32 and the increase of spectral weight in the gap, while small, can be observed in the EDCs. Fig. 3.33(d) and (e) give the esti-

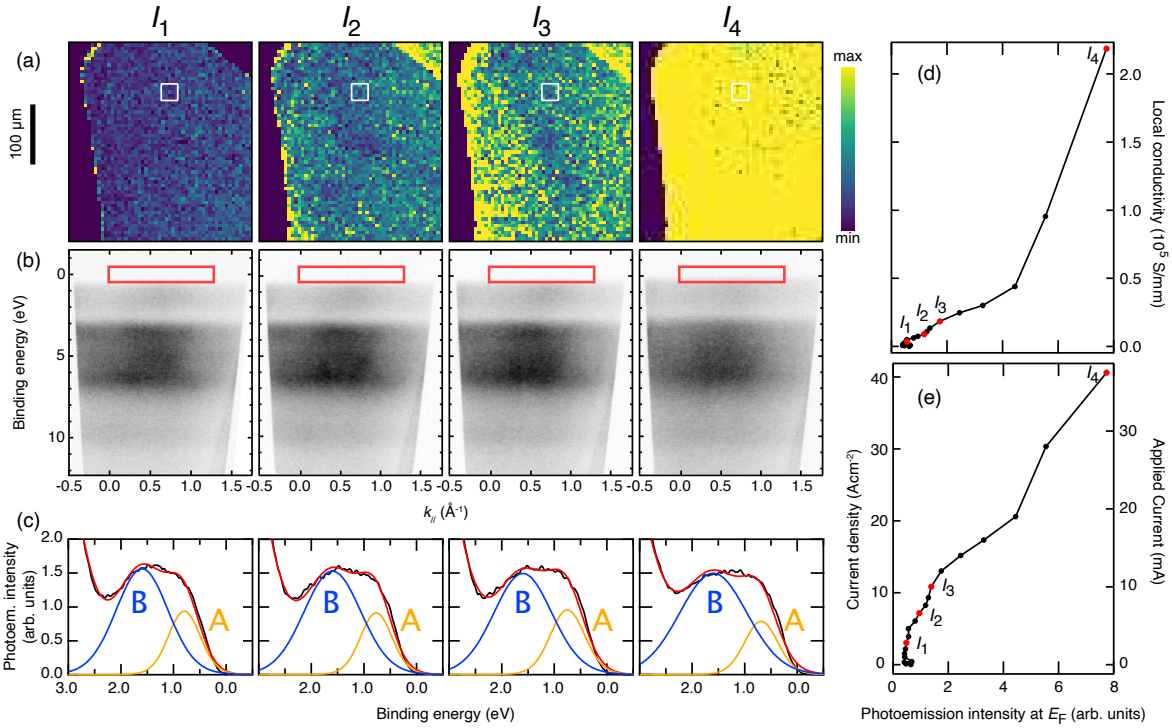

Figure 3.33: Mapping the IMT throughout the data set. (a) In-gap photoemission intensity across the sample for selected currents marked in Fig. 3.31(c). The integration region is given by the red rectangles in panel (b). (b) Corresponding photoemission spectra at the location marked by a white rectangles in panel (a). (c) Angle-integrated energy distribution curves obtained from the spectra in panel (b). (d) Estimated local conductivity and (e) applied current as a function of in-gap photoemission intensity, integrated over the red rectangles in panel (b).

mated local conductivity and the applied current as a function of in-gap photoemission intensity, respectively. The local conductivity was estimated with the assumption of a uniform current distribution through the whole sample. After we found the current density J and $|\bigtriangledown V|$, we calculated the conductivity from $\sigma = J/|\bigtriangledown V|$. Both curves show the expected correlation between the quantities, with a clear increase of conductivity starting near the turning point of the I/V curve in Fig. 3.33(c) and additional changes at very high currents where Joule heating is likely to play an important role in accelerating the transition.

An IMT with a persistent Mott signature appears to be at odds with the conventional theoretical understanding of IMTs induced by temperature, strain, electric fields or applied currents [31, 46, 108, 114, 116]. However, a potentially important element missing in the corresponding calculations is the structural inhomogeneity accompanying the IMT. We show that this inhomogeneity is indeed essential for an understanding of the IMT by considering a simple model in which Ca_2RuO_4 structural units with a slightly different c-axis parameter are interfaced with each other. To this end, Fig. 3.33(a) compares the electronic density of states (DOS) for the equilibrium S-phase and a modified S'-phase with a small (3%) expansion of the c-axis. The influence of the structural change is very small. Both phases are insulating with a very similar gap and the features mainly appear shifted in energy. This shift, however, is crucial as it results in an effective band gap between the valence band maximum of the S-phase and the conduction band minimum of the S'-phase that is drastically reduced compared to the gap in either of the pure phases. This smaller gap would be present at the interface between the two phases and results in an increased conductivity there. The reason for the relative energy shift is the strong covalency of the Ru 4d states combined with a distance variation between the Ru and the apical oxygen atoms that is changing the crystal field. As expected, the oxygen states are also affected by the modified interaction with the Ru atoms.

While a single interface between the S and S'-phases already captures the essence of the gap reduction, a more appropriate model for the experimental situation might be, for example, a superlattice with alternating S and S'-phases, *i.e.*, "flat" and "not-so-flat" octahedra. Such a structure is sketched in Fig. 3.34(b), constructed such that S and S'-layers are stacked with a layer of intermediate structure in between. The calculated DOS for this superlattice is also shown in Fig. 3.34(b). Now the distinction between the contributions of the individual phases loses meaning, but the reduced gap manifests itself directly in the overall DOS. The gap reduction is qualitatively similar for other choices of the superlattice.

The experimental situation is presumably more complicated than this, with inhomogeneous domain sizes that give rise to a continuum of energetically displaced and slightly different band structures. This will further increase the tendency for gap reduction and in-gap states, in excellent qualitative agreement with the ARPES results. We stress that all this proceeds without destroying the local Mott state, and that the resulting phase can be viewed as an emergent inhomogeneous band-Mott semi-metallic state. Such a state can retain the high-energy features of the Coulomb-driven insulator while allowing for an in-gap spectral weight and a conductivity increase due to the current-driven structural inhomogeneities.

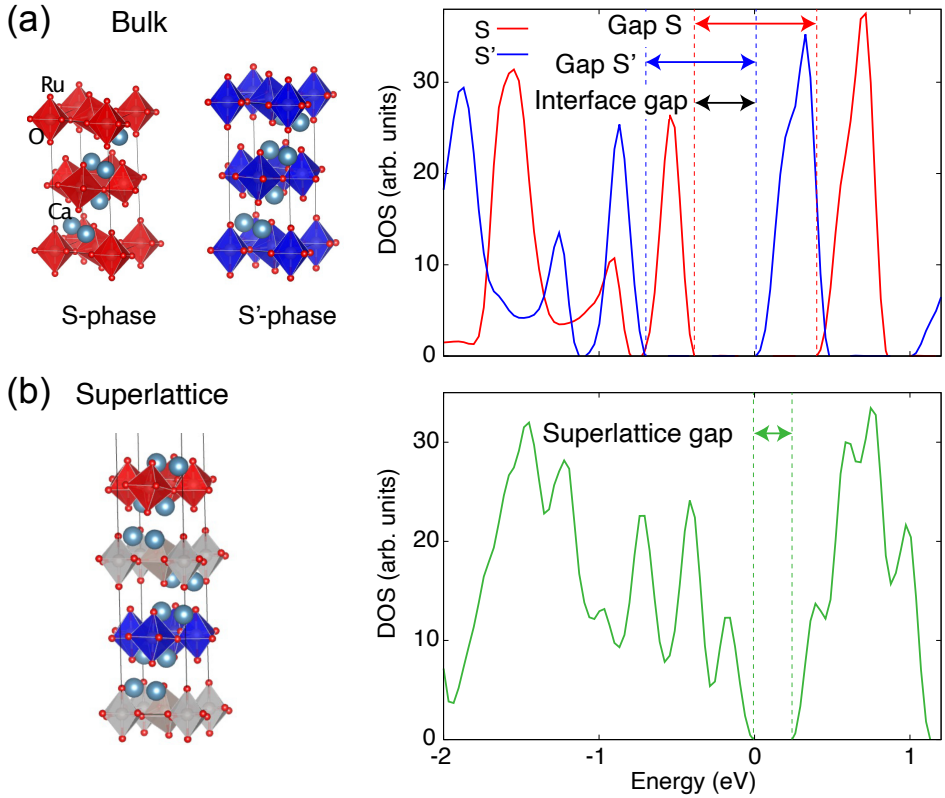

Figure 3.34: (a) Sketch of the Ca_2RuO_4 bulk crystal structures and corresponding density of states (DOS). S- and S' have unit cells with a different c axis length. S and S' are insulating with the indicated gaps but the band alignment leads to a smaller effective gap at the interface between S and S'. (b) Superlattice formed by the S and S' unit cells separated by an interface unit cell with intermediate properties (grey octahedra). The corresponding DOS shows a substantial reduction of the charge gap. The zero of the energy scale is fixed to the valence band maximum of the superlattice throughout the paper.

Conclusions

In conclusion, we have shown that the current-driven IMT in Ca_2RuO_4 leads to the expected increase of in-gap spectral weight, but that the Mott state appears to be largely retained. An emergent semi-metallic state with simultaneous Mott character can be explained by the current-induced structural inhomogeneity of the sample, because the band alignment between structurally different domains effectively reduces the overall gap. This work thus unveils a novel type of non-equilibrium semi-metallic state that forms at the interface of Mott domains. In contrast to what would be expected on the basis of well known mechanisms, this situation arises from the structural inhomogeneity of a system, and it is entirely different than the mere coexistence of insulating and metallic domains that would be expected for a first-order phase transition. The creation of a novel phase from microstructuring has not been reported in connection with the IMT in transition metal oxides, but it is somewhat reminiscent of the hidden phase in laser- or current-exposed 1T-TaS_2, where metallicity is induced in a modified

Mott phase by nano-texturing [117].

Bibliography

[1] N. F. Mott, Proceedings of the Physical Society. Section A **62**, 416 (1949).

[2] N. Mott, *Metal-Insulator Transitions* (Taylor and Francis, Ltd., London 1974, 1979).

[3] P. Fazekas, *Lecture notes on electron correlation and magnetism*, vol. 5 (World scientific, 1999).

[4] H. Tanaka and M. Misono, Current Opinion in Solid State and Materials Science **5**, 381 (2001).

[5] S. Ruddlesden and P. Popper, Acta Crystallographica **11**, 54 (1958).

[6] S. Ruddlesden and P. Popper, Acta Crystallographica **10**, 538 (1957).

[7] B. Beznosikov and K. Aleksandrov, Crystallography Reports **45**, 792 (2000).

[8] D. Lee and H. N. Lee, Materials **10** (2017), ISSN 1996-1944, URL `https://www.mdpi.com/1996-1944/10/4/368`.

[9] M. A. Yatoo and S. J. Skinner, Materials Today: Proceedings **56**, 3747 (2022), ISSN 2214-7853, first International Conference on Design and Materials, URL `https://www.sciencedirect.com/science/article/pii/S2214785321082997`.

[10] Y. Maeno, H. Hashimoto, K. Yoshida, S. Nishizaki, T. Fujita, J. G. Bednorz, and F. Lichtenberg, Nature **372**, 532 (1994), URL `https://doi.org/10.1038/372532a0`.

[11] Y. Maeno, T. M. Rice, and M. Sigrist, Physics Today **54**, 42 (2001).

[12] K. Ishida, H. Mukuda, Y. Kitaoka, K. Asayama, Z. Mao, Y. Mori, and Y. Maeno, Nature **396**, 658 (1998), URL `https://doi.org/10.1038/25315`.

[13] G. M. Luke, Y. Fudamoto, K. M. Kojima, M. I. Larkin, J. Merrin, B. Nachumi, Y. J. Uemura, Y. Maeno, Z. Q. Mao, Y. Mori, et al., Nature **394**, 558 (1998), URL `https://doi.org/10.1038/29038`.

[14] A. P. Mackenzie and Y. Maeno, Rev. Mod. Phys. **75**, 657 (2003), URL https://link.aps.org/doi/10.1103/RevModPhys.75.657.

[15] A. Pustogow, Y. Luo, A. Chronister, Y. S. Su, D. A. Sokolov, F. Jerzembeck, A. P. Mackenzie, C. W. Hicks, N. Kikugawa, S. Raghu, et al., Nature **574**, 72 (2019), URL https://doi.org/10.1038/s41586-019-1596-2.

[16] G. Cao, O. Korneta, S. Chikara, L. DeLong, and P. Schlottmann, Solid State Communications **148**, 305 (2008), ISSN 0038-1098, URL https://www.sciencedirect.com/science/article/pii/S0038109808005139.

[17] A. V. Puchkov, M. C. Schabel, D. N. Basov, T. Startseva, G. Cao, T. Timusk, and Z.-X. Shen, Phys. Rev. Lett. **81**, 2747 (1998), URL https://link.aps.org/doi/10.1103/PhysRevLett.81.2747.

[18] W. Witczak-Krempa, G. Chen, Y. B. Kim, and L. Balents, Annual Review of Condensed Matter Physics **5**, 57 (2014), URL https://doi.org/10.1146/annurev-conmatphys-020911-125138.

[19] S. Nakatsuji, S.-i. Ikeda, and Y. Maeno, Journal of the Physical Society of Japan **66**, 1868 (1997), URL https://doi.org/10.1143/JPSJ.66.1868.

[20] S. Nakatsuji, S. ichi Ikeda, and Y. Maeno, Physica C: Superconductivity **282-287**, 729 (1997), ISSN 0921-4534, proceedings of the International Conference on Materials and Mechanisms of Superconductivity High Temperature Superconductors V Part II, URL https://www.sciencedirect.com/science/article/pii/S0921453497005455.

[21] S. Nakatsuji and Y. Maeno, Phys. Rev. Lett. **84**, 2666 (2000), URL https://link.aps.org/doi/10.1103/PhysRevLett.84.2666.

[22] C. S. Alexander, G. Cao, V. Dobrosavljevic, S. McCall, J. E. Crow, E. Lochner, and R. P. Guertin, Phys. Rev. B **60**, R8422 (1999), URL https://link.aps.org/doi/10.1103/PhysRevB.60.R8422.

[23] O. Friedt, M. Braden, G. André, P. Adelmann, S. Nakatsuji, and Y. Maeno, Phys. Rev. B **63**, 174432 (2001), URL https://link.aps.org/doi/10.1103/PhysRevB.63.174432.

[24] G. Cao, S. McCall, M. Shepard, J. E. Crow, and R. P. Guertin, Phys. Rev. B **56**, R2916 (1997), URL https://link.aps.org/doi/10.1103/PhysRevB.56.R2916.

[25] M. Braden, G. André, S. Nakatsuji, and Y. Maeno, Phys. Rev. B **58**, 847 (1998), URL https://link.aps.org/doi/10.1103/PhysRevB.58.847.

[26] G. Cao, S. McCall, V. Dobrosavljevic, C. S. Alexander, J. E. Crow, and R. P. Guertin, Phys. Rev. B **61**, R5053 (2000), URL https://link.aps.org/doi/10.1103/PhysRevB.61.R5053.

[27] F. Nakamura, M. Sakaki, Y. Yamanaka, S. Tamaru, T. Suzuki, and Y. Maeno, Scientific Reports **3**, 2536 (2013), URL https://doi.org/10.1038/srep02536.

[28] T. Qi, Theses and dissertations − physics and astronomy, University of Kentucky (2012).

[29] C. Cirillo, V. Granata, G. Avallone, R. Fittipaldi, C. Attanasio, A. Avella, and A. Vecchione, Phys. Rev. B **100**, 235142 (2019), URL https://link.aps.org/doi/10.1103/PhysRevB.100.235142.

[30] V. Anisimov, I. Nekrasov, D. Kondakov, T. Rice, and M. Sigrist, The European Physical Journal B-Condensed Matter and Complex Systems **25**, 191 (2002).

[31] E. Gorelov, M. Karolak, T. O. Wehling, F. Lechermann, A. I. Lichtenstein, and E. Pavarini, Phys. Rev. Lett. **104**, 226401 (2010), URL https://link.aps.org/doi/10.1103/PhysRevLett.104.226401.

[32] T. Mizokawa, L. H. Tjeng, G. A. Sawatzky, G. Ghiringhelli, O. Tjernberg, N. B. Brookes, H. Fukazawa, S. Nakatsuji, and Y. Maeno, Phys. Rev. Lett. **87**, 077202 (2001), URL https://link.aps.org/doi/10.1103/PhysRevLett.87.077202.

[33] C. G. Fatuzzo, M. Dantz, S. Fatale, P. Olalde-Velasco, N. E. Shaik, B. Dalla Piazza, S. Toth, J. Pelliciari, R. Fittipaldi, A. Vecchione, et al., Phys. Rev. B **91**, 155104 (2015), URL https://link.aps.org/doi/10.1103/PhysRevB.91.155104.

[34] J. Lotze and M. Daghofer, Phys. Rev. B **104**, 045125 (2021), URL https://link.aps.org/doi/10.1103/PhysRevB.104.045125.

[35] I. Vergara, M. Magnaterra, P. Warzanowski, J. Attig, S. Kunkemöller, D. I. Khomskii, M. Braden, M. Hermanns, and M. Grüninger, Phys. Rev. B **106**, 085103 (2022), URL https://link.aps.org/doi/10.1103/PhysRevB.106.085103.

[36] H. Fukazawa and Y. Maeno, Journal of the Physical Society of Japan **70**, 460 (2001), URL https://doi.org/10.1143/JPSJ.70.460.

[37] R. Okazaki, Y. Nishina, Y. Yasui, F. Nakamura, T. Suzuki, and I. Terasaki, Journal of the Physical Society of Japan **82**, 103702 (2013), URL https://doi.org/10.7566/JPSJ.82.103702.

[38] J. Zhang, A. S. McLeod, Q. Han, X. Chen, H. A. Bechtel, Z. Yao, S. N. Gilbert Corder, T. Ciavatti, T. H. Tao, M. Aronson, et al., Phys. Rev. X **9**, 011032 (2019), URL https://link.aps.org/doi/10.1103/PhysRevX.9.011032.

[39] G. Avallone, R. Fermin, K. Lahabi, V. Granata, R. Fittipaldi, C. Cirillo, C. Attanasio, A. Vecchione, and J. Aarts, npj Quantum Materials **6**, 91 (2021), URL https://doi.org/10.1038/s41535-021-00394-7.

[40] G. Avallone, Theses and dissertations, University of Salerno − Dipartimento di Fisica "E.R. Caianiello" (2021).

[41] M. Imada, A. Fujimori, and Y. Tokura, Rev. Mod. Phys. **70**, 1039 (1998), URL https://link.aps.org/doi/10.1103/RevModPhys.70.1039.

[42] F. Nakamura, T. Goko, M. Ito, T. Fujita, S. Nakatsuji, H. Fukazawa, Y. Maeno, P. Alireza, D. Forsythe, and S. R. Julian, Phys. Rev. B **65**, 220402 (2002), URL https://link.aps.org/doi/10.1103/PhysRevB.65.220402.

[43] C. S. Snow, S. L. Cooper, G. Cao, J. E. Crow, H. Fukazawa, S. Nakatsuji, and Y. Maeno, Phys. Rev. Lett. **89**, 226401 (2002), URL https://link.aps.org/doi/10.1103/PhysRevLett.89.226401.

[44] P. Steffens, O. Friedt, P. Alireza, W. G. Marshall, W. Schmidt, F. Nakamura, S. Nakatsuji, Y. Maeno, R. Lengsdorf, M. M. Abd-Elmeguid, et al., Phys. Rev. B **72**, 094104 (2005), URL https://link.aps.org/doi/10.1103/PhysRevB.72.094104.

[45] H. Taniguchi, K. Nishimura, R. Ishikawa, S. Yonezawa, S. K. Goh, F. Nakamura, and Y. Maeno, Phys. Rev. B **88**, 205111 (2013), URL https://link.aps.org/doi/10.1103/PhysRevB.88.205111.

[46] S. Riccò, M. Kim, A. Tamai, S. McKeown Walker, F. Y. Bruno, I. Cucchi, E. Cappelli, C. Besnard, T. K. Kim, P. Dudin, et al., Nature Communications **9**, 4535 (2018), URL https://doi.org/10.1038/s41467-018-06945-0.

[47] D. Sutter, C. G. Fatuzzo, S. Moser, M. Kim, R. Fittipaldi, A. Vecchione, V. Granata, Y. Sassa, F. Cossalter, G. Gatti, et al., Nature Communications **8**, 15176 (2017), URL https://doi.org/10.1038/ncomms15176.

[48] S. Nakatsuji and Y. Maeno, Phys. Rev. B **62**, 6458 (2000), URL https://link.aps.org/doi/10.1103/PhysRevB.62.6458.

[49] S. Nakatsuji, D. Hall, L. Balicas, Z. Fisk, K. Sugahara, M. Yoshioka, and Y. Maeno, Phys. Rev. Lett. **90**, 137202 (2003), URL https://link.aps.org/doi/10.1103/PhysRevLett.90.137202.

[50] J. S. Lee, Y. S. Lee, T. W. Noh, S.-J. Oh, J. Yu, S. Nakatsuji, H. Fukazawa, and Y. Maeno, Phys. Rev. Lett. **89**, 257402 (2002), URL https://link.aps.org/doi/10.1103/PhysRevLett.89.257402.

[51] J. H. Jung, Z. Fang, J. P. He, Y. Kaneko, Y. Okimoto, and Y. Tokura, Phys. Rev. Lett. **91**, 056403 (2003), URL https://link.aps.org/doi/10.1103/PhysRevLett.91.056403.

[52] Z. Fang, N. Nagaosa, and K. Terakura, Phys. Rev. B **69**, 045116 (2004), URL https://link.aps.org/doi/10.1103/PhysRevB.69.045116.

[53] H. Rho, S. L. Cooper, S. Nakatsuji, H. Fukazawa, and Y. Maeno, Phys. Rev. B **68**, 100404 (2003), URL https://link.aps.org/doi/10.1103/PhysRevB.68.100404.

[54] S. Nakatsuji, V. Dobrosavljevi, D. Tanaskovi, M. Minakata, H. Fukazawa, and Y. Maeno, Phys. Rev. Lett. **93**, 146401 (2004), URL https://link.aps.org/doi/10.1103/PhysRevLett.93.146401.

[55] S. Nakatsuji and Y. Maeno, Journal of Solid State Chemistry **156**, 26 (2001), ISSN 0022-4596, URL https://www.sciencedirect.com/science/article/pii/S0022459600989539.

[56] T. Qi, M. Ge, O. Korneta, S. Parkin, L. De Long, and G. Cao, Journal of Solid State Chemistry **184**, 893 (2011), ISSN 0022-4596, URL https://www.sciencedirect.com/science/article/pii/S0022459611000740.

[57] T. F. Qi, O. B. Korneta, S. Parkin, L. E. De Long, P. Schlottmann, and G. Cao, Phys. Rev. Lett. **105**, 177203 (2010), URL https://link.aps.org/doi/10.1103/PhysRevLett.105.177203.

[58] D. G. Porter, F. Forte, V. Granata, M. Cannavacciuolo, R. Fittipaldi, M. Cuoco, A. Bombardi, and A. Vecchione, Scientific Reports **12**, 10957 (2022), URL https://doi.org/10.1038/s41598-022-14932-1.

[59] T. F. Qi, O. B. Korneta, S. Parkin, J. Hu, and G. Cao, Phys. Rev. B **85**, 165143 (2012), URL https://link.aps.org/doi/10.1103/PhysRevB.85.165143.

[60] P. Rudolph, *Handbook of crystal growth: Bulk crystal growth* (Elsevier, 2014).

[61] R. Perry and Y. Maeno, Journal of Crystal Growth **271**, 134 (2004), ISSN 0022-0248, URL https://www.sciencedirect.com/science/article/pii/S0022024804008863.

[62] S. I. Ikeda, U. Azuma, N. Shirakawa, Y. Nishihara, and Y. Maeno, Journal of Crystal Growth **237-239**, 787 (2002), ISSN 0022-0248, the thirteenth international conference on Crystal Growth in conj unction with the eleventh international conference on Vapor Growth and Epitaxy, URL https://www.sciencedirect.com/science/article/pii/S0022024801020334.

[63] R. Fittipaldi, A. Vecchione, S. Fusanobori, K. Takizawa, H. Yaguchi, J. Hooper, R. Perry, and Y. Maeno, Journal of Crystal Growth **282**, 152 (2005), ISSN 0022-0248, URL https://www.sciencedirect.com/science/article/pii/S0022024805005841.

[64] D. Chatterji and R. Vest, Journal of the American Ceramic Society **54**, 73 (1971).

[65] W. E. Bell and M. Tagami, The Journal of Physical Chemistry **67**, 2432 (1963).

[66] V. Tagirov, D. Chizhikov, E. Kazenas, and L. Shubochkin, Zhurnal Neorganicheskoj Khimii **20**, 2035 (1975).

[67] T. G. Rochow and E. G. Rochow, *Scanning Electron Microscopy* (Springer US, Boston, MA, 1978), pp. 273–298, ISBN 978-1-4684-2454-6, URL $https://doi.org/10.1007/978-1-4684-2454-6-13$.

[68] N. Instruments, Ecole polytechnique federale de Lausanne (1983).

[69] S. J. B. Reed, *Electron microprobe analysis* (Cambridge University Press Cambridge [Eng] ; New York, 1975), ISBN 0521204666.

[70] Zeiss, *Leo Electronmikroskopie GmbH - LEO SUPRA* (10.02 instrument information booklet, 2003).

[71] A. J. Schwartz, M. Kumar, B. L. Adams, and D. P. Field, *Electron backscatter diffraction in materials science*, vol. 2 (Springer, 2009).

[72] Oxford, *Electron Backscattered Diffraction* (Oxford Instruments Analytical, 2002).

[73] J. A. Venables and C. J. Harland, The Philosophical Magazine: A Journal of Theoretical Experimental and Applied Physics **27**, 1193 (1973), URL https://doi.org/10.1080/14786437308225827.

[74] A. Winkelmann, G. Cios, T. Tokarski, G. Nolze, R. Hielscher, and T. Kozieł, Acta Materialia **188**, 376 (2020), ISSN 1359-6454, URL https://www.sciencedirect.com/science/article/pii/S1359645420300781.

[75] O. Engler and V. Randle, *Introduction to texture analysis: macrotexture, microtexture, and orientation mapping* (CRC press, 2009).

[76] B. D. Cullity, *Elements of X-ray Diffraction* (Addison-Wesley Publishing, 1956).

[77] P. Bridgman, Science **80**, 290 (1934), URL https://www.science.org/doi/abs/10.1126/science.80.2074.290.b.

[78] D. Bowen and B. Tanner, *High Resolution X-Ray Diffractometry and Topography* (CRC Press LLC, 2019), ISBN 9780367400637, URL https://books.google.it/books?id=XE1-yAEACAAJ.

[79] J. Hill and D. McMorrow, Acta Crystallographica Section A: Foundations of Crystallography **52**, 236 (1996).

[80] C. Vettier, The European Physical Journal Special Topics **208**, 3 (2012), URL https://doi.org/10.1140/epjst/e2012-01602-7.

[81] S. Grenier and Y. Joly, Journal of Physics: Conference Series **519**, 012001 (2014), URL https://dx.doi.org/10.1088/1742-6596/519/1/012001.

[82] S.-G. Sun, P. A. Christensen, and A. Wieckowski, *In-situ spectroscopic studies of adsorption at the electrode and electrocatalysis* (Elsevier, 2011).

[83] N. ASHCROFT and N. MERMIN, New York (1976).

[84] S. Hüfner and S. Hüfner, Photoelectron Spectroscopy: Principles and Applications pp. 411–500 (2003).

[85] A. Einstein, Annalen der Physik **322**, 132 (1905), URL https://onlinelibrary.wiley.com/doi/abs/10.1002/andp.19053220607.

[86] K. Wang, B. Ecker, and Y. Gao, Crystals **10** (2020), ISSN 2073-4352, URL https://www.mdpi.com/2073-4352/10/9/773.

[87] R. L. Park and M. G. Lagally, *Solid state physics: surfaces* (Academic Press, 1985).

[88] F. Reinert and S. Hüfner, New Journal of Physics **7**, 97 (2005), URL https://dx.doi.org/10.1088/1367-2630/7/1/097.

[89] K. E. Smith and S. D. Kevan, Progress in Solid State Chemistry **21**, 49 (1991), ISSN 0079-6786, URL https://www.sciencedirect.com/science/article/pii/007967869190001G.

[90] A. Damascelli, Z. Hussain, and Z.-X. Shen, Rev. Mod. Phys. **75**, 473 (2003), URL https://link.aps.org/doi/10.1103/RevModPhys.75.473.

[91] A. C. Walters, L. Alianelli, H. Wang, M. D. Watson, C. Cacho, C. Nicklin, and K. Sawhney, Journal of Physics: Conference Series **2380**, 012039 (2022), URL https://dx.doi.org/10.1088/1742-6596/2380/1/012039.

[92] K. Jenni, F. Wirth, K. Dietrich, L. Berger, Y. Sidis, S. Kunkemöller, C. P. Grams, D. I. Khomskii, J. Hemberger, and M. Braden, Phys. Rev. Mater. **4**, 085001 (2020), URL https://link.aps.org/doi/10.1103/PhysRevMaterials.4.085001.

[93] V. Granata, R. Fittipaldi, A. Guarino, A. Ubaldini, E. Carleschi, A. M. Strydom, F. Chiarella, and A. Vecchione, Journal of Alloys and Compounds **832**, 154890 (2020), ISSN 0925-8388, URL https://www.sciencedirect.com/science/article/pii/S0925838820312536.

[94] R. Fittipaldi, D. Sisti, A. Vecchione, and S. Pace, Crystal Growth & Design **7**, 2495 (2007), URL https://doi.org/10.1021/cg070180p.

[95] B. L. Treu, W. G. Fahrenholtz, and M. J. O'Keefe, Inorganic Materials **47**, 974 (2011), URL https://doi.org/10.1134/S0020168511090214.

[96] Y. Maeno, T. Ando, Y. Mori, E. Ohmichi, S. Ikeda, S. NishiZaki, and S. Nakatsuji, Phys. Rev. Lett. **81**, 3765 (1998), URL https://link.aps.org/doi/10.1103/PhysRevLett.81.3765.

[97] M. S. Anwar and J. W. A. Robinson, Coatings **11** (2021), ISSN 2079-6412, URL https://www.mdpi.com/2079-6412/11/9/1110.

[98] D. Pincini, S. Boseggia, R. Perry, M. J. Gutmann, S. Riccò, L. S. I. Veiga, C. D. Dashwood, S. P. Collins, G. Nisbet, A. Bombardi, et al., Phys. Rev. B **98**, 014429 (2018), URL https://link.aps.org/doi/10.1103/PhysRevB.98.014429.

[99] S. P. Collins, A. Bombardi, A. R. Marshall, J. H. Williams, G. Barlow, A. G. Day, M. R. Pearson, R. J. Woolliscroft, R. D. Walton, G. Beutier, et al., AIP Conference Proceedings **1234**, 303 (2010), URL https://aip.scitation.org/doi/abs/10.1063/1.3463196.

[100] K. Takenaka, N. Inoue, Y. Mizuno, Y. Okamoto, N. Katayama, Y. Sakai, T. Nishikubo, and M. Azuma, Applied Physics Letters **113**, 071902 (2018), URL https://doi.org/10.1063/1.5046463.

[101] S. Kunkemöller, E. Komleva, S. V. Streltsov, S. Hoffmann, D. I. Khomskii, P. Steffens, Y. Sidis, K. Schmalzl, and M. Braden, Phys. Rev. B **95**, 214408 (2017), URL https://link.aps.org/doi/10.1103/PhysRevB.95.214408.

[102] C. Autieri, Journal of Physics: Condensed Matter **28**, 426004 (2016), URL https://dx.doi.org/10.1088/0953-8984/28/42/426004.

[103] S. Chi, F. Ye, G. Cao, H. Cao, and J. A. Fernandez-Baca, Phys. Rev. B **102**, 014452 (2020), URL https://link.aps.org/doi/10.1103/PhysRevB.102.014452.

[104] M. Sakaki, N. Nakajima, F. Nakamura, Y. Tezuka, and T. Suzuki, Journal of the Physical Society of Japan **82**, 093707 (2013), URL https://doi.org/10.7566/JPSJ.82.093707.

[105] K. Fürsich, J. Bertinshaw, P. Butler, M. Krautloher, M. Minola, and B. Keimer, Phys. Rev. B **100**, 081101 (2019), URL https://link.aps.org/doi/10.1103/PhysRevB.100.081101.

[106] G. Mattoni, S. Yonezawa, F. Nakamura, and Y. Maeno, Phys. Rev. Mater. **4**, 114414 (2020), URL https://link.aps.org/doi/10.1103/PhysRevMaterials.4.114414.

[107] G. Chiriacò and A. J. Millis, Phys. Rev. B **102**, 085116 (2020), URL https://link.aps.org/doi/10.1103/PhysRevB.102.085116.

[108] J. Bertinshaw, N. Gurung, P. Jorba, H. Liu, M. Schmid, D. T. Mantadakis, M. Daghofer, M. Krautloher, A. Jain, G. H. Ryu, et al., Phys. Rev. Lett. **123**, 137204 (2019), URL https://link.aps.org/doi/10.1103/PhysRevLett.123.137204.

[109] H. Zhao, B. Hu, F. Ye, C. Hoffmann, I. Kimchi, and G. Cao, Phys. Rev. B **100**, 241104 (2019), URL https://link.aps.org/doi/10.1103/PhysRevB.100.241104.

[110] R. Okazaki, K. Kobayashi, R. Kumai, H. Nakao, Y. Murakami, F. Nakamura, H. Taniguchi, and I. Terasaki, Journal of the Physical Society of Japan **89**, 044710 (2020), URL https://doi.org/10.7566/JPSJ.89.044710.

[111] D. Curcio, A. J. H. Jones, R. Muzzio, K. Volckaert, D. Biswas, C. E. Sanders, P. Dudin, C. Cacho, S. Singh, K. Watanabe, et al., Phys. Rev. Lett. **125**, 236403 (2020), URL https://link.aps.org/doi/10.1103/PhysRevLett.125.236403.

[112] P. Hofmann, AVS Quantum Science **3**, 021101 (2021), URL https://doi.org/10.1116/5.0038637.

[113] J. Avila, I. Razado-Colambo, S. Lorcy, B. Lagarde, J.-L. Giorgetta, F. Polack, and M. C. Asensio, Journal of Physics: Conference Series **425**, 192023 (2013), URL https://dx.doi.org/10.1088/1742-6596/425/19/192023.

[114] F. Petocchi, V. Christiansson, and P. Werner, Phys. Rev. B **104**, 195146 (2021), URL https://link.aps.org/doi/10.1103/PhysRevB.104.195146.

[115] R. Lou, A. Fedorov, Q. Yin, A. Kuibarov, Z. Tu, C. Gong, E. F. Schwier, B. Büchner, H. Lei, and S. Borisenko, Phys. Rev. Lett. **128**, 036402 (2022), URL https://link.aps.org/doi/10.1103/PhysRevLett.128.036402.

[116] Q. Han and A. Millis, Phys. Rev. Lett. **121**, 067601 (2018), URL https://link.aps.org/doi/10.1103/PhysRevLett.121.067601.

[117] D. Cho, S. Cheon, K.-S. Kim, S.-H. Lee, Y.-H. Cho, S.-W. Cheong, and H. W. Yeom, Nature Communications **7**, 10453 (2016), URL https://doi.org/10.1038/ncomms10453.

List of Publications

[1] M. Cannavacciuolo *et al.*, "Impact of Ru excess on the structural and electronic properties of Pr doped Ca_2RuO_4 single crystals," *in preparation*, 2023.

[2] J. Neilson, V. Granata, C. A. Ofelia Durante and, G. Avallone, T. F. Bennett, F. Bobba, M. Cannavacciuolo, G. Carapella, F. Chiadini, G. De-Salvo, R. DeSalvo, R. D. Simone, C. D. Giorgio, R. Fittipaldi, V. Fiumara, B. Larsen, T. LeBohec, S. Linke, A. Micco, A. Miller, M. Mondin, B. Nayak, A. Vecchione, I. M. Pinto, and V. Pierro, "Improving the Precision of E-beam Evaporation for Nanolayered Coatings," *submitted to Applied Sciences*, 2023.

[3] D. Curcio, C. E. Sanders, A. Chikina, H. E. Lund, M. Bianchi, V. Granata, M. Cannavacciuolo, G. Cuono, C. Autieri, F. Forte, A. Romano, M. Cuoco, P. Dudin, J. Avila, C. Polley, T. Balasubramanian, R. Fittipaldi, A. Vecchione, and P. Hofmann, "Current driven insulator-to-metal transition without Mott breakdown in Ca_2RuO_4," *submitted to Physical Review Letter*, 2023.

[4] R. Abbott, ... and M. Cannavacciuolo, *et al.* (LVK Collaboration), "Population of Merging Compact Binaries Inferred Using Gravitational Waves through GWTC-3," *Physical Review X*, vol. 13, no. 1, 2023.

[5] R. Abbott, ... and M. Cannavacciuolo, *et al.* (LVK Collaboration), "The Advanced Virgo+ status," *Journal of Physics: Conference Series*, vol. 2429, no. 1, 2023.

[6] R. Abbott, ... and M. Cannavacciuolo, *et al.* (LVK Collaboration), "Advanced Virgo Plus: Future Perspectives," *Journal of Physics: Conference Series*, vol. 2429, no. 1, 2023.

[7] R. Abbott, ... and M. Cannavacciuolo, *et al.* (LVK Collaboration), "Model-based Cross-correlation Search for Gravitational Waves from the Low-mass X-Ray Binary Scorpius X-1 in LIGO O3 Data," *Astrophysical Journal Letters*, vol. 941, no. 2, 2022.

[8] R. Abbott, ... and M. Cannavacciuolo, *et al.* (LVK Collaboration), "The Virgo O3 run and the impact of the environment," *Classical and Quantum Gravity*, vol. 39, no. 23, 2022.

[9] D. Porter, F. Forte, V. Granata, M. Cannavacciuolo, R. Fittipaldi, M. Cuoco, A. Bombardi, and A. Vecchione, "Guiding antiferromagnetic transitions in Ca_2RuO_4," *Scientific Reports*, vol. 12, no. 1, 2022.

[10] R. Abbott, ... and M. Cannavacciuolo, *et al.* (LVK Collaboration), "All-sky search for continuous gravitational waves from isolated neutron stars using Advanced LIGO and Advanced Virgo O3 data," *Physical Review D*, vol. 106, no. 10, 2022.

[11] R. Abbott, ... and M. Cannavacciuolo, *et al.* (LVK Collaboration), "Search for gravitational waves from Scorpius X-1 with a hidden Markov model in O3 LIGO data," *Physical Review D*, vol. 106, no. 6, 2022.

[12] R. Abbott, ... and M. Cannavacciuolo, *et al.* (LVK Collaboration), "Search for continuous gravitational wave emission from the Milky Way center in O3 LIGO-Virgo data," *Physical Review D*, vol. 106, no. 4, 2022.

[13] R. Abbott, ... and M. Cannavacciuolo, *et al.* (LVK Collaboration), "Search for Subsolar-Mass Binaries in the First Half of Advanced LIGO's and Advanced Virgo's Third Observing Run," *Physical Review Letters*, vol. 129, no. 6, 2022.

[14] R. Abbott, ... and M. Cannavacciuolo, *et al.* (LVK Collaboration), "Searches for Gravitational Waves from Known Pulsars at Two Harmonics in the Second and Third LIGO-Virgo Observing Runs," *Astrophysical Journal*, vol. 935, no. 1, 2022.

[15] R. Abbott, ... and M. Cannavacciuolo, *et al.* (LVK Collaboration), "All-sky, all-frequency directional search for persistent gravitational waves from Advanced LIGO's and Advanced Virgo's first three observing runs," *Physical Review D*, vol. 105, no. 12, 2022.

[16] R. Abbott, ... and M. Cannavacciuolo, *et al.* (LVK Collaboration), "Narrowband Searches for Continuous and Long-duration Transient Gravitational Waves from Known Pulsars in the LIGO-Virgo Third Observing Run," *Astrophysical Journal*, vol. 932, no. 2, 2022.

[17] R. Abbott, ... and M. Cannavacciuolo, *et al.* (LVK Collaboration), "First joint observation by the underground gravitational-wave detector KAGRA with GEO 600," *Progress of Theoretical and Experimental Physics*, vol. 2022, no. 6, 2022.

[18] R. Abbott, ... and M. Cannavacciuolo, *et al.* (LVK Collaboration), "All-sky search for gravitational wave emission from scalar boson clouds around spinning black holes in LIGO O3 data," *Physical Review D*, vol. 105, no. 10, 2022.

[19] R. Abbott, ... and M. Cannavacciuolo, *et al.* (LVK Collaboration), "Search of the early O3 LIGO data for continuous gravitational waves from the Cassiopeia A and Vela Jr. supernova remnants," *Physical Review D*, vol. 105, no. 8, 2022.

[20] R. Abbott, ... and M. Cannavacciuolo, *et al.* (LVK Collaboration), "Search for Gravitational Waves Associated with Gamma-Ray Bursts Detected by Fermi and Swift during the LIGO-Virgo Run O3b," *Astrophysical Journal*, vol. 928, no. 2, 2022.

[21] R. Abbott, ... and M. Cannavacciuolo, *et al.* (LVK Collaboration), "Constraints on dark photon dark matter using data from LIGO's and Virgo's third observing run," *Physical Review D*, vol. 105, no. 6, 2022.

[22] R. Abbott, ... and M. Cannavacciuolo, *et al.* (LVK Collaboration), "Search for intermediate-mass black hole binaries in the third observing run of Advanced LIGO and Advanced Virgo," *Astronomy and Astrophysics*, vol. 659, 2022.

[23] R. Abbott, ... and M. Cannavacciuolo, *et al.* (LVK Collaboration), "Calibration of advanced Virgo and reconstruction of the detector strain h(t) during the observing run O3," *Classical and Quantum Gravity*, vol. 39, no. 4, 2022.

[24] R. Abbott, ... and M. Cannavacciuolo, *et al.* (LVK Collaboration), "Search for continuous gravitational waves from 20 accreting millisecond x-ray pulsars in O3 LIGO data," *Physical Review D*, vol. 105, no. 2, 2022.

[25] R. Abbott, ... and M. Cannavacciuolo, *et al.* (LVK Collaboration), "All-sky search for short gravitational-wave bursts in the third Advanced LIGO and Advanced Virgo run," *Physical Review D*, vol. 104, no. 12, 2021.

[26] R. Abbott, ... and M. Cannavacciuolo, *et al.* (LVK Collaboration), "Search for Lensing Signatures in the Gravitational-Wave Observations from the First Half of LIGO-Virgo's Third Observing Run," *Astrophysical Journal*, vol. 923, no. 1, 2021.

[27] R. Abbott, ... and M. Cannavacciuolo, *et al.* (LVK Collaboration), "Constraints from LIGO O3 Data on Gravitational-wave Emission Due to R-modes in the Glitching Pulsar PSR J0537-6910," *Astrophysical Journal*, vol. 922, no. 1, 2021.

[28] R. Abbott, ... and M. Cannavacciuolo, *et al.* (LVK Collaboration), "All-sky search for long-duration gravitational-wave bursts in the third Advanced LIGO and Advanced Virgo run," *Physical Review D*, vol. 104, no. 10, 2021.

[29] R. Abbott, ... and M. Cannavacciuolo, *et al.* (LVK Collaboration), "Searches for continuous gravitational waves from young supernova remnants in the early third observing run of advanced LIGO and Virgo," *Astrophysical Journal*, vol. 921, no. 1, 2021.

[30] R. Abbott, ... and M. Cannavacciuolo, *et al.* (LVK Collaboration), "All-sky search for continuous gravitational waves from isolated neutron stars in the early O3 LIGO data," *Physical Review D*, vol. 104, no. 8, 2021.

[31] R. Abbott, ... and M. Cannavacciuolo, *et al.* (LVK Collaboration), "Search for anisotropic gravitational-wave backgrounds using data from Advanced LIGO and Advanced Virgo's first three observing runs," *Physical Review D*, vol. 104, no. 2, 2021.

[32] R. Abbott, ... and M. Cannavacciuolo, *et al.* (LVK Collaboration), "Upper limits on the isotropic gravitational-wave background from Advanced LIGO and Advanced Virgo's third observing run," *Physical Review D*, vol. 104, no. 2, 2021.

[33] R. Abbott, ... and M. Cannavacciuolo, *et al.* (LVK Collaboration), "Observation of Gravitational Waves from Two Neutron Star-Black Hole Coalescences," *Astrophysical Journal Letters*, vol. 915, no. 1, 2021.

[34] R. Abbott, ... and M. Cannavacciuolo, *et al.* (LVK Collaboration), "Constraints on Cosmic Strings Using Data from the Third Advanced LIGO-Virgo Observing Run," *Physical Review Letters*, vol. 126, no. 24, 2021.

[35] R. Abbott, ... and M. Cannavacciuolo, *et al.* (LVK Collaboration), "Diving below the Spin-down Limit: Constraints on Gravitational Waves from the Energetic Young Pulsar PSR J0537-6910," *Astrophysical Journal Letters*, vol. 913, no. 2, 2021.

[36] R. Abbott, ... and M. Cannavacciuolo, *et al.* (LVK Collaboration), "All-sky search in early O3 LIGO data for continuous gravitational-wave signals from unknown neutron stars in binary systems," *Physical Review D*, vol. 103, no. 6, 2021.

[37] R. Abbott, ... and M. Cannavacciuolo, *et al.* (LVK Collaboration), "High-bandwidth beam balance for vacuum-weight experiment and Newtonian noise subtraction," *European Physical Journal Plus*, vol. 136, no. 3, 2021.

[38] G. Balestrino, M. Cannavacciuolo, R. Di Leo, L. Maritato, A. Nigro, P. Romano, R. Vaglio, and P. Paroli, "Transport properties of textured $Bi_2Sr_2CaCu_2O_{8+y}$, thin films," *Journal of Superconductivity*, vol. 3, no. 2, pp. 215–220, 1990.

[39] M. Cannavacciuolo, R. Di Leo, L. Maritato, A. Nigro, P. Romano, and R. Vaglio, "Fabrication and properties of thin films of the $YBa_2Cu_3O_7$ compound," *Physica C: Superconductivity and its Applications*, vol. 162-164, no. PART 2, pp. 1063–1064, 1989.